Absolute Trends and Accurate and Precise Gas-Phase Binding Energies of 1-Alkyl-3-Methylimidazolium Tetrafluoroborate Ionic Liquid Clusters from Combined Independent and Competitive TCID Measurements

H. A. Roy and M. T. Rodgers*

Department of Chemistry, Wayne State University, Detroit, MI, 48202, USA

Abstract

Ionic liquid (IL) development efforts have focused on achieving desired properties via tuning of the IL through variation of the cations and anions. However, works geared toward a microscopic understanding of the nature and strength of the intrinsic cation-anion interactions of ILs have been rather limited such that the intrinsic strength of the cation-anion interactions in ILs is largely unknown. In previous work, we employed threshold collision-induced dissociation (TCID) approaches supported and enhanced by electronic structure calculations to characterize the nature of the cation-anion interactions in and determine the bond dissociation energies (BDEs) of a series of four 2:1 clusters of 1-alkyl-3-methylimidazolium cations and tetrafluoroborate anions, $[2C_nmim{:}BF_4]^+$. The cation was varied over the series: 1-ethyl-3-methylimidazolium, $[C_2mim]^+$, 1-butyl-3-methylimidazolium, $[C_4mim]^+$, 1-hexyl-3-methylimidazolium, $[C_6mim]^+$, and 1-octyl-3-methylimidazolium, $[C_8mim]^+$, to determine the structural and energetic effects of the size of the 1-alkyl substituent on the binding. The variation in the strength of binding determined for these $[2C_nmim{:}BF_4]^+$ clusters was found to be similar in magnitude to the average experimental uncertainty in these determinations. To definitively establish an absolute order of binding among these $[2C_nmim{:}BF_4]^+$ clusters we extend this work here to include competitive binding studies of three mixed 2:1 clusters of 1-alkyl-3-methylimidazolium cations and tetrafluoroborate anions, $[C_{n-2}mim{:}BF_4{:}C_nmim]^+$ for n = 4, 6, and 8. Importantly, the results of the present work simultaneously provide the absolute BDEs of these mixed $[C_{n-2}mim{:}BF_4{:}C_nmim]^+$ clusters and the absolute relative order of the intrinsic binding interactions as a function of the cation with significantly improved precision. Further, by combining the thermochemical results of the previous and present studies, the BDEs of the $[2C_nmim{:}BF_4]^+$ clusters are more accurately and precisely determined.

Corresponding author: M. T. Rodgers, mrodgers@chem.wayne.edu, Tel. (313) 577-2431

Introduction

Ionic liquids (ILs) are molten salts that have melting points that are much lower than those of traditional salts, and typically below ~ 100° C. The cations and anions that may comprise an IL are extraordinarily diverse,[1] and as such enable tunability of its' properties for a wide variety of applications spanning electrochemistry,[2,3] energy storage,[4-6] organic and inorganic synthesis,[7-9] gas and liquid chromatographic separations,[10-13] and space propulsion.[14-16] Common IL cations include: ammonium, imidazolium, phosphonium, pyridinium, and sulfonium ions and their alkylated derivatives. Common IL anions are generally weakly coordinating organic and inorganic anions such as acetates, borates, imides, phosphates, sulfates, and sulfonates and their halogenated derivatives. A thorough understanding of how the specific cations and anions affect the properties of an IL is essential to the intelligent development of ILs for targeted applications.

Understanding the intrinsic interactions, reactivity, and clustering of ILs for their use as fuels in electrospray propulsion provides the motivation for this work. Specifically, we are interested in determining the impact that the cations and anions of an IL have on thrust and efficiency for electrospray propulsion. Knowledge of the gas-phase reaction dynamics and intrinsic binding interactions of ILs can aid in the elucidation of that knowledge and help lead the development of task-specific ILs. Electrospray propulsion has the benefits of easy miniaturization and low complexity making this propulsion technique amenable to nanosatellite propulsion.[17] The propulsion mechanism associated with electrospray thrusters parallels that of electrospray ionization (ESI),[18] presently one of the most commonly employed ionization techniques for mass spectrometry. In electrospray thrusters, an alternating high voltage is applied to an electrospray emitter facilitating the formation of ions. The ions are accelerated in the electric field, generating thrust as the ions are emitted from the spacecraft. The thrust generated is generally very small, therefore an array of emitters are needed to generate the required thrust of a small nanosatellite.[17]

A variety of ILs are being investigated as potential fuels for space propulsion using electrospray thrusters including 1-alkyl-3-methylimidazolium tetrafluoroborate ILs, $C_n$mim-BF_4,

where n describes the number of carbon atoms in the 1-alkyl chain.[19,20] The $C_n$mim-BF_4 ILs with ethyl, butyl, hexyl, and octyl 1-alkyl substituents have been studied in greatest detail as their properties are best matched to space propulsion needs. In previous work, we employed threshold collision-induced dissociation (TCID) approaches combined with electronic structure calculations to characterize the nature of the cation-anion interactions and determined the bond dissociation energies (BDEs) of a series of four 2:1 clusters of 1-alkyl-3-methylimidazolium cations and tetrafluoroborate anions, $[2C_n\text{mim:}BF_4]^+$ for n = 2, 4, 6, and 8.[21] The structures of the cations: 1-ethyl-3-methylimidazolium, $[C_2\text{mim}]^+$, 1-butyl-3-methylimidazolium, $[C_4\text{mim}]^+$, 1-hexyl-3-methylimidazolium, $[C_6\text{mim}]^+$, and 1-octyl-3-methylimidazolium, $[C_8\text{mim}]^+$, (including atom numbering) and the $[BF_4]^-$ anion are shown in **Figure 1**. The primary dissociation pathway observed for all four clusters involves loss of a neutral ($C_n$mim:BF_4) ion pair, as described by **reaction 1**.

$$[2C_n\text{mim:}BF_4]^+ + Xe \rightarrow [C_n\text{mim}]^+ + (C_n\text{mim:}BF_4) \quad (1)$$

The BDEs of the $[2C_n\text{mim:}BF_4]^+$clusters were determined from thermochemical analyses of the $[C_n\text{mim}]^+$ product cross sections. The differences in the BDEs measured for these clusters are rather small and of similar magnitude to the uncertainties in the measurements. Thus, the trend in the BDEs as a function of the $[C_n\text{mim}]^+$ cation are indiscernible based only on these measurements. Further, although theory is often able to predict relative trends with high fidelity, inconsistencies in the computed trends are also found among the B3LYP, B3LYP-GD3BJ and M06-2X levels of theory investigated. Similar to the measured BDEs, the accuracy of the theoretically predicted values is also similar or slightly larger than the differences in the strength of binding. Competitive measurements are thus needed to establish a definitive order of binding.

The importance of elucidating absolute and relative trends in the structure, energetics, and reactivity of chemical systems has long been appreciated and has led to the development of absolute and relative cation and anion affinity scales for a wide variety of neutral and ionic systems.[22-24] In particular, electrospray ionization tandem mass spectrometry (ESI-MS/MS) approaches typically using collisional activation have been employed to examine the dissociation

of IL clusters to establish cation-anion interaction scales for ILs.[25,26-32] Several studies have examined the variable-energy CID behavior of cationic and anionic clusters of various ILs as a function of collision energy. In contrast to the threshold CID approach employed in our work, where energetic information is extracted at the onset of dissociation, these studies were based on comparisons at 50% dissociation. Bini et al. used the variable-energy CID approach to examine the competitive dissociation of $[C_2mim:Br:C_nmim]^+$ clusters for n = 4, 6, and 8. Based on the measured intensities, the relative order of binding was found to be $[C_nmim]^+ < [C_2mim]^+$ for all three clusters. Although no other mixed clusters were examined, the relative intensities of the $[C_nmim]^+$ vs. $[C_2mim]^+$ cations across these experiments suggest that the relative intrinsic binding for the imidazolium cations to the $[Br]^-$ anion follows the order: $[C_8mim]^+ < [C_6mim]^+ < [C_4mim]^+ < [C_2mim]^+$.[26] Fernandes et al.[25,29] also used the variable-energy CID behavior approach to examine the intrinsic binding of the $[C_nmim]^+$ cations in $[2C_nmim:X]^+$ clusters where $[X]^- = [Cl]^-$, $[BF_4]^-$ and bis(trifluoromethyl)sulfonylimide, $[Tf_2N]^-$. Based on the relative center-of-mass collision energies at 50% dissociation, the relative order of binding follows the order: $[C_8mim]^+ < [C_6mim]^+ < [C_4mim]^+ < [C_2mim]^+$ for both $[Cl]^-$ and $[Tf_2N]^-$; the same order excluding the $[C_6mim]^+$ cation, which was not included in that work, was also found for $[BF_4]^-$. Using Cooks' kinetic method, Vitorino et al. [28] also confirmed the relative order of binding of the $[C_nmim]^+$ cations to $[Tf_2N]^-$ as $[C_6mim]^+ < [C_4mim]^+ < [C_2mim]^+$ consistent with that observed by Bini et al. These works suggest that the overall relative order of binding of the $[C_nmim]^+$ cations to $[BF_4]^-$ follows the order: $[C_8mim]^+ < [C_6mim]^+ < [C_4mim]^+ < [C_2mim]^+$. However, because the competitive experiments did not comprehensively examine other mixed clusters, and the energy-resolved experiments did not incorporate internal energy and unimolecular dissociation rates into the comparisons of the experimental data, there is still some uncertainty in this conclusion. Further, none of these other works have provided absolute binding affinities or BDEs of the IL clusters under investigation.

In the present work, a combination of theory and experiment are utilized to determine the impact of cation variation on the structure and energetics of mixed IL clusters. Threshold

collision-induced dissociation (TCID) of three $[C_{n-2}mim:BF_4:C_nmim]^+$ clusters, n = 4, 6, and 8, is performed with Xe. Absolute BDEs of these clusters are reported, both for the binding of the $[C_nmim]^+$ cation to the ($C_{n-2}mim:BF_4$) ion pair as well as the binding of the $[C_{n-2}mim]^+$ cation to the ($C_nmim:BF_4$) ion pair. Relative ion pairing energies (ΔIPEs) of the ($C_nmim:BF_4$) and ($C_{n-2}mim:BF_4$) ion pairs are also estimated from the differences in the BDEs measured for the $[C_{n-2}mim:BF_4:C_nmim]^+$ clusters. Comparisons are made between the experimentally determined values and the ΔBDEs and ΔIPEs determined from electronic structure calculations. Further, the absolute BDEs previously reported for the $[2C_nmim:BF_4]^+$ clusters are combined with the ΔIPEs of the ($C_nmim:BF_4$) ion pairs determined here and subjected to a maximal likelihood analysis to improve the accuracy and precision in the BDEs determined.

Experimental and Computational Methods

Sample Preparation. The ILs and electrospray solvents were purchased from commercial vendors and used as received. HPLC grade solvents were used. Methanol was purchased from Fischer Scientific (Waltham, MA, USA). Water, 1-ethyl-3-methylimidazolium tetrafluoroborate, C_2mim-BF_4, and 1-hexyl-3-methylimidazolium bis(trifluoromethylsulfonyl)-imide, C_6mim-Tf_2N, were purchased from Sigma Aldrich (St. Louis, MO, USA). 1-Butyl-3-methylimidazolium tetrafluoroborate, C_4mim-BF_4, and 1-octyl-3-methyl-imidazolium bis(trifluoromethylsulfonyl)imide, C_8mim-Tf_2N, were purchased from Alfa Aesar (Haverhill, MA, USA). Working solutions with ~0.5 mM of each constituent in 50:50 methanol:water (v:v) were prepared by diluting mixtures of the relevant two (or three) ILs, and relying on ion exchange in solution to enable generation of the desired $[C_{n-2}mim:BF_4:C_nmim]^+$ cluster via electrospray ionization.

Experimental Procedures. TCID experiments were performed for three $[C_{n-2}mim:BF_4:C_nmim]^+$ clusters using a custom-built guided ion beam tandem mass spectrometer (GIBMS)[33] coupled to a custom-built electrospray ionization (ESI) source.[34,35] Sample solutions were infused using a syringe pump through a 35 gauge stainless steel ESI emitter at a flow rate

of ~ 1.2 μL/min. Stable Taylor cone formation and ion generation were observed at ~ +2 kV. The ESI plume was sampled through a 0.012" diameter limiting orifice and ions were transferred to the first stage of the mass spectrometer via a heated capillary inlet held at ~100°C. An rf ion funnel (IF) traps ions exiting the capillary in the radial direction and focuses and injects the ions into an rf hexapole ion guide (6P). The IF was operated at 530 kHz and 25 V_{pp}; the rf is applied 180° out of phase to alternate adjacent ring electrodes. A 25 V_{dc} gradient was applied across the IF to draw the ions into the mass spectrometer. The last two plates of the IF serve as a limiting orifice to throttle the gas load and as an injection lens to focus and inject the ions into the 6P. The 6P spans a differentially pumped chamber at sufficiently high pressure that the ions undergo > 10^4 thermalizing collisions, resulting in a room temperature distribution. The ion beam is converted from a cylindrical to a ribbon-shaped geometry to facilitate the first stage of mass selection in the magnetic sector momentum analyzer. After mass selection, the precursor ion beam was reconverted from ribbon to cylindrical geometry, and the precursor ions were slowed to a nominal kinetic energy using an exponential retarder. The precursor ions were then focused into an rf octopole ion guide (8P) spanning a collision cell. A dc offset was applied in the 8P that determines the collision energy of the precursor $[C_{n-2}mim:BF_4:C_nmim]^+$ cluster with the collision gas, Xe. Xenon is chosen as the collision gas for its large size and polarizability, resulting in larger measured cross sections.[36-38] Remaining precursor ions and fragment ions traverse the 8P and are focused into a quadrupole mass filter for the second stage of mass analysis. Ions are detected using a Daly detector[39] and standard pulse-counting electronics.

Theoretical Calculations. In previous work, theoretical calculations were performed to characterize the structures and stabilities of the $[C_nmim]^+$ and $[BF_4]^-$ ions and their modes of binding in the $(C_nmim:BF_4)$ ion pairs and $[2C_nmim:BF_4]^+$ clusters.[21] Parallel theoretical procedures were pursued here to extend these calculations to include characterization of the structures and stabilities of the mixed $[C_{n-2}mim:BF_4:C_nmim]^+$ clusters. Briefly, molecular mechanics conformational searching was used to generate preliminary structures, which were then subjected to density functional theory calculations. A molecular mechanics simulated

annealing procedure[40] was performed in HyperChem[41] using the Amber 3 force field. To prevent dissociation from occurring during the simulated annealing procedure, the cation(s) and anion of the $[C_{n-2}mim:BF_4:C_nmim]^+$ cluster were constrained to the coordinate origin. The restraining force constant was empirically chosen and set to 0.01 kcal $mol^{-1}Å^{-2}$ to provide reasonable sampling of conformational space. In each cycle of simulated annealing, the internal energy of the system was first increased by linearly ramping the temperature from 0 to 1000 K over a period of 0.3 ps. The simulation temperature, 1000 K, was then maintained for 0.2 ps to allow the system to sample conformational space. The internal energy of the system was then returned to 0 K by linearly decreasing the temperature from 1000 to 0 K over a period of 0.3 ps. At the end of each simulated annealing cycle, a snapshot of the system was saved and used to initiate the next cycle. Typically, 300 cycles of heating, conformational sampling, and cooling were performed. The resulting snapshot structures were sorted by energy, and ~20–40 structures were sampled for follow-up density functional theory calculations. In addition, 20 of the lowest-energy structures previously found for the $[2C_nmim:BF_4]^+$ clusters[21] for n = 4, 6, and 8 were selected and used to generate additional candidate structures for the $[C_{n-2}mim:BF_4:C_nmim]^+$ clusters by shortening the 1-alkyl chain of one of the cations by an ethyl moiety. This procedure generated two new candidate structures for the mixed IL cluster from each $[2C_nmim:BF_4]^+$ structure, thereby providing ~ 40 additional unique structures that were subjected to density functional theory calculations. This latter procedure was often effective at facilitating more rapid geometry optimization and producing stable conformers that were generally among the most stable conformers found.

Electronic structure calculations were performed using Gaussian 09.[42] Geometry optimizations and frequency analyses were performed using three density function theory methods: B3LYP,[43-46] B3LYP-GD3BJ,[47] and M06-2X[48] each with the 6-311+G(d,p) basis set. To improve accuracy of the energetic predictions, single point energies were calculated using the same theoretical approach, but with an extended basis set that includes additional diffuse and polarization functions, the 6-311+G(2d,2p) basis set. Basis set superposition error (BSSE)[49,50]

and zero-point energy (ZPE) corrections were included for all three levels of theory. The M06-2X calculations were sometimes plagued by convergence issues during geometry optimization and frequency analysis, which necessitated the use of an ultrafine integration grid for these conformers. The stabilities of structures that required the use of an ultrafine integration grid for convergence are indicated with an asterisk.

Electrostatic potential (ESP) maps were also computed for the B3LYP and M06-2X optimized geometries of the ground conformers of the $[C_{n-2}mim:BF_4:C_nmim]^+$ clusters. These ESP maps along with those of the $[C_nmim]^+$ cations, $[BF_4]^-$ anion, ($C_nmim:BF_4$) ion pairs, and $[2C_nmim:BF_4]^+$ clusters[21] are used to visualize the favorable interaction sites of the $[C_nmim]^+$ cations and $[BF_4]^-$ anion, and how they are influenced by the intrinsic binding interactions in the 1:1 neutral ion pairs and 2:1 cationic clusters. All ESP maps were generated using the B3LYP or M06-2X functional with a 6-311+G(2d,2p) basis set and displayed at an isosurface of 0.01 a.u. of the total SCF electron density. The Mülliken charges on the hydrogen atoms of the $[C_nmim]^+$ cations and the fluorine atoms of the $[BF_4]^-$ anion are labeled. The most electronegative regions are color-coded in red, whereas the most electropositive regions are color-coded in blue (see the colorbar of the figure in which the ESP maps are shown.

As for the $[C_nmim]^+$ cations, $[BF_4]^-$ anion, ($C_nmim:BF_4$) ion pairs and $[2Cnmim:BF4]^+$ clusters,[21] noncovalent interactions within the B3LYP/6-311+G(d,p) and M06-2X/6-311+G(d,p) ground conformers of the $[C_{n-2}mim:BF_4:C_nmim]^+$ clusters were also calculated using the NCIPLOT method previously described by Yang and coworkers.[51,52] The input needed for the NCIPLOT method can be extracted directly from the Gaussian output files. the NCIPLOT procedure looks for peaks in the reduced electron density gradient that occur at low densities. The sign of the second density Hessian eigenvalue times the density distinguishes between attractive and repulsive interactions, whereas its magnitude describes the strength of interaction. Visual Molecular Dynamics (VMD) software[53] was used to render and visualize the NCI maps, which are shown at an isosurface of 0.20 a.u. of the reduced electron density gradient isosurfaces determined using the same density functional but with the 6-311+G(2d,2p) basis set employed

for energetics in this work. Strong attractive interactions, e.g., hydrogen-bonding interactions, appear blue; weak attractive interactions, e.g., London dispersion interactions, appear green; strong repulsive forces such as steric interactions appear in red.

Thermochemical Analysis. The intensities of the precursor $[C_{n-2}mim:BF_4:C_nmim]^+$ cluster and CID fragment ions were measured as a function of collision energy and pressure of the neutral collision gas, Xe. The Beer's law relationship of **eq 2** was used to convert the measured ion intensities to energy-dependent CID cross sections.

$$I = I_0 \, exp(-\sigma_{tot} n l) \qquad (2)$$

Here I is the measured intensity of the precursor ion, I_0 is the total ion intensity (i.e., the sum of the precursor and CID product ion intensities), σ_{tot} is the total CID cross section, n is the Xe collision gas density, and l the effective interaction path length. The dc offset applied to the 8P is scanned to vary the collision energy, and to determine the zero and width of the ion kinetic energy distribution.[54] The ion kinetic energy distributions of the $[C_{n-2}mim:BF_4:C_nmim]^+$ clusters measured here are well described by Gaussian distributions with full-width at half-maximum (fwhm) of ~ 0.3–0.4 eV in the laboratory frame. Energies in the laboratory frame are converted to energies in the center-of-mass frame using the relationship described by **eq 3**.

$$E_{cm} = E_{Lab} \, m/(m + M) \qquad (3)$$

where m is the mass of the neutral collision gas Xe and M is the mass of the precursor $[C_{n-2}mim:BF_4:C_nmim]^+$ cluster ion. Pressure dependent studies are performed because multiple collisions can impact the shape of CID cross sections, particularly in the threshold region, and shift the apparent threshold to lower collision energies.[36] The CID cross sections were measured at nominal Xe pressures of 0.20, 0.10, and 0.05 mTorr and pressure extrapolated to zero pressure to analytically remove the effects of secondary collisions.

The fitting procedures employed for the thermochemical analysis of CID cross sections have evolved over the years as new insight into energy transfer and dynamics of CID processes as well as modeling of the rates of unimolecular decomposition have been gained, and have been

discussed in detail previously.[33,55,56] Briefly, thresholds are determined through a fitting procedure with an empirical threshold law of the form,

$$\sigma(E) = \sigma_0 \sum g_i (E + E_i - E_0)^n / E \quad (4)$$

where σ_0 is an energy-independent scaling factor, E is the relative translational energy of the $[C_{n-2}mim:BF_4:C_nmim]^+$ IL cluster and Xe reactants, E_0 is the threshold for reaction of the ground electronic and ro-vibrational state, and n is an adjustable parameter that describes the efficiency of kinetic to internal energy transfer.[33,55,56] The summation is over the ro-vibrational states of the reactants i, where E_i is the excitation energy of each state and g_i is the population of that state, ($\Sigma g_i = 1$). The density of ro-vibrational states is determined using the Beyer-Swinehart algorithm.[57] The relative populations g_i are calculated assuming a Maxwell-Boltzmann distribution of the precursor $[C_{n-2}mim:BF_4:C_nmim]^+$ cluster at 298 K. The B3LYP/6-311+G(d,p) frequencies were scaled by the recommended factor of 0.9887[58] to correct for anharmonicity effects not accounted for in the frequency analyses, which are based on the harmonic oscillator approximation. The B3LYP-GD3BJ and M06-2X computed frequencies were used without scaling as excellent correlation with the scaled B3LYP frequencies was found.[21]

Equation 4 provides robust modeling of CID cross sections only in cases where the rate of dissociation is very rapid such that the activated $[C_{n-2}mim:BF_4:C_nmim]^+$ precursor ions dissociate before they reach the end of the 8P. However, this is typically the case only for very small or very weakly-bound systems. To properly account for dissociation not occurring on the timescale of the experiments (~ 100 μs), the empirical threshold law of **eq 4** is modified to incorporate lifetime effects using Rice-Ramsperger-Kassel-Marcus (RRKM) theory as described by **eq 5**, and discussed in depth previously.[55,59]

$$\sigma(E) = \left(\frac{n\sigma_0}{E}\right) \sum g_i \int_0^{E+E_i-E_0} [1 - e^{-k(E^*)\tau}](\Delta E)^{n-1} d(\Delta E) \quad (5)$$

The integration is over the dissociation probability, $k(E^*)$ is the unimolecular dissociation rate constant, and $E^* = E + E_i + \Delta E$, is the internal energy of the energized $[C_{n-2}mim:BF_4:C_nmim]^+$ cluster after the collision.

Equation 5 provides robust modeling of CID cross sections that exhibit a single primary dissociation pathway. However, if dissociation occurs via two or more competing pathways of similar energy, then the apparent threshold for the less favorable pathway is shifted to higher energy, a "competitive shift". To properly account for such competitive dissociation and enable extraction of accurate energetics, the empirical threshold law is modified to enable simultaneous analysis of competitive dissociation pathways as described previously, **eq 6**.[55,56]

$$\sigma(E) = \left(\frac{n\sigma_{0,j}}{E}\right) \sum g_i \int_0^{E+E_i-E_{0,j}} \frac{k_j(E^*)}{k_{tot}(E^*)} [1 - e^{-k_{tot}(E^*)\tau}](\Delta E)^{n-1} d(\Delta E) \qquad (6)$$

This modified form of the empirical threshold law incorporates competition between CID pathways, the subscript j designating the two CID pathways. Competition is described by the ratio of the unimolecular dissociation rate constant for a given CID pathway, $k_j(E^*)$, vs. the total unimolecular dissociation rate constant, $k_{tot}(E^*)$. Based on this model, the $\sigma_{0,j}$ values that describe the competitive dissociation behavior should in principle be the same for both dissociation pathways. However, we have previously found that CID cross sections cannot always be accurately reproduced unless the $\sigma_{0,j}$ values are not constrained to be equal to one another.[56,60-65] Thus, data was first analyzed using a single σ_0 value for both dissociation channels. In cases where the data could not be accurately reproduced in this fashion, the $\sigma_{0,j}$ values were allowed to vary to enable reproduction of the experimental cross sections with high fidelity.

The zero-pressure-extrapolated CID cross sections are modeled using **eq 4**, **eq 5**, and **eq 6**. Threshold energies extracted using **eq 6** provide the most accurate energetics for these systems, whereas values extracted from analyses using **eq 5** do not correct for competitive effects and those using **eq 4** do not correct for lifetime or competitive effects. Comparisons of values extracted from these analyses enable the lifetime and competitive effects to be assessed, and kinetic and competitive shifts in the CID cross sections to be quantitatively determined.

The errors in the threshold energies determined include variances from analyses of multiple datasets (typically the largest source of error), uncertainties in the vibrational frequencies predicted by theory and the resultant frequency effects on the estimation of internal

energy and RRKM lifetimes for dissociation, and the error in the absolute energy scale. Uncertainties introduced in the threshold determinations as a result of errors in the vibrational frequencies were estimated by scaling the predicted values up and down by 10%, and by increasing and decreasing the time assumed available for dissociation by a factor of two. The absolute energy scale has an uncertainty of ±0.05 eV in the laboratory frame (limited by the voltage output of the 8P dc power supply). This translates to an uncertainty of ~ ±0.02 eV (cm) for the $[C_{n-2}mim:BF_4:C_nmim]^+$ clusters examined here.[54] Uncertainties in the absolute cross section have been previously estimated to be ~ ±20%; uncertainties in the relative cross sections are smaller due to cancellation of errors and have been estimated to be ~ ±5%.[54]

RESULTS

Cross Sections for Collision-Induced Dissociation. Energy-dependent CID cross sections were measured for the interaction of three $[C_{n-2}mim:BF_4:C_nmim]^+$ clusters with Xe, where n = 4, 6 and 8; representative data for all three clusters are shown in **Figure 2**. The dominant fragmentation pathways observed for all three clusters involve competitive loss of a neutral ion pair and detection of the complementary cation as described by **reactions 7** and **8**.

$$[C_{n-2}mim:BF_4:C_nmim]^+ + Xe \rightarrow [C_nmim]^+ + (C_{n-2}mim:BF_4) + Xe \quad (7)$$

$$\rightarrow [C_{n-2}mim]^+ + (C_nmim:BF_4) + Xe \quad (8)$$

For all three clusters, the $[C_nmim]^+$ product cross section (**reaction 7**) exhibits a slightly lower apparent threshold than the $[C_{n-2}mim]^+$ product cross section (**reaction 8**). The competitive CID data for each of the three clusters immediately establish the relative order of intrinsic binding of the $[C_nmim]^+$ cations to $[BF_4]^-$ as internal energy and lifetime effects have an equivalent impact on both reaction channels: $[C_nmim]^+ < [C_{n-2}mim]^+$. Combined these data indicate a relative order of binding of: $[C_8mim]^+ < [C_6mim]^+ < [C_4mim]^+ < [C_2mim]^+$. However, to quantitatively determine the relative binding affinities of these $[C_nmim]^+$ cations for $[BF_4]^-$, thermochemical analyses that include the effects of the kinetic and internal energy distributions of the $[C_{n-2}mim:BF_4:C_nmim]^+$ and Xe reactants and the lifetime for dissociation including the effects of

competition are necessary as described in the **Thermochemical Analysis** section. Sequential dissociation of the $[C_nmim]^+$ and $[C_{n-2}mim]^+$ cations is observed at collision energies in excess of 4.5 eV. The 3-methylimidazolium cation, $[C_4H_7N_2]^+$, formed via neutral loss of the 1-alkyl substituent is the dominant species observed. Other $[C_nH_{2n+1}]^+$ cation series that arise from cleavage along and charge retention by the 1-alkyl substituent are also observed. The sequential dissociation pathways observed here for the $[C_nmim]^+$ cations parallel those observed in the CID of the $[2C_nmim{:}BF_4]^+$ clusters and have been detailed previously;[21] present results are summarized in **Table S1** of the Supporting Information.

The energy-dependent CID behavior observed for all three $[C_{n-2}mim{:}BF_4{:}C_nmim]^+$ clusters is highly parallel (see **Figure 2)**. The cross section shapes are very similar, but the cross section magnitudes and apparent onsets do exhibit systematic variation. As both the absolute binding energies and trends in the binding of these clusters are of great interest, the total CID cross sections and the $[C_nmim]^+$ and $[C_{n-2}mim]^+$ primary product cross sections are compared in greater detail in **Figure 3**. As can be seen in the expanded overlays shown in the figure, the apparent thresholds for the total CID cross sections as well as the $[C_nmim]^+$ and $[C_{n-2}mim]^+$ primary product cross sections all increase in the order: 2:4 < 4:6 < 6:8 where n-2:n denotes the $[C_{n-2}mim{:}BF_4{:}C_nmim]^+$ cluster, suggesting that the binding is the weakest for the cluster involving the smallest cations and increases slightly with increasing size of the cations, or equivalently with increasing length of the 1-alkyl substituents. However, extracting meaningful trends from such simple analyses of the apparent CID thresholds can be problematic, especially for systems that exhibit very minor differences in their energy dependences. This is particularly true for the $[C_{n-2}mim{:}BF_4{:}C_nmim]^+$ clusters examined here as the effects of the size of the cations on the internal energy and lifetime for dissociation should shift the observed CID cross sections in opposite directions, and the magnitudes of these effects may differ. However, comparison of the apparent thresholds for the $[C_nmim]^+$ and $[C_{n-2}mim]^+$ primary product cross sections makes it clear that binding to the larger cation is weaker. Therefore, the trends in the apparent thresholds make it clear that lifetime effects are increasing the apparent thresholds to a greater extent than

the increased internal energy available in the larger clusters decreases the apparent threshold. Simultaneous thermochemical analyses of the competitive dissociation behavior will provide quantitative assessment of the relative $[C_nmim]^+$ cation affinities for $[BF_4]^-$.

Theoretical Results. Stable structures and energetics of the $[C_{n-2}mim:BF_4:C_nmim]^+$ clusters were calculated as described in the Theoretical calculations section. The structures and stabilities of the $[C_nmim]^+$ and $[BF_4]^-$ ions and ($C_nmim:BF_4$) ion pairs are taken from our initial study.[21] Details of the B3LYP, B3LYP-GD3BJ, and M06-2X geometry optimized structures of the ground conformers of the $[C_nmim]^+$ cations, $[BF_4]^-$ anion, ($C_nmim:BF_4$) ion pairs, and $[C_{n-2}mim:BF_4:C_nmim]^+$ clusters are given in **Tables S2-S5** of the Supporting Information.

Nomenclature. In our initial study of 1-alkyl-3-methylimidazolium tetrafluoroborate clusters,[21] we defined a nomenclature to differentiate the stable conformations of the $[C_nmim]^+$ cations, ($C_nmim:BF_4$) ion pairs, and $[2C_nmim:BF_4]^+$ clusters as described in detail in **Figure S1** of the Supporting Information. This nomenclature was designed to describe the nature of the cation-anion binding interaction, and the conformations and relative orientations of the cations to facilitate recognition of structural elements. Further, the nomenclature also provides parallel naming for the mixed $[C_{n-2}mim:BF_4:C_nmim]^+$ clusters examined here as well as clusters of other $C_n$mim-anion IL clusters currently being examined in related studies. The following discussion will focus primarily on the B3LYP and M06-2X as B3LYP-GD3BJ exhibits results that are nearly identical to one or the other of the former theoretical methods.

$[C_nmim]^+$. Geometric parameters of the B3LYP, B3LYP-GD3BJ, and M06-2X geometry-optimized structures of the ground conformers of the $[C_nmim]^+$ cations are summarized in **Table S2**. To visualize noncovalent interactions within these cations, NCI plots have been superimposed on the B3LYP and M06-2X ground conformers of the $[C_nmim]^+$ cations in **Figure 4**. The 3-methylimidazolium moiety common to all four $[C_nmim]^+$ cations takes on the same nearly planar conformation in all of the stable structures found such that stable conformers differ only in the conformation of the 1-alkyl substituent. Therefore, the $[C_nmim]^+$ cations are simply denoted by a series of dihedral angles (a1...an that describe the conformation of the

1-alkyl substituent) enclosed in square brackets and superscripted with a plus sign to indicate that they are cations, $[a1...an]^+$. See **Figure S1** for definitions of the an dihedral angles and their cis, gauche(+), trans, and gauche(-) designations.

In the B3LYP ground conformers of the $[C_nmim]^+$ cations, the 1-alkyl substituents adopt anti-staggered orientations to minimize steric repulsion and are described as $[g.]^+$, $[g.t_2]^+$, $[g.t_4]^+$, and $[g.t_6]^+$ for n = 2, 4, 6, and 8, respectively. Of note, the g_+ and g. designations for the a1 dihedral angle differentiate enantiomeric structures such that there are also energetically equivalent B3LYP ground conformations of the $[C_nmim]^+$ described as $[g_+]^+$, $[g_+t_2]^+$, $[g_+t_4]^+$, and $[g_+t_6]^+$, respectively. The NCI surfaces visible in the B3LYP optimized structures show no intramolecular stabilizing interactions. The ground conformers of the $[C_nmim]^+$ cations determined via M06-2X and B3LYP-GD3BJ optimization are similar to those determined by B3LYP except that twisting of the 1-alkyl chain to enable noncovalent interactions with the π cloud of the imidazolium ring is observed in these conformations. A weak interaction between the C2′ hydrogen atom and the C5 carbon atom of the imidazolium ring is evident in the NCI maps for all four cations. For the three largest cations, the longer 1-alkyl chain enables a much stronger noncovalent interaction between the C3′ hydrogen atom and the π cloud of the imidazolium ring (see **Figure 4**). The excess charge is delocalized along the entire surface of the $[C_nmim]^+$ cation such that all of the hydrogen atoms provide favorable sites for accepting electron density from the anion. The charge of the imidazolium ring hydrogen atoms exceeds that of the alkyl chain hydrogen atoms, with the C2 hydrogen atom exhibiting the greatest Mülliken charge. Additional details regarding the ground and other stable low-energy conformations of the $[C_nmim]^+$ cations computed can be found in our initial study of the $[2C_nmim{:}BF_4]^+$ clusters.[21]

$[BF_4]^-$. Geometric parameters of the B3LYP, B3LYP-GD3BJ, and M06-2X geometry-optimized structures of $[BF_4]^-$ are summarized in **Table S3**. Noncovalent interactions within this anion are visualized as a superimposed NCI plot on the B3LYP and M06-2X optimized structures of $[BF_4]^-$ anion in **Figure 4**. Only a single stable ideal tetrahedral geometry was found for each theoretical model. However, the B–F bond lengths in the M06-2X structure

are slightly shorter than those computed by B3LYP and B3LYP-GD3BJ. The lone pairs of electrons on the fluorine atoms provide favorable sites for donation of electron density to the $[C_n\text{mim}]^+$ cations.

($C_n$mim:BF_4). Geometric parameters of the B3LYP, B3LYP-GD3BJ, and M06-2X geometry-optimized structures of the ground conformers of the ($C_n$mim:BF_4) ion pairs are summarized in **Table S4**. NCI plots have been superimposed on the B3LYP and M06-2X ground conformers of the ($C_n$mim:BF_4) cations in **Figure 5** to visualize noncovalent interactions within these ion pairs. The geometries of the isolated $[C_n\text{mim}]^+$ cation and $[BF_4]^-$ anion are only modestly perturbed upon binding. In all of the ground conformers, regardless of the theory employed, binding occurs via noncovalent interactions between the C1′, C2, and C1″ hydrogen atoms of the $[C_n\text{mim}]^+$ cation and two of the F atoms of the $[BF_4]^-$ anion. Additional stabilization is garnered through an anion-π interaction between a third F atom and the π-cloud of the imidazolium ring. As for the isolated cations, the 1-alkyl substituent takes on an anti-staggered geometry in the B3LYP structures, but can fold to achieve additional interactions with the anion particularly for the larger cations and the B3LYP-GD3BJ and M06-2X structures. These noncovalent interactions are easily seen in the NCI plots of **Figure 5** as the cation-anion interaction polarizes the electron density toward the interaction surfaces. Here again, the NCI surfaces of the B3LYP structures are less extensive than those determined using M06-2X. The cation-anion distance does not vary with the cation across the ($C_n$mim:BF_4) ion pair series, but does depend on the theoretical model employed with B3LYP finding a larger separation than B3LYP-GD3BJ and M06-2X.

The intrinsic binding interactions of the ground conformers of the ($C_n$mim:BF_4) ion pairs are conserved across the cation series and the various levels of theory examined. However, other less favorable modes of binding were also found among the stable conformers. Therefore, the ($C_n$mim:BF_4) ion pairs are denoted by the mode of binding and the dihedral angles that describe the conformation of the 1-alkyl substituent enclosed in parentheses and with no charge to indicate that these conformers are neutral ion pairs, (**b1BS**;a1...an). See **Figure S1** for the various

binding site designations, which provide details of the location and orientation of the binding interactions.

The B3LYP and M06-2X ground conformers of the ($C_n$mim:BF_4) ion pairs all exhibit front-side binding (**F**), but several favorable orientations as described by the **b1** dihedral angle are found including $\mathbf{g}_+$, $\mathbf{g}_-$, and **c**. The 1-alkyl substituents adopt anti-staggered orientations in which the 1-alkyl substituent partially wraps around the anion to achieve additional stabilization. The B3LYP ground conformers are described as ($\mathbf{g}_+$**F**;g_-), ($\mathbf{g}_+$**F**;$g_{-2}t$), (**cF**;g_-t_4), and (**cF**;$g_{-2}t_5$), whereas the M06-2X ground conformers are described as (**g**$_-$**F**;g_-), ($\mathbf{g}_+$**F**;cg$_-$t), (**g**$_-$**F**;g_-t_4), and (**g**$_-$**F**;$g_-t_2g_{+2}t_2$) for n = 2, 4, 6, and 8, respectively. Additional structural and energetic information for the ground and other stable low-energy conformations of the ($C_n$mim:BF_4) ion pairs computed can be found in our initial study of the $[2C_n\text{mim:}BF_4]^+$ clusters.[21]

$[C_{n-2}$mim:BF_4:$C_n$mim$]^+$. Geometric parameters of the B3LYP, B3LYP-GD3BJ, and M06-2X geometry-optimized structures of the ground conformers of the $[C_{n-2}\text{mim:}BF_4\text{:}C_n\text{mim}]^+$ clusters are summarized in **Table S4**. Noncovalent interactions within these clusters are again visualized by superimposing NCI plots on the B3LYP and M06-2X ground conformers in **Figure 6**.

Not surprisingly, the stable structures of the $[C_{n-2}\text{mim:}BF_4\text{:}C_n\text{mim}]^+$ clusters are quite parallel to those found for the $[2C_n\text{mim:}BF_4]^+$ clusters. Binding in the ground conformers of the $[C_{n-2}\text{mim:}BF_4\text{:}C_n\text{mim}]^+$ clusters also occurs via noncovalent interactions between the C1′, C2, and C1″ hydrogen atoms of each of the cations and two of the F atoms of the $[BF_4]^-$ anion. However, the presence of the second cation blocks the anion-π interaction between a third F atom and the π-cloud of the imidazolium ring that provides additional stabilization to the ($C_n$mim:BF_4) ion pairs. The 1-alkyl substituents again take on anti-staggered geometries in the B3LYP structures, but can fold to achieve additional interactions with the anion particularly for the larger cations and the B3LYP-GD3BJ and M06-2X structures. The imidazolium rings are nearly planar with the tetrahedron BF_2 edges of the anion in the B3LYP structures, whereas the M06-2X structures lie out of the plane producing somewhat more compact structures.

These noncovalent interactions are easily seen in the NCI plots of **Figure 6** as the cation-anion interactions polarize electron density toward the interaction surfaces. The NCI surfaces of the B3LYP structures clearly show these interactions as being localized between the interacting atoms, whereas the NCI surfaces of the M06-2X structures are much more extensive and also exhibit interactions with the 1-alkyl substituents. The B3LYP cation-anion distances do not vary significantly with the cation across the $[C_{n-2}mim:BF_4:C_nmim]^+$ cluster series, but do exhibit modest variation for the B3LYP-GD3BJ and M06-2X structures. Notably in several of the B3LYP-GD3BJ and M06-2X ground conformers, the cation-anion interaction distances differ with the smaller cation exhibiting a shorter interaction distance. As for the ($C_nmim:BF_4$) ion pairs, B3LYP finds larger separations than B3LYP-GD3BJ and M06-2X.

The intrinsic binding interactions of the ground conformers of the $[C_{n-2}mim:BF_4:C_nmim]^+$ clusters are again conserved across the cation series and the various levels of theory examined. The involvement of the 1-alkyl substituent in the binding however increases for the larger cations for B3LYP-DG3BJ and M06-2X, as well as for higher-energy B3LYP conformers. We chose to limit calculations performed here to low-energy modes of binding as other modes of binding are sufficiently less favorable as to be unimportant experimentally, but maintain a parallel naming scheme for consistency. The $[C_{n-2}mim:BF_4:C_nmim]^+$ clusters are denoted by the modes of binding and the dihedral angles that describe the conformations of the 1-alkyl substituents enclosed in square brackets and superscripted with a plus sign to indicate that they are cations, [a1...an-2:**b2BS1**(n-2)**BS2**(n):a1...an]$^+$. To facilitate recognition, the 1-alkyl orientation of the $[C_{n-2}mim]^+$ cation and its binding mode is given first. See **Figure S1** for the various binding site designations, which provide details of the locations and orientations of the binding interactions, and the relative orientations of the 1-alkyl substituents.

The B3LYP and M06-2X ground conformers of the $[C_{n-2}mim:BF_4:C_nmim]^+$ clusters exhibit front-side binding of both cations (**FF**), except for the M06-2X conformer of $[C_4mim:BF_4:C_6mim]^+$, which exhibits $\mathbf{F_mF}$ binding. The binding orientations as described by the **b1** dihedral angles are generally **c**, but a **g**- orientation of one of the cations is found in the

M06-2X conformer of $[C_2mim{:}BF_4{:}C_4mim]^+$. The 1-alkyl substituents adopt anti-staggered orientations in which the 1-alkyl substituents partially wrap around the anion to achieve additional stabilization. The relative orientations of the 1-alkyl substituents as described by the **b2** dihedral angle are generally $\mathbf{g}_+$ or $\mathbf{g}_-$, but the $[C_4mim{:}BF_4{:}C_6mim]^+$ cluster again deviates with a **t** orientation. The B3LYP ground conformers are described as $[g_-;\mathbf{g_-cFcF};g_-t_2]^+$, $[g_-t_2;\mathbf{g_+cFcF};g_-t_4]^+$, and $[g_-t_4;\mathbf{g_+cFcF};g_+t_6]^+$, whereas the M06-2X ground conformers are described as $[g_-;\mathbf{g_+g_-FcF};g_{+2}t]^+$, $[g_+g_{-2};\mathbf{tcF_mcF};g_-g_+t_3]^+$, and $[g_+g_-t_2g;\mathbf{g_-cFcF};g-g_{+2}t_2g_+t]^+$ for n = 4, 6, and 8, respectively. Additional structural and energetic information for the ground and other stable low-energy conformations of the $[C_{n-2}mim{:}BF_4{:}C_nmim]^+$ clusters computed can be found in **Figures S2**, which shows ESP maps of the ground conformers and in **Figures S3-S5**, which show the ground and stable low-energy conformers of the $[C_{n-2}mim{:}BF_4{:}C_nmim]^+$ clusters along with their B3LYP, B3LYP-GD3BJ, and M06-2X relative stabilities.

Theoretical estimates for the BDEs of the $[C_{n-2}mim{:}BF_4{:}C_nmim]^+$ and $[2C_nmim{:}BF_4]^+$ clusters are predicted based on the computed ground conformers of these clusters and the various $[C_nmim]^+$ cations and $(C_nmim{:}BF_4)$ ion pairs. As described earlier, the clusters dissociate via loss of a neutral ion pair; a single primary CID pathway is observed for the $[2C_nmim{:}BF_4]^+$ clusters (**reaction 1**), whereas two competing primary CID pathways occur in competition for the mixed clusters (**reactions 7** and **8**). Theoretical estimates for the IPEs of the $(C_nmim{:}BF_4)$ ion pairs are also predicted based on the computed ground conformers of the various $[C_nmim]^+$ cations and the $[BF_4]^-$ anion. Relative IPEs of the $(C_nmim{:}BF_4)$ ion pairs and relative BDEs of the $[C_{n-2}mim{:}BF_4{:}C_nmim]^+$ and $[2C_nmim{:}BF_4]^+$ clusters are also computed based on the predicted absolute IPEs and BDEs.

Threshold Analysis of CID Cross Sections. The threshold regions of the zero-pressure extrapolated cross sections for the primary CID pathways, **reactions 7** and **8**, observed for three $[C_{n-2}mim{:}BF_4{:}C_nmim]^+$ clusters were simultaneously modeled using the empirical threshold law of **eq 6** as described in the **Thermochemical Analysis** section. These simple noncovalent bond cleavage reactions were modeled using a loose phase space limit transition state (PSL TS)

model.[55,56] Previous work has established the PSL TS model as providing the most accurate determination of threshold energies for CID reactions of such noncovalently bound complexes.[66-73] Representative analyses for all three clusters are shown in **Figure 7**. As can be seen in the figure, the PSL TS model reproduces the primary CID product cross sections for all three $[C_{n-2}mim:BF_4:C_nmim]^+$ clusters with high fidelity over energy ranges exceeding 3.5 eV and cross sections magnitudes of at least 100. Results of these analyses are summarized in **Table 1**. The primary CID product cross sections were also independently modeled using the empirical threshold law of **eq 5**; results of these analyses are summarized in **Table S8**. Comparison of results of analyses using **eq 5** and **eq 6** enable competitive shifts in the CID product cross sections to be quantitatively assessed. The primary CID product cross sections were also independently modeled using **eq 4** in two ways, in the first the *n* values for both pathways are fixed at the value determined from analysis with **eq 6**, and in the second, the *n* values for are set at the values determined from **eq 5**. Comparison of results of analyses for **eq 4** and **eq 6** and likewise comparisons of analyses using **eq 4** and **eq 5** enable kinetic shifts to be quantitatively assessed. Results of analyses using **eq 4** are also summarized in **Table 1** and **Table S8**. For all of these analyses, the molecular parameters are taken from the B3LYP optimized structures of the ground conformers of the precursor $[C_{n-2}mim:BF_4:C_nmim]^+$ cluster and its CID products, which are summarized in **Tables S6** and **S7**.

Kinetic Shifts. The differences between the threshold values determined including lifetime effects (**eq 6** and **eq 5**), E_0(PSL), and those excluding lifetime effects (**eq 4**), E_0, provide quantitative assessment of the kinetic shifts in the experimental data and are also given in **Table 1** and **Table S8**. The kinetic shifts are appreciable and vary with the size of the cluster. The kinetic shifts are smallest for the $[C_2mim:BF_4:C_4mim]^+$ cluster with values of 0.78 and 0.88 eV when modeled simultaneously, and 0.85 and 0.79 eV when modeled independently. The kinetic shifts are somewhat larger for the $[C_4mim:BF_4:C_6mim]^+$ cluster with values of 1.14 and 1.11 eV when modeled simultaneously, and 1.08 and 1.15 eV when modeled independently. The kinetic shifts are largest for the $[C_4mim:BF_4:C_6mim]^+$ cluster with values of 1.42 and 1.42 eV when

modeled simultaneously, and 1.40 and 1.41 eV when modeled independently. Trends in the kinetic shifts are easily rationalized based on the number of vibrational modes available to these systems, which increase from 141 to 177 to 213, respectively. The very minor differences in the kinetic shifts determined from analyses that include and exclude the effects of competition indicate that the energetics for both dissociation pathways are very similar.

Competitive Shifts. The differences between the threshold values, E_0(PSL), determined including and excluding competitive effects (**eq 6** and **eq 5**), provide quantitative assessment of the competitive shifts in the experimental data and are rather small for these systems. The threshold values for **reactions 7** are reduced by 0.03 eV, whereas the threshold values for reactions 8 increase by 0.04 to 0.09 eV when competition is included. These results are consistent with previous findings where errors resulting from "completive shifts" were found to be small when thresholds differ by ~0.1 eV.[56]

The entropy of activation, $\Delta S^{\dagger}$, is a measure of the looseness of the TS but also depends on the size and complexity of the system. The entropy of activation is determined as the entropy difference between the TS using used to model the data and the reactants. The $\Delta S^{\dagger}$(PSL) values at 1000 K determined for analyses using **eq 6** and **eq 5** are included in **Table 1** and **Table S8**. The values exhibit only modest variation and vary between 17 and 44 J mol^{-1} K^{-1} across these systems. The values of $\Delta S^{\dagger}$ are positive as expected for unimolecular dissociation reactions of noncovalently bound systems and in particular for modeling using a loose PSL TS as employed here. These values compare favorably to $\Delta S^{\dagger}$ values previously determined for CID of noncovalently bound complexes that have been previously measured in our laboratory.[66-72]

Conversion from 0 to 298 K. Although TCID measurements are typically performed at room temperature as for the systems examined here, the values extracted from thermochemical analysis correspond to enthalpies of dissociation at 0 K. The 0 K enthalpies (or BDEs in this case) are converted to 298 K enthalpies and free energies to facilitate comparisons to values typically reported in the literature. The enthalpy and entropy conversions are calculated using standard formulas, which employ harmonic oscillator and rigid rotor models to predict the vibrational

frequencies and rotational constants determined from the B3LYP optimized geometries, given in **Tables S6** and **S7** of the Supporting Information. **Table 3** lists the 0 and 298 K enthalpy, free energy, and entropic corrections for all systems experimentally determined. Uncertainties in the enthalpic and entropic corrections are estimated by 10% variation in the vibrational frequencies.

DISCUSSION

Comparison of Theory and Experiment: The ability of the B3LYP, B3LYP-GD3BJ and M06-2X theoretical approaches employed here to describe the intrinsic cation-anion interactions in the ($C_n$mim:BF_4) ion pairs and $[2C_n\text{mim:}BF_4]^+$ and $[C_{n-2}\text{mim:BF4:}C_n\text{mim}]^+$ clusters is evaluated comprehensively. First comparisons between the measured and computed BDEs of the $[2C_n\text{mim:}BF_4]^+$ clusters previously determined are reviewed.[21] Next, comparisons are made between the measured and computed BDEs of the $[C_{n-2}\text{mim:}BF_4\text{:}C_n\text{mim}]^+$ clusters determined here. Finally, the computed relative BDEs of the $[2C_n\text{mim:}BF_4]^+$ clusters and relative IPEs of the ($C_n$mim:BF_4) ion pairs are compared to those estimated from the measured relative BDEs of the $[C_{n-2}\text{mim:}BF_4\text{:}C_n\text{mim}]^+$ clusters determined here via competitive TCID measurements.

$[2C_n\text{mim:}BF_4]^+$ BDEs. Excellent agreement between the TCID measured BDEs of the $[2C_n\text{mim:}BF_4]^+$ clusters and those predicted by B3LYP and B3LYP-GD3BJ was previously found.[21] For both theories, the mean absolute deviation (MAD) between the computed and measured values, 1.8 ± 1.4 kJ/mol and 1.9 ± 1.3 kJ/mol are smaller than the average experimental uncertainty (AEU) in the measured values, 5.4 ± 1.0 kJ/mol. In contrast, the BDEs predicted by M06-2X exhibit much poorer agreement with the measured values. The MAD for M06-2X vs. the TCID measured values is 11.3 ± 5.7 kJ/mol, which is more than twice as large as the AEU in these values. When BSSE corrections are not included for M06-2X, the agreement improves significantly and the MAD reduces to 4.0 ± 5.1 kJ/mol. Overall comparisons suggest that the B3LYP values are most reliable, but B3LYP-GD3BJ also predicts energetics for these systems very well. In contrast, M06-2X systematically underestimates the strength of binding

however, the predicted BDEs exhibit reasonable agreement when BSSE corrections are excluded.

$[C_{n-2}mim:BF_4:C_nmim]^+$ BDEs. The TCID measured BDEs of the $[C_{n-2}mim:BF_4:C_nmim]^+$ clusters are compared to the B3LYP, B3LYP-GD3BJ, and M06-2X computed values in **Table 2** and **Figure 8**. The experimental values listed in the table and plotted in the figure are determined from threshold analyses based on the B3LYP optimized geometries of the precursor $[C_{n-2}mim:BF_4:C_nmim]^+$ cluster and its primary dissociation products. As found for the $[2C_nmim:BF_4]^+$ clusters, B3LYP and B3LYP-GD3BJ predict BDEs that are in excellent agreement with the values determined from the TCID measurements. The MADs between the TCID measured BDEs and the B3LYP and B3LYP-GD3BJ calculated values are 2.5 ± 3.3 kJ/mol and 3.2 ± 2.4 kJ/mol. M06-2X does not perform quite as well; the MAD is more than twice as large, 6.6 ± 5.1 kJ/mol. When BSSE corrections are not included, the MAD decreases only slightly to 6.5 ± 4.0 kJ/mol. Recall that M06-2X systematically underestimated the strength of binding in the $[2C_nmim:BF_4]^+$ clusters, which may suggest that in spite of our comprehensive sampling of those systems that the true M06-2X ground conformers may not have been found. These comparisons again suggest that the B3LYP values are the most reliable. Further, B3LYP-GD3BJ also predicts energetics for these systems quite well, whereas M06-2X does not perform quite as well, but still does a reasonable job.

$[C_{n-2}mim:BF_4:C_nmim]^+$ Relative BDEs. The TCID measured relative BDEs of the $[C_{n-2}mim:BF_4:C_nmim]^+$ clusters are compared to B3LYP, B3LYP-GD3BJ, and M06-2X computed values in **Table 4** and **Figure 9**. The experimental values listed in the table and plotted in the figure are again those determined from threshold analyses based on the B3LYP optimized geometries of the precursor $[C_{n-2}mim:BF_4:C_nmim]^+$ cluster and its primary dissociation products. The theoretical values are computed in two different ways, first as the relative BDEs (ΔBDEs) of the $[C_{n-2}mim:BF_4:C_nmim]^+$ clusters and their dissociation products (**reactions 7** and **8**), and second as the relative ion pairing energies (ΔIPEs) of the ($C_nmim:BF_4$) and ($C_{n-2}mim:BF_4$) ion pairs. The differences in the B3LYP computed ΔBDEs vs. ΔIPEs is very small (0 to 0.7 kJ/mol),

but slightly larger for B3LYP-GD3BJ (0.3 to 1.8 kJ/mol), and M06-2X (0.2 to 2.9 kJ/mol). The MADs between the TCID measured ΔBDEs and the B3LYP computed ΔBDEs and ΔIPEs are 2.4 ± 2.4 kJ/mol and 2.4 ± 2.0 kJ/mol. B3LYP-GD3BJ performs almost as well with MADs between the TCID measured ΔBDEs and the B3LYP-GD3BJ computed values of are 4.1 ± 2.7 kJ/mol and 3.3 ± 2.1 kJ/mol. The performance of M06-2X is slightly poorer, but still reasonable, with MADs of 5.8 ± 6.0 kJ/mol and 3.9 ± 5.1 kJ/mol. All three levels of theory find slightly better agreement between the measured ΔBDEs and the calculated ΔIPEs than the calculated ΔBDEs. Further, these comparisons again suggest that the B3LYP values are the most reliable, but that both B3LYP-GD3BJ and M06-2X also predict energetics for these systems reasonably well.

Ion Pairing Energies. Based on these findings, we report theoretical estimates for the absolute IPEs of the ($C_n$mim:BF_4) ion pairs, which are summarized in **Table 5**. For all three theoretical models, the computed IPEs are quite large and nearly three times as large at the BDEs measured and predicted for the $[2C_n\text{mim:}BF_4]^+$ and $[C_{n-2}\text{mim:}BF_4\text{:}C_n\text{mim}]^+$ clusters, and generally decrease with increasing size of the cation. The IPEs predicted by B3LYP are the weakest ~ 337 kJ/mol, increase for B3LYP-GD3BJ to ~ 357 kJ/mol, and increase further to ~ 373 kJ/mol for M06-2X. Interestingly, the predicted relative order of binding in the ($C_n$mim:BF_4) ion pairs differs from that of the $[2C_n\text{mim:}BF_4]^+$ clusters for each level of theory, again suggesting that uncertainties in the theoretical values are larger than the differences being estimated.

Evaluated $[2C_n\text{mim:}BF_4]^+$ BDEs. As discussed above, the variation in the BDEs of the $[2C_n\text{mim:}BF_4]^+$ clusters determined from independent TCID experiments is rather small, and similar in magnitude to the AEU in these determinations.[21] Thus, the absolute order of the intrinsic binding interactions as a function of the cation cannot be established solely from these measurements. However, the competitive dissociation behavior of the $[C_{n-2}\text{mim:}BF_4\text{:}C_n\text{mim}]^+$ clusters examined here definitively establish the relative order of binding of the $[2C_n\text{mim:}BF_4]^+$ clusters as a function of the cation as: $[C_8\text{mim}]^+ < [C_6\text{mim}]^+ < [C_4\text{mim}]^+ < [C_2\text{mim}]^+$. Further, the relative BDEs determined here provide additional constraints on the absolute energetics of

binding in these clusters, and with reduced uncertainties. By combining the absolute BDEs of the $[2C_nmim:BF_4]^+$ clusters with the relative BDEs determined here and subjecting the results to linear regression / maximum likelihood analysis using OriginPro 8.6.0 (OriginLab Corporation, Northampton, MA, USA), improved estimates of the BDEs of the $[2C_nmim:BF_4]^+$ clusters are determined. The results of these combined analyses are summarized in **Table 6** and shown in **Figure 10**. The absolute BDEs of the $[2C_nmim:BF_4]^+$ clusters previously determined from independent TCID measurements are plotted in the top panel of **Figure 10**. As can be seen in the figure, the ranges these BDEs span exhibit significant overlap due to the experimental uncertainties, making it impossible to definitively establish a relative order of binding. The relative BDEs of the $[2C_nmim:BF_4]^+$ clusters, which are approximated as by the relative BDEs of the $[C_{n-2}mim:BF_4:C_nmim]^+$ clusters determined from competitive TCID measurements (as validated above) are plotted in the center panel of **Figure 10**. Combined, this thermochemistry provides an over-determined system of equations that was solved to extract BDEs of the $[2C_nmim:BF_4]^+$ clusters with improved accuracy and precision as shown in the bottom panel of **Figure 10**. The trend in the resultant BDEs is now consistent with the competitive measurements. Further, the ranges these BDEs span now exhibit very little overlap due to the experimental uncertainties, firmly establishing the relative order of binding as $[C_8mim]^+ < [C_6mim]^+ < [C_4mim]^+ < [C_2mim]^+$.

The BDEs of the $[2C_nmim:BF_4]^+$ clusters originally measured as well as those derived from the regression analysis are compared with the theoretically predicted BDEs in **Figure 11**. The agreement between the measured BDEs derived from the regression analysis and the B3LYP, B3LYP-GD3BJ, and M06-2X calculated BDEs is reasonably good with MADs of 3.7 ± 2.0 kJ/mol, 5.0 ± 4.7 kJ/mol, and 4.3 ± 1.9 kJ/mol, respectively. However, in all cases, the agreement between theory and experiment slightly degrades from the directly measured vs. evaluated BDEs. Overall, these results suggest that all three levels of theory are able to provide a reasonable description of the binding in these systems with B3LYP providing the best performance, but that

the theoretically predicted energetics of binding is not able to differentiate the small differences in the binding in these systems accurately.

Influence of the $C_n$mim-BF4 IL for Space Propulsion. The BDEs of the $[C_{n-2}mim:BF_4:C_nmim]^+$ and $[2C_nmim:BF_4]^+$ clusters measured and determined here provide additional thermochemistry relevant to the $C_n$mim-BF_4 ILs that can be used to improve modeling of the dissociation dynamics of these ILs relevant to electrospray propulsion. Further, the present measurements firmly establish the intrinsic order of binding as a function of the cation among these clusters as $[C_8mim]^+ < [C_6mim]^+ < [C_4mim]^+ < [C_2mim]^+$. The very small variation in the energetics of binding as the cation is varied indicate that all four of these $C_n$mim-BF_4 ILs should provide similar thrust for space propulsion applications when the electrospray thruster is tuned to produce primarily the $[2C_nmim:BF_4]^+$ clusters. However, packing effects among the $C_n$mim-BF_4 ILs may differ as a function of the cation such that differences in propulsion efficiency may be found when the electrospray thrusters are tuned to produce larger clusters or cluster distributions. Extending these studies to larger clusters should elucidate packing effects and provide additional insight into the relative ability of these $C_n$mim:BF_4 ILs to serve as fuels for electrospray propulsion.

CONCLUSIONS

Threshold collision-induced dissociation techniques were previously employed to examine the energy-dependent dissociation behavior and determine the bond dissociation energies (BDEs) of the 2:1 clusters of 1-alkyl-3-methylimidazolium cations and tetrafluoroborate, $[2C_nmim:BF_4]^+$.[21] Four $[C_nmim]^+$ cations with 1-alkyl substituents of variable length were included in that work to examine the structural and energetic effects of the size of the 1-alkyl substituent on the binding. Complementary electronic structure calculations were performed to determine the structures, energetics, and binding preferences in these clusters. Several theoretical models, B3LYP, B3LYP-GD3BJ, and M06-2X, using the 6-311+G(d,p) basis set for geometry optimizations and frequency analyses and the 6-311+G(2d,2p) basis set for energetics, were

benchmarked to evaluate their abilities to describe the nature of the binding interactions and to reproduce the measure BDEs. The variation in the BDEs of the $[2C_nmim:BF_4]^+$ clusters was found to be similar to the AEU in the values such that trends in the BDEs as a function of the cation were indiscernible. B3LYP and B3LYP-GD3BJ were found to describe these systems very well, whereas M06-2X did not perform quite as well, but still provided reasonable agreement.

To properly resolve the absolute order of binding of the $[C_nmim]^+$ cations in the $[2C_nmim:BF_4]^+$ clusters, competitive TCID measurements and electronic structure calculations were performed to characterize the dissociation behavior and determine the BDEs of three mixed $[C_{n-2}mim:BF_4:C_nmim]^+$ clusters, n = 4, 6, and 8. Again the variation in the BDEs of these clusters is found to be similar to the AEU in the values, such that the relative order of binding based on these values remains indeterminate. The competitive dissociation behavior examined here however, definitively establishes the relative order of binding among all three clusters as $[C_nmim]^+ < [C_{n-2}mim]^+$. Further, simultaneous thermochemical analyses of the competitive TCID data provide relative BDEs for these clusters with significantly improved precision. Maximum likelihood analyses based on the absolute BDEs of the $[2C_nmim:BF_4]^+$ clusters and the relative BDEs of the $[C_{n-2}mim:BF_4:C_nmim]^+$ clusters determined here provide more accurate and precise estimates of the BDEs of the $[2C_nmim:BF_4]^+$ clusters. The evaluated BDEs of the $[2C_nmim:BF_4]^+$ clusters conclusively reveal the absolute order of binding among these clusters to follow the order: $[C_8mim]^+ < [C_6mim]^+ < [C_4mim]^+ < [C_2mim]^+$. Overall, B3LYP is found to best describe the binding in $C_nmim\text{-}BF_4$ IL clusters. Although B3LYP-DG3BJ and M06-2X include dispersion and extensive parameterization, which should in principle provide more accurate descriptions of noncovalent binding interactions, present results indicate that they do not provide improved estimates for the energetics of binding in $C_nmim\text{-}BF_4$ IL clusters.

The very small variation in the energetics of binding as the cation is varied suggest that all four $C_nmim\text{-}BF_4$ ILs (n = 2, 4, 6 and 8) should provide similar efficiencies for high thrust operation of electrospray thrusters. However, packing effects may differ as a function of the cation such that differences in propulsion efficiency may be found when the electrospray

thrusters are tuned for lower thrust operation Studies of larger clusters should elucidate packing effects and provide additional insight into the relative ability of these $C_n$mim:BF_4 ILs to serve as fuels for electrospray propulsion.

ASSOCIATED CONTENT

Supporting Information. Tables summarizing CID fragments of the $[C_{n-2}mim:BF_4:C_nmim]^+$ cluster ions; geometric parameters of the ground conformers of the $[C_nmim]^+$ cations, $[BF_4]^-$ anion, ($C_n$mim:BF_4) ion pairs, and $[C_{n-2}mim:BF_4:C_nmim]^+$ clusters, molecular (vibrational and rotational) constants determined from B3LYP/6-311+G(d,p) optimized geometries of the $[C_{n-2}mim:BF_4:C_nmim]^+$ clusters, ($C_n$mim:BF_4) ion pairs, and $[C_nmim]^+$ cations employed in the thermochemical analysis of the experimental data; fitting parameters of eq 5 for threshold determinations in which the two primary CID product cross sections are fitted independently. Figures describing the nomenclature used to differentiate various stable conformations of the $[C_{n-2}mim:BF_4:C_nmim]^+$ clusters, ($C_n$mim:BF_4) ion pairs, and $[C_nmim]^+$ cations; ESP maps of the B3LYP/6-311+G(2d,2p) ground conformers of the $[C_{n-2}mim:BF_4:C_nmim]^+$ clusters; ground and select stable conformations of the $[C_{n-2}mim:BF_4:C_nmim]^+$ clusters found at the B3LYP/6-311+G(d,p), B3LYP-GD3BJ/6-311+G(d,p), and M06-2X/6-311+G(d,p) levels of theory along with their relative Gibbs free energies determined at the same levels of theory with a 6-311+G(2d,2p) basis set are provided. This material is available free of charge at http://pubs.acs.org

AUTHOR INFORMATION

Notes. The authors declare no competing financial interest.

ACKNOWLEDGMENTS

Financial support for this work was provided by the National Science Foundation, CHE-1709789. Computational resources were provided by Wayne State University C&IT. The

authors acknowledge support from the Wayne State University Summer Dissertation Fellowship for HAR.

ORCID

Harrison A. Roy https://orcid.org/0000-0002-9128-5245

Mary T. Rodgers https://orcid.org/0000-0002-5614-0948

REFERENCES

(1) MacFarlane, D. R.; Kar, M.; Pringle, J. M., *Fundamentals of Ionic Liquids: From Chemistry to Applications*. John Wiley & Sons: 2017.

(2) Liu, H.; Liu, Y.; Li, J., Ionic liquids in Surface Electrochemistry. *Phys. Chem. Chem. Phys.* **2010**, *12*, 1685-1697.

(3) MacFarlane, D. R.; Forsyth, M.; Howlett, P. C.; Pringle, J. M.; Sun, J.; Annat, G.; Neil, W.; Izgorodina, E. I., Ionic Liquids in Electrochemical Devices and Processes: Managing Interfacial Electrochemistry. *Accts. Chem. Res.* **2007**, *40*, 1165-1173.

(4) Watanabe, M.; Thomas, M. L.; Zhang, S.; Ueno, K.; Yasuda, T.; Dokko, K., Application of Ionic Liquids to Energy Storage and Conversion Materials and Devices. *Chem. Rev.* **2017**, *117*, 7190-7239.

(5) MacFarlane, D. R.; Tachikawa, N.; Forsyth, M.; Pringle, J. M.; Howlett, P. C.; Elliott, G. D.; Davis, J. H.; Watanabe, M.; Simon, P.; Angell, C. A., Energy Applications of Ionic Liquids. *Energy Environ. Sci.* **2014**, *7*, 232-250.

(6) Liu, H.; Yu, H., Ionic Liquids for Electrochemical Energy Storage Devices Applications. *J. Mater. Sci. Technol.* **2018**, *35*, 674-686.

(7) Suresh; Sandhu, J. S., Recent Advances in Ionic Liquids: Green Unconventional Solvents of this Century: Part I. *Green Chem. Lett. Rev.* **2011**, *4*, 289-310.

(8) Newington, I.; Perez-Arlandis, J. M.; Welton, T., Ionic Liquids as Designer Solvents for Nucleophilic Aromatic Substitutions. *Org. Lett.* **2007**, *9*, 5247-5250.

(9) Baker, G. A.; Baker, S. N.; Pandey, S.; Bright, F. V., An Analytical View of Ionic Liquids. *Analyst* **2005**, *130*, 800-808.

(10) Sun, P.; Armstrong, D. W., Ionic Liquids in Analytical Chemistry. *Anal. Chem. Acta* **2010**, *661*, 1-16.

(11) Brown, L.; Earle, M. J.; Gîlea, M. A.; Plechkova, N. V.; Seddon, K. R., Ionic Liquid–Liquid Chromatography: A New General Purpose Separation Methodology. In *Ionic Liquids II*, Springer: 2017; pp 85-125.

(12) Soares, B.; Passos, H.; Freire, C. S.; Coutinho, J. A.; Silvestre, A. J.; Freire, M. G., Ionic Liquids in Chromatographic and Electrophoretic Techniques: Toward Additional Improvements in the Separation of Natural Compounds. *Green Chem.* **2016**, *18*, 4582-4604.

(13) Poole, C. F.; Lenca, N., Gas Chromatography on Wall-Coated Open-Tubular Columns with Ionic Liquid Stationary Phases. *J. Chromatogr. A* **2014**, *1357*, 87-109.

(14) Prince, B.; Fritz, B.; Chiu, Y., Ionic Liquids in Electrospray Propulsion Systems. *Ionic Liquids: Science and Applications* **2012**, *1117*, 27-49.

(15) Donius, B. R.; Rovey, J. L., Ionic Liquid Dual-Mode Spacecraft Propulsion Assessment. *J. Spacecraft Rockets* **2011**, *48*, 110-123.

(16) Berg, S. P.; Rovey, J. L., Assessment of Imidazole-Based Ionic Liquids as Dual-Mode Spacecraft Propellants. *J. Propul. Power.* **2013**, *29*, 339-351.

(17) Patrick, A. L., Electrospray Ionization Enters the Final Frontier: Mass Spectrometry's Role in Understanding Electrospray Thrusters and Their Plumes. *Rapid Commun. Mass Spectrom.* **2020**, *34*, e8587.

(18) Yamashita, M.; Fenn, J. B., Electrospray Ion Source. Another Variation on the Free-Jet Theme. *J. Phys. Chem.* **1984**, *88*, 4451-4459.

(19) Lozano, P.; Martinez-Sanchez, M., Ionic Liquid Ion Sources: Characterization of Externally Wetted Emitters. *J. Colloid Interface Sci.* **2005**, *282*, 415-421.

(20) Mehta, N. A.; Levin, D. A., Molecular Dynamics Electrospray Simulations of Coarse-Grained Ethylammonium Nitrate (EAN) and 1-Ethyl-3-Methylimidazolium Tetrafluoroborate (EMIM-BF_4). *Aerospace* **2018**, *5*, 1.

(21) Roy, H. A.; Hamlow, L. A.; Rodgers, M. T., Gas Phase Binding Energies and Dissociation Dynamics of 1-Alkyl-3-Methylimidazolium Tetrafluoroborate Ionic Liquid Clusters. *J. Phys. Chem. A* **2020**, *submitted for publication*, jp-2020-06297y.

(22) Armentrout, P. B.; Rodgers, M. T., An Absolute Sodium Cation Affinity Scale: Threshold Collision-Induced Dissociation Experiments and ab Initio Theory. *J. Phys. Chem. A* **2000**, *104*, 2238-2247.

(23) *CRC Handbook of Chemistry and Physics*. 101st ed.; CRC Press, Taylor & Francis: Boca Raton, FL, 2020.

(24) Linstrom, P. J.; Mallard, W. G., *NIST Chemistry WebBook, NIST Standard Reference Database Number 69*. National Institute of Standards and Technology: Gaithersburg MD, 20899, 2018; Vol. (http://webbook.nist.gov).

(25) Fernandes, A. M.; Coutinho, J. A.; Marrucho, I. M., Gas‐Phase Dissociation of Ionic Liquid Aggregates Studied by Electrospray Ionisation Mass Spectrometry and Energy‐Variable Collision Induced Dissociation. *J. Mass Spectrom.* **2009**, *44*, 144-150.

(26) Bini, R.; Bortolini, O.; Chiappe, C.; Pieraccini, D.; Siciliano, T., Development of Cation/Anion "Interaction" Scales for Ionic Liquids Through ESI-MS Measurements. *J. Phys. Chem. B* **2007**, *111*, 598-604.

(27) Gozzo, F. C.; Santos, L. S.; Augusti, R.; Consorti, C. S.; Dupont, J.; Eberlin, M. N., Gaseous Supramolecules of Imidazolium Ionic Liquids: "Magic" Numbers and Intrinsic Strengths of Hydrogen Bonds. *Chem. Eur. J.* **2004**, *10*, 6187-6193.

(28) Vitorino, J.; Leal, J. P.; Minas da Piedade, M. E., Gas-Phase Affinity Scales for Typical Ionic Liquid Moieties Determined by using Cooks' Kinetic Method. *ChemPhysChem* **2015**, *16*, 1969-1977.

(29) Fernandes, A. M.; Rocha, M. A.; Freire, M. G.; Marrucho, I. M.; Coutinho, J. A.; Santos, L. M., Evaluation of Cation−Anion Interaction Strength in Ionic Liquids. *J. Phys. Chem. B* **2011**, *115*, 4033-4041.

(30) Zhou, Y.; Zhan, J.; Gao, X.; Li, C.; Chingin, K.; Le, Z., The Cation−Anion Interaction in Ionic Liquids Studied by Extractive Electrospray Ionization Mass Spectrometry. *Can. J. Chem.* **2014**, *92*, 611-615.

(31) Bortolini, O.; Chiappe, C.; Ghilardi, T.; Massi, A.; Pomelli, C. S., Dissolution of Metal Salts in Bis(trifluoromethylsulfonyl)imide-Based Ionic Liquids: Studying the Affinity of Metal Cations Toward a "Weakly Coordinating" Anion. *J. Phys. Chem. A* **2015**, *119*, 5078-5087.

(32) De Silva, M.; Brown, A. C.; Patrick, A. L., Thermal- and Collision-Induced Dissociation Studies of Functionalized Imidazolium-Based Ionic Liquid Cations. *J. Mass Spectrom.* **2020**, *55*, e4518.

(33) Rodgers, M. T., Substituent Effects in the Binding of Alkali Metal Ions to Pyridines Studied by Threshold Collision-Induced Dissociation and Ab Initio Theory: The Methylpyridines. *J. Phys. Chem. A* **2001**, *105*, 2374-2383.

(34) Chen, Y.; Rodgers, M. T., Structural and Energetic Effects in the Molecular Recognition of Protonated Peptidomimetic Bases by 18-Crown-6. *J. Am. Chem. Soc.* **2012**, *134*, 2313-2324.

(35) Moision, R.; Armentrout, P., An Electrospray Ionization Source for Thermochemical Investigation with the Guided Ion Beam Mass Spectrometer. *J. Am. Soc. Mass Spectrom.* **2007**, *18*, 1124–1134.

(36) Dalleska, N. F.; Honma, K.; Armentrout, P. B., Stepwise Solvation Enthalpies of Protonated Water Clusters: Collision-Induced Dissociation as an Alternative to Equilibrium Studies. *J. Am. Chem. Soc.* **1993**, *115*, 12125-12131.

(37) Aristov, N.; Armentrout, P. B., Collision Induced-Dissociation of Vanadium Monoxide Ion. *J. Phys. Chem.* **1986**, *90*, 5135-5140.

(38) Hales, D. A.; Armentrout, P. B., Effect of Internal Excitation on the Collision-Induced Dissociation and Reactivity of Co_2^+. *J. Clust. Sci.* **1990**, *1*, 127-142.

(39) Daly, N. R., Scintillation Type Mass Spectrometer Ion Detector. *Rev. Sci. Instrum.* **1960**, *31*, 264-267.

(40) Bertsimas, D.; Tsitsiklis, J., Simulated Annealing. *Stat. Sci.* **1993**, *8*, 10-15.

(41) Wolinski, K.; Hinton, J.; Wishart, D.; Sykes, B.; Richards, F.; Pastone, A.; Saudek, V.; Ellis, P.; Maciel, G.; McIver, J., HyperChem Computational Chemistry Software Package, Version 8.0. Hypercube, Inc., Gainsville, FL: 2004.

(42) Frisch, M. J.; Trucks, G. W.; Schlegel, H. B.; Scuseria, G. E.; Robb, M. A.; Cheeseman, J. R.; Scalmani, G.; Barone, V.; Mennucci, B.; Petersson, G. A., et al., *Gaussian 09*, revision C.01; Gaussian, Inc.: Wallingford, CT, 2009.

(43) Becke, A. D., Density-Functional Thermochemistry. III. The Role of Exact Exchange. *J. Chem. Phys.* **1993**, *98*, 5648-5652.

(44) Lee, C.; Yang, W.; Parr, R. G., Development of the Colle-Salvetti Correlation-energy Formula into a Functional of the Electron Density. *Phys. Rev. B* **1988**, *37*, 785-789.

(45) Sousa, S. F.; Fernandes, P. A.; Ramos, M. J., General Performance of Density Functionals. *J. Phys. Chem. A* **2007**, *111*, 10439-10452.

(46) Tirado-Rives, J.; Jorgensen, W. L., Performance of B3LYP Density Functional Methods for a Large Set of Organic Molecules. *J. Chem. Theory Comput.* **2008**, *4*, 297-306.

(47) Grimme, S.; Ehrlich, S.; Goerigk, L., Effect of the Damping Function in Dispersion Corrected Density Functional Theory. *J. Comput. Chem.* **2011**, *32*, 1456-1465.

(48) Zhao, Y.; Truhlar, D. G., The M06 Suite of Density Functionals for Main Group Thermochemistry, Thermochemical Kinetics, Noncovalent Interactions, Excited States, and Transition Elements: Two New Functionals and Systematic Testing of Four M06-Class Functionals and 12 Other Functionals. *Theor. Chem. Acc.* **2008**, *120*, 215-241.

(49) Simon, S.; Duran, M.; Dannenberg, J., How Does Basis Set Superposition Error Change the Potential Surfaces for Hydrogen‐Bonded Dimers? *J. Chem. Phys.* **1996**, *105*, 11024-11031.

(50) Boys, S. F.; Bernardi, R., The Calculation of Small Molecular Interactions by the Differences of Separate Total Energies. Some Procedures with Reduced Errors. *Mol. Phys.* **1970**, *19*, 553-566.

(51) Contreras-García, J.; Johnson, E. R.; Keinan, S.; Chaudret, R.; Piquemal, J.-P.; Beratan, D. N.; Yang, W., NCIPLOT: A Program for Plotting Noncovalent Interaction Regions. *J. Chem. Theory Comput.* **2011**, *7*, 625-632.

(52) Johnson, E. R.; Keinan, S.; Mori-Sánchez, P.; Contreras-García, J.; Cohen, A. J.; Yang, W., Revealing Noncovalent Interactions. *J. Am. Chem. Soc.* **2010**, *132*, 6498-6506.

(53) Humphrey, W.; Dalke, A.; Schulten, K., VMD: Visual Molecular Dynamics. *J. Mol. Graph.* **1996**, *14*, 33-38.

(54) Ervin, K. M.; Armentrout, P. B., Translational Energy Dependence of $Ar^+ + XY \rightarrow ArX^+ + Y$ ($XY = H_2$, D_2, HD) from Thermal to 30 eV c.m. *J. Chem. Phys.* **1985**, *83*, 166-189.

(55) Rodgers, M. T.; Ervin, K. M.; Armentrout, P. B., Statistical Modeling of Collision-Induced Dissociation Thresholds. *J. Chem. Phys.* **1997**, *106*, 4499-4508.

(56) Rodgers, M. T.; Armentrout, P. B., Statistical Modeling of Competitive Threshold Collision-Induced Dissociation. *J. Chem. Phys.* **1998**, *109*, 1787-1800.

(57) Beyer, T. S.; Swinehart, D. F., Number of Multiply-Restricted Partitions. *Commun. ACM* **1973**, *16*, 379.

(58) Merrick, J. P.; Moran, D.; Radom, L., An Evaluation of Harmonic Vibrational Frequency Scale Factors. *J. Phys. Chem. A* **2007**, *111*, 11683–11700.

(59) Khan, F. A.; Clemmer, D. E.; Schultz, R. H.; Armentrout, P. B., Sequential Bond Energies of $Cr(CO)_x^+$, $x = 1 - 6$. *J. Phys. Chem.* **1993**, *97*, 7978-7987.

(60) Muntean, F.; Armentrout, P., Modeling Kinetic Shifts and Competition in Threshold Collision-Induced Dissociation. Case Study: n-Butylbenzene Cation Dissociation. *J. Phys. Chem. A* **2003**, *107*, 7413-7422.

(61) Muntean, F.; Armentrout, P., Collision-Induced Dissociation Dynamics of the $[OCS•C_2H_2]^+$ Complex. A Combined Experimental and Theoretical Study. *Z. Phys. Chem.* **2000**, *214*, 1035-1064.

(62) Amicangelo, J. C.; Armentrout, P. B., Relative and Absolute Bond Dissociation Energies of Sodium Cation Complexes Determined Using Competitive Collision-Induced Dissociation Experiments. *Int. J. Mass Spectrom.* **2001**, *212*, 301-325.

(63) Romanov, V.; Siu, C.-K.; Verkerk, U. H.; Hopkinson, A. C.; Siu, K. M., Bond Dissociation Energies of Solvated Silver (I)−Amide Complexes: Competitive Threshold Collision-Induced Dissociations and Calculations. *J. Phys. Chem. A* **2010**, *114*, 6964-6971.

(64) Chen, Y.; Rodgers, M., Re-Evaluation of the Proton Affinity of 18-Crown-6 Using Competitive Threshold Collision-Induced Dissociation Techniques. *Anal. Chem.* **2012**, *84*, 7570-7577.

(65) Chen, Y.; Rodgers, M. T., Structural and Energetic Effects in the Molecular Recognition of Amino Acids by 18-Crown-6 *J. Am. Chem. Soc.* **2012**, *134*, 5863-5875.

(66) Rannulu, N. S.; Rodgers, M. T., Noncovalent Interactions of Cu^+ with N-Donor Ligands (Pyridine, 4,4-Dipyridyl, 2,2-Dipyridyl, and 1,10-Phenanthroline): Collision-Induced Dissociation and Theoretical Studies. *J. Phys. Chem. A* **2007**, *111*, 3465-3479.

(67) Hallowita, N.; Carl, D. R.; Armentrout, P. B.; Rodgers, M. T., Dipole Effects on Cation-π Interactions: Absolute Bond Dissociation Energies of Complexes of Alkali Metal Cations to N-methylaniline and N,N-dimethylaniline. *J. Phys. Chem. A* **2008**, *112*, 7996–8008.

(68) Ruan, C.; Yang, Z.; Rodgers, M., Influence of the d Orbital Occupation on the Nature and Strength of Copper Cation–π Interactions: Threshold Collision-Induced Dissociation and Theoretical Studies. *Phys. Chem. Chem. Phys.* **2007**, *9*, 5902-5918.

(69) Rannulu, N. S.; Amunugama, R.; Yang, Z.; Rodgers, M. T., Influence of s and d Orbital Occupation on the Binding of Metal Ions to Imidazole. *J. Phys. Chem. A* **2004**, *108*, 6385-6396.

(70) Ruan, C.; Rodgers, M. T., Cation-π Interactions: Structures and Energetics of Complexation of Na^+ and K^+ with the Aromatic Amino Acids, Phenylalanine, Tyrosine and Tryptophan. *J. Am. Chem. Soc.* **2004**, *126*, 14600-14610.

(71) Huang, H.; Rodgers, M. T., Sigma versus Pi Interactions in Alkali Metal Ion Binding Affinities of Azoles: Threshold Collision-Induced Dissociation and Ab Initio Theory Studies. *J. Phys. Chem. A* **2002**, *106*, 4277-4289.

(72) Rodgers, M. T.; Armentrout, P. B., Absolute Alkali Metal Ion Binding Affinities of Several Azoles Determined by Threshold Collision-Induced Dissociation. *Int. J. Mass Spectrom.* **1999**, *185/186/187*, 359-380.

(73) Ruan, C.; Yang, Z.; Hallowita, N.; Rodgers, M. T., Cation-π Interactions with a Model for the Side Chain of Tryptophan: Structures and Absolute Binding Energies of Alkali Metal Cation-Indole Complexes. *J. Phys. Chem. A* **2005**, *109*, 11539-11550.

Table 1. Fitting Parameters of eq 6, Threshold Dissociation Energies at 0 K and Entropies of Activation at 1000 K of $[C_{n-2}mim{:}BF_4{:}C_nmim]^+$ Clusters.[a]

System	Ionic Product	σ[b]	*n*	E_0[c] (eV)	E_0(PSL)[b] (eV)	Kinetic Shift (eV)	$\Delta S^{\ddagger}$ (PSL)[b] (J mol^{-1} K^{-1})
$[C_2mim{:}BF_4{:}C_4mim]^+$	$[C_2mim]^+$	240.7 (6.1)	1.0 (0.1)	2.17 (0.03)	1.29 (0.05)	0.88	25 (5)
	$[C_4mim]^+$	80.8 (2.9)	1.0 (0.1)	2.02 (0.02)	1.24 (0.05)	0.78	31 (5)
$[C_4mim{:}BF_4{:}C_6mim]^+$	$[C_4mim]^+$	42.8 (0.8)	1.2 (0.1)	2.39 (0.11)	1.25 (0.06)	1.14	25 (3)
	$[C_6mim]^+$	42.8 (0.8)	1.2 (0.1)	2.32 (0.11)	1.20 (0.06)	1.11	17 (4)
$[C_6mim{:}BF_4{:}C_8mim]^+$	$[C_6mim]^+$	45.4 (3.6)	1.2 (0.1)	2.75 (0.08)	1.33 (0.06)	1.42	44 (4)
	$[C_8mim]^+$	45.4 (3.6)	1.2 (0.1)	2.64 (0.08)	1.29 (0.06)	1.42	38 (4)

[a]Present results based on competitive analyses of the CID product cross sections of **reactions 7** and **8** except as noted. Uncertainties are listed in parentheses. [b]Average values for loose a PSL TS. [c]Results based on analyses of the CID product cross sections using **eq 4**, without inclusion of lifetime or competitive effects.

Table 2. Absolute Bond Dissociation Energies for $[C_{n-2}mim{:}BF_4{:}C_nmim]^+$ at 0 K in kJ/mol.[a]

System	Ionic Product	TCID	B3LYP[b]		M06-2X[d]		GD3BJ[c]	
			D_0	$D_{0,BSSE}$[e]	D_0	$D_{0,BSSE}$[e]	D_0	$D_{0,BSSE}$[e]
$[C_2mim{:}BF_4{:}C_4mim]^+$	$[C_2mim]^+$	124.4 (4.7)	127.8	123.7	117.7[f]	112.3[f]	124.5	120.2
	$[C_4mim]^+$	119.4 (4.6)	122.7	118.5	113.8[f]	108.3[f]	124.8	120.2
$[C_4mim{:}BF_4{:}C_6mim]^+$	$[C_4mim]^+$	120.3 (5.5)	123.8	119.6	126.0[f]	117.8[f]	121.5	113.8
	$[C_6mim]^+$	116.1 (5.4)	124.5	120.3	124.3[f]	117.5[f]	120.6	115.9
$[C_6mim{:}BF_4{:}C_8mim]^+$	$[C_6mim]^+$	128.4 (6.3)	124.3	120.1	128.5	117.9	139.3	131.7
	$[C_8mim]^+$	124.4 (6.2)	122.5	118.2	136.8	126.4	136.4	128.7
AEU/MAD[g]		5.5 (0.7)[h]	4.1 (2.2)	3.5 (3.3)	6.5 (4.0)	6.6 (5.1)	5.7 (4.9)	3.2 (2.4)

[a]Present results, uncertainties are listed in parentheses. [b]Calculated at the B3LYP level of theory including ZPE corrections. [c]Calculated at the B3LYP-GD3BJ level of theory including ZPE corrections. [d]Calculated at the M06-2X level of theory including ZPE corrections. [e]Also includes BSSE corrections. [f]Calculated using grid=ultrafine keyword to facilitate convergence. [g]Mean absolute deviation (MADs) between TCID and calculated values. [h]Average experimental uncertainty (AEU).

Table 3. Enthalpies and Free Energies of Binding of the $[C_{n-2}mim:BF_4:C_nmim]^+$ Clusters at 298 K in kJ/mol[a]

System	Ionic Product	ΔH_0	ΔH_0[b]	$\Delta H_{298} - \Delta H_0$[b]	ΔH_{298}	ΔH_{298}[b]	$T\Delta S_{298}$[b]	ΔG_{298}	ΔG_{298}[b]
$[C_2mim:BF_4:C_4mim]^+$	$[C_2mim]^+$	124.4 (4.7)	123.7	-3.9 (0.1)	120.5 (4.7)	119.8	35.2 (1.5)	85.3 (4.9)	84.8
	$[C_4mim]^+$	119.4 (4.6)	118.5	-3.5 (0.1)	115.9 (4.6)	115.0	37.2 (1.5)	78.7 (4.8)	78.0
$[C_4mim:BF_4:C_6mim]^+$	$[C_4mim]^+$	120.3 (5.5)	119.6	-3.4 (0.1)	116.9 (5.5)	116.2	34.9 (1.5)	82.0 (5.7)	81.4
	$[C_6mim]^+$	116.1 (5.4)	120.3	-4.0 (0.1)	112.1 (5.4)	116.2	32.8 (1.5)	79.3 (5.6)	83.5
$[C_6mim:BF_4:C_8mim]^+$	$[C_6mim]^+$	128.4 (6.3)	120.1	-4.1 (0.1)	124.3 (6.3)	116.0	40.7 (1.5)	83.6 (6.5)	75.5
	$[C_8mim]^+$	124.4 (6.2)	118.2	-3.4 (0.1)	121.0 (6.2)	114.8	39.0 (1.5)	82.0 (6.4)	76.0

[a]Present results, uncertainties are listed in parentheses. [b]Values calculated at the B3LYP/6-311+G(2d,2p)/B3LYP/6-311+G(d,p) level of theory with frequencies scaled by 0.9887 and including BSSE corrections.

Table 4. Relative BDEs of $[C_{n-2}mim:BF_4:C_nmim]^+$ Clusters and Relative IPEs of $(C_{n-2}:BF_4)$ vs. $(C_nmim:BF_4)$ Ion Pairs at 0 K in kJ/mol.[a]

System	ΔIPE	B3LYP[b]		B3LYP-GD3BJ[c]		M06-2X[d]	
		D_0	$D_{0,BSSE}$[e]	D_0	$D_{0,BSSE}$[e]	D_0	$D_{0,BSSE}$[e]
$[C_2mim:BF_4:C_4mim]^+$	5.0 (1.4)	5.1	5.2	-0.3	0.0	3.9[f]	5.2[f]
		5.1	*5.3*	*-0.3*	*0.3*	*4.5*[f]	*5.4*[f]
$[C_4mim:BF_4:C_6mim]^+$	4.2 (1.2)	-0.7	-0.7	0.9	-2.1	1.7[f]	0.3[f]
		-0.6	*0.0*	*1.0*	*1.0*	*2.8*[f]	*2.6*[f]
$[C_6mim:BF_4:C_8mim]^+$	4.1 (1.1)	1.8	1.9	2.9	3.0	-8.4	-8.5
		1.8	*1.9*	*2.8*	*4.8*	*-8.4*	*-5.6*
AEU/MAD[g]	1.2 (0.2)[h]	2.4 (2.4)	2.4 (2.4)	3.3 (2.1)	4.1 (2.7)	5.3 (6.2)	5.8 (6.0)
		2.4 (2.4)	*2.4 (2.0)*	*3.3 (2.0)*	*3.3 (2.1)*	*4.8 (6.7)*	*3.9 (5.1)*

[a]Present results, uncertainties are listed in parentheses. [b]Calculated at the B3LYP level of theory including ZPE corrections. [c]Calculated at the B3LYP-GD3BJ level of theory including ZPE corrections. [d]Calculated at the M06-2X level of theory including ZPE corrections. [e]Also includes BSSE corrections. [f]Calculated using grid=ultrafine during optimization and frequency analysis. [g]Mean absolute deviation (MADs) between TCID measured and calculated values. [h]Average experimental uncertainty (AEU). [i]Values in standard font are computed from the energies of the $[C_{n-2}mim:BF_4:C_nmim]^+$ cluster and its CID products. Values in italics font are computed from differences in the energies of the $(C_{n-2}mim:BF_4)$ and $(C_nmim:BF_4)$ ion pairs and their component ions.

Table 5. Computed Ion-Pairing Energies of the ($C_n$mim:BF_4) Ion Pairs at 0 K in kJ/mol. [a]

System	B3LYP[b]		B3LYP-GD3BJ[c]		M06-2X[d]	
	D_0	$D_{0,BSSE}$[e]	D_0	$D_{0,BSSE}$[e]	D_0	$D_{0,BSSE}$[e]
(C_2mim:BF_4)	347.5	341.2	366.0	359.0	385.1	376.4
(C_4mim:BF_4)	342.4	335.9	366.3	358.7	380.6[f]	371.0[f]
(C_6mim:BF_4)	343.0	335.9	365.3	357.7	377.8	368.4
(C_8mim:BF_4)	341.2	334.0	362.5	352.9	386.2	374.0

[a]All values included ZPE corrections. [b]Calculated at the B3LYP/6-311+G(2d,2p) level of theory using B3LYP/6-311+G(d,p) optimized geometries. [c]Calculated at the B3LYP-GD3BJ/6-311+G(2d,2p) level of theory using B3LYP-GD3BJ/6-311+G(d,p) optimized geometries. [d]Calculated at the M06-2X/6-311+G(2d,2p) level of theory using M06-2X/6-311+G(d,p) optimized geometries. [e]Also includes BSSE corrections. [f]Calculated using grid=ultrafine for the integral keyword for the optimization and frequency analysis.

Table 6. Bond Dissociation Energies for the $[2C_n\text{mim:}BF_4]^+$ Clusters at 0 K in kJ/mol.[a]

System	TCID[b]	TCID[c] (Evaluated)	B3LYP[d]		B3LYP-GD3BJ[e]		M06-2X[f]	
			D_0	$D_{0,BSSE}$[g]	D_0	$D_{0,BSSE}$[g]	D_0	$D_{0,BSSE}$[g]
$[2C_2\text{mim:}BF_4]^+$	120.4 (4.2)	125.1 (2.6)	125.5	121.4	128.4	124.1	119.5	112.5
$[2C_4\text{mim:}BF_4]^+$	118.2 (5.0)	120.6 (2.6)	122.1	117.8	121.4	116.8	115.2[h]	108.8[h]
$[2C_6\text{mim:}BF_4]^+$	120.9 (6.0)	116.9 (2.7)	122.8	118.6	126.6	120.2	121.5	112.9
$[2C_8\text{mim:}BF_4]^+$	123.0 (6.3)	113.1 (2.8)	123.7	119.5	130.1	124.9	111.5	103.2
AEU/MAD[i]	5.4 (1.0)[j]	3.5 (0.1)[j]	2.9 (2.0) *4.6 (4.7)*	1.8 (1.4) *3.7 (2.0)*	6.0 (2.1) *7.7 (7.2)*	1.9 (1.3) *5.0 (4.7)*	4.0 (5.1) *4.3 (1.9)*	11.3 (5.7) *9.6 (3.9)*

[a]Present results, uncertainties are listed in parentheses. [b]Values taken from reference 2.1. [c]Values determined from regression analysis of the absolute and relative TCID 0 K BDEs. are indicated in italics. [d]Calculated at the B3LYP level of theory including ZPE corrections. [e]Calculated at the B3LYP-GD3BJ level of theory including ZPE corrections. [f]Calculated at the M06-2X level of theory including ZPE corrections. [g]Includes BSSE corrections. [h]Calculated using int=ultrafine keyword to facilitate convergence. [i]Mean absolute deviation (MADs) between TCID and calculated values. MADs based on the evaluated BDEs are indicated in italics. [j]Average experimental uncertainty (AEU).

FIGURE CAPTIONS

Figure 1. Chemical structures of the 1-alkyl-3-methylimidazolium cations, $[C_nmim]^+$ for n = 2, 4, 6 and 8, and the $[BF_4]^-$ anion. The atom numbering of the cations is indicated.

Figure 2. Cross sections for collision-induced dissociation of the $[C_{n-2}mim{:}BF_4{:}C_nmim]^+$ clusters (for n = 4, 6 and 8) with Xe as a function of collision energy in the center-of-mass frame (lower *x*-axis) and laboratory frame (upper *x*-axis). The two primary CID pathways leading to elimination of a neutral ion pair are labeled as $[C_nmim]^+$ with data shown as solid circles, where n = 2 (●), 4 (●), 6(●), and 8(●). Ionic products arising from sequential dissociation of the primary $[C_nmim]^+$ product ions are shown as open symbols ($[C_4H_7N_2]^+$ □, $[C_4H_9]^+$ △, and $[C_3H_7]^+$ ○) and color-coded to match the $[C_nmim]^+$ product ion from which they are primarily derived. The data shown was acquired at a Xe pressure of ~ 0.2 mTorr.

Figure 3. Overlay and expanded views of the CID cross sections of the $[C_{n-2}mim{:}BF_4{:}C_nmim]^+$ clusters, where n = 4, 6 and 8 as a function of the center-of-mass collision energy. The data shown were acquired at a Xe pressure of ~ 0.2 mTorr. The total CID cross sections (σ_{tot}) and the $[C_nmim]^+$ and $[C_{n-2}mim]^+$ primary CID product cross sections for each cluster are separately compared in the top, middle and bottom panels, respectively. A small systematic increase in the apparent thresholds with increasing size of the cluster cations is apparent in the data.

Figure 4. B3LYP/6-311+G(d,p) and M06-2X/6-311+G(d,p) optimized geometries of the ground conformers of the $[C_nmim]^+$ cations and $[BF_4]^-$ anion. The conformer designation describes the stereochemistry along the 1-alkyl substituent (see **Figure S1** for nomenclature details). Noncovalent interaction maps at an isosurface of 0.20 a.u. of the reduced electron density gradients determined using the same theoretical model with a 6-311+G(2d,2p) basis set have been superimposed on the optimized structures. Regions exhibiting highly repulsive interactions are color-coded in red, and occur above and below the center of the imidazolium ring. Weak attractive dispersion interactions are color-coded in green, and are visible only in the M06-2X structures along the 1-alkyl substituents, with the most significant interaction visible between the C3′ hydrogen atom and the π cloud of the 3-methylimidazolium ring, i.e., a cation-π interaction. Strong attractive interactions such as canonical hydrogen-bonding interactions are color-coded in blue; none are visible in these structures.

Figure 5. B3LYP/6-311+G(d,p) and M06-2X/6-311+G(d,p) optimized geometries of the ground conformers of the (C_nmim:BF_4) ion pairs. The conformer designation describes the binding site designation and stereochemistry along the 1-alkyl substituent (see **Figure S1** for details of the nomenclature used). Noncovalent interaction maps at an isosurface of 0.20 a.u. of the reduced electron density gradients determined using the same theoretical model and a 6-311+G(2d,2p) basis set have been superimposed on the optimized structures. The M06-2X NCI surfaces are more extensive than those of the B3LYP optimized structures. Regions exhibiting strongly repulsive interactions are color-coded in red, and occur above and below the center of the imidazolium ring. Weak attractive dispersion interactions are color-coded in green, and show the nature and extent of the noncovalent interaction between the $[C_nmim]^+$ cation and $[BF_4]^-$ anion. Strong attractive interactions such as canonical hydrogen-bonding interactions are color-coded in blue; none are visible in these structures.

Figure 6. B3LYP/6-311+G(d,p) and M06-2X/6-311+G(d,p) optimized geometries of the ground conformers of the $[C_nmim:BF_4:C_nmim]^+$ clusters. The conformer designation including the binding site designation(s) and 1-alkyl stereochemistry of the cations is given for each cluster (see **Figure S1** for nomenclature details). Noncovalent interaction maps at an isosurface of 0.20 a.u. of the reduced electron density gradients determined using the same theoretical model with a 6-311+G(2d,2p) basis set have been superimposed on the optimized structures. The M06-2X NCI surfaces are more extensive than those of the B3LYP optimized structures. Regions exhibiting strongly repulsive interactions are color-coded in red, and occur above and below the center of the imidazolium ring. Weak attractive dispersion interactions are color-coded in green, and show the nature and extent of the noncovalent interaction between the $[C_nmim]^+$ cations and $[BF_4]^-$ anion. Strong attractive interactions such as canonical hydrogen-bonding interactions are color-coded in blue; none are visible in these structures.

Figure 7. Zero-pressure-extrapolated cross sections for the collision-induced dissociation of the $[C_{n-2}mim:BF_4:C_nmim]^+$ clusters (for n = 4, 6, and 8) with Xe as a function of center-of-mass frame (lower *x*-axis) and laboratory frame (upper *x*-axis). The solid lines represent the best fits to the experimental data convoluted over the neutral and ion kinetic energy distributions. The dashed lines represents the model cross sections in the absence of experimental kinetic energy broadening for reactants with an internal energy corresponding to 0 K.

Figure 8. Comparisons of B3LYP, B3LYP-GD3BJ, and M06-2X computed 0 K BDEs versus measured threshold dissociation energies of the $[C_{n-2}mim:BF_4:C_nmim]^+$ clusters for n = 4, 6, and 8 (in kJ/mol). All theoretical values included ZPE and BSSE corrections. The $[C_nmim]^+$ and $[C_{n-2}mim]^+$ primary product cations are indicated with closed and open symbols, respectively. The n-2:n values of each cluster are indicated for each data point. The diagonal lines indicate values for which the calculated and measured values are equal.

Figure 9. Comparisons of B3LYP, B3LYP-GD3BJ, and M06-2X computed relative BDEs of the $[C_{n-2}mim:BF_4:C_nmim]^+$ clusters (for n = 4, 6 and 8) and relative IPEs of the ($C_nmim:BF_4$) ion pairs (for n = 2, 4, 6, 8) vs. experimentally determined 0 K ΔBDEs of the $[C_{n-2}mim:BF_4:C_nmim]^+$ clusters (for n = 4, 6 and 8). All theoretical values included ZPE and BSSE corrections. The ΔIPEs and ΔBDEs are indicated with open and closed symbols, respectively. The n-2:n values of each cluster are indicated for each data point. The diagonal lines indicate values for which the calculated and measured values are equal.

Figure 10. Absolute BDEs of the $[2C_nmim:BF_4]^+$ clusters at 0 K (in kJ/mol) as a function of the $[C_nmim]^+$ cation (n = 2, 4, 6, and 8) determined from independent TCID measurements (top panel). Relative BDEs of the $[C_{n-2}mim:BF_4:C_nmim]^+$ clusters at 0 K (in kJ/mol) as a function of the $[C_{n-2}mim]^+$ and $[C_nmim]^+$ cations (n = 4, 6, and 8) determined from competitive TCID measurements (middle panel). Absolute BDEs of the $[2C_nmim:BF_4]^+$ clusters at 0 K (in kJ/mol) as a function of the $[C_nmim]^+$ cation (n = 2, 4, 6, and 8) determined directly and evaluated from combined results of the independent and competitive TCID measurements (bottom panel).

Figure 11. Comparisons of B3LYP, B3LYP-GD3BJ, and M06-2X computed vs. TCID 0 K BDEs of the $[2C_nmim:BF_4]^+$ clusters for n = 2, 4, 6, and 8 (in kJ/mol). All theoretical values included ZPE and BSSE corrections. Values derived from direct TCID measurements[21] and those determined from regression analyses using the direct and competitive TCID measurements are indicated with open and closed symbols, respectively. The diagonal lines indicate values for which the calculated and measured values are equal.

Figure 1.

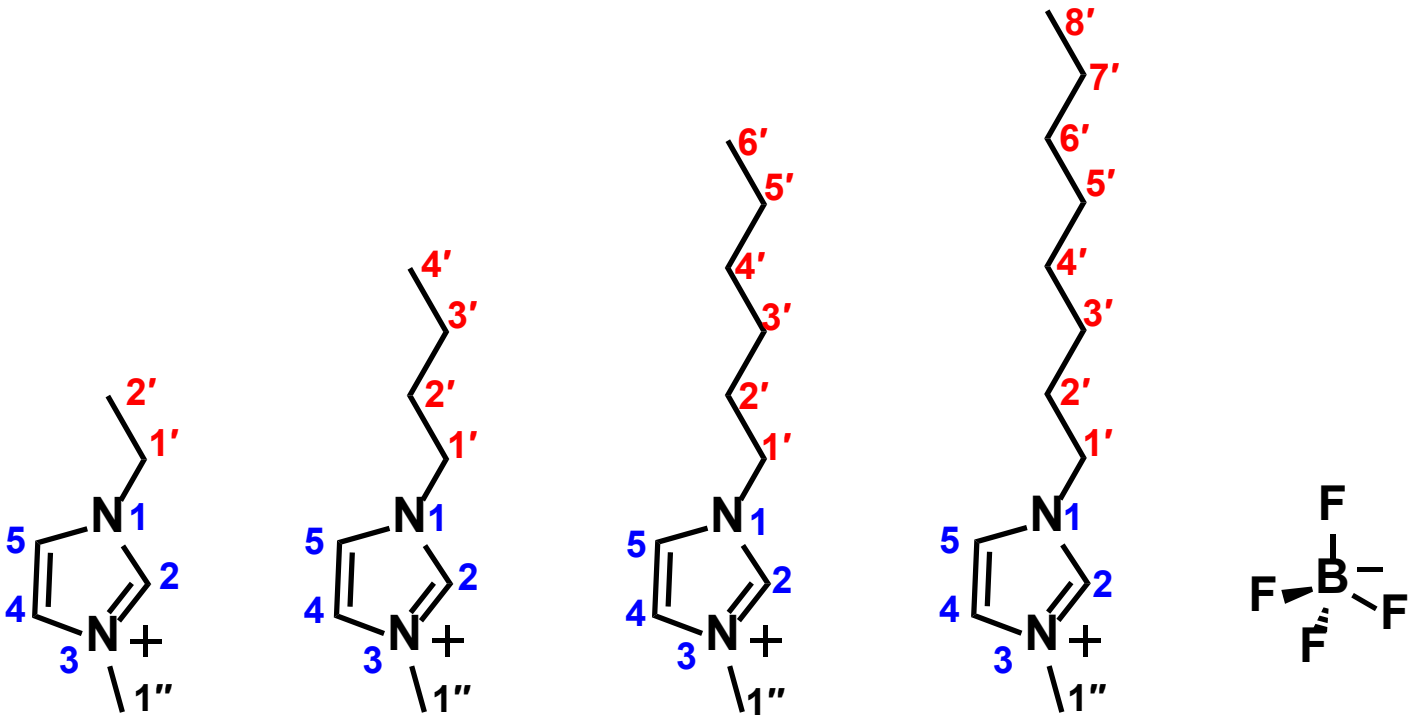

$[C_2mim]^+$ $[C_4mim]^+$ $[C_6mim]^+$ $[C_8mim]^+$ $[BF_4]^-$

Figure 2.

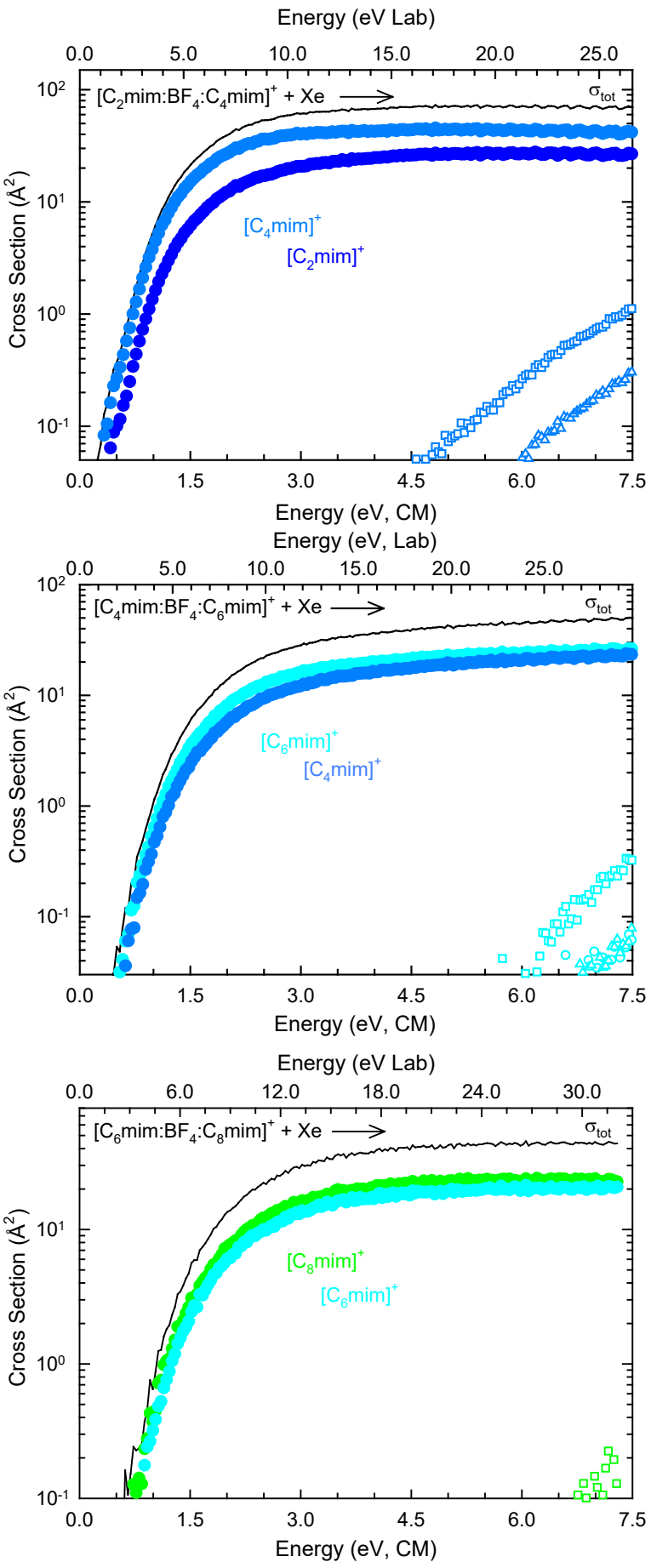
Energy (eV Lab)
[C2mim:BF4:C4mim]+ + Xe
σtot
[C4mim]+
[C2mim]+
Cross Section (Å2)
Energy (eV, CM)
Energy (eV, Lab)
[C4mim:BF4:C6mim]+ + Xe
σtot
[C6mim]+
[C4mim]+
Cross Section (Å2)
Energy (eV, CM)
Energy (eV Lab)
[C6mim:BF4:C8mim]+ + Xe
σtot
[C8mim]+
[C6mim]+
Cross Section (Å2)
Energy (eV, CM)

Figure 3.

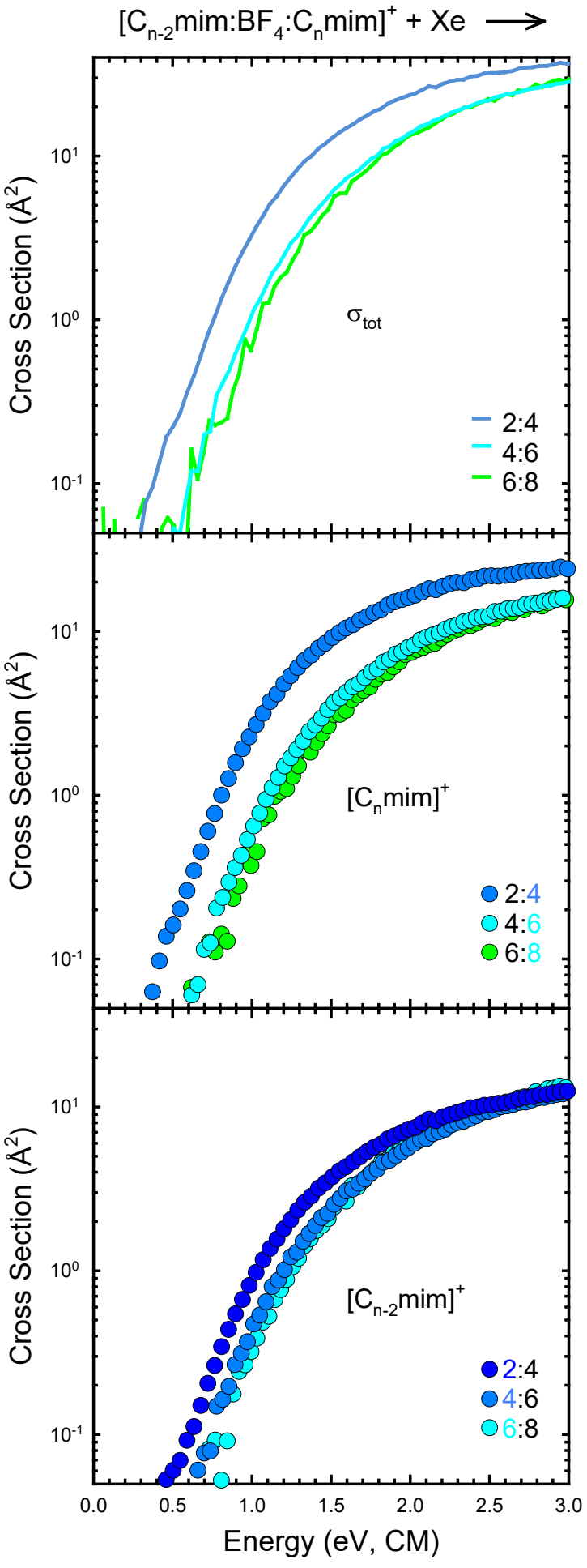
[C$_{n-2}$mim:BF$_4$:C$_n$mim]$^+$ + Xe ⟶
Cross Section (Å^2)
10^1
10^0
10^{-1}
σ_{tot}
2:4
4:6
6:8
[C$_n$mim]$^+$
2:4
4:6
6:8
[C$_{n-2}$mim]$^+$
2:4
4:6
6:8
0.0
0.5
1.0
1.5
2.0
2.5
3.0
Energy (eV, CM)

Figure 4.

B3LYP/6-311+G(d,p)

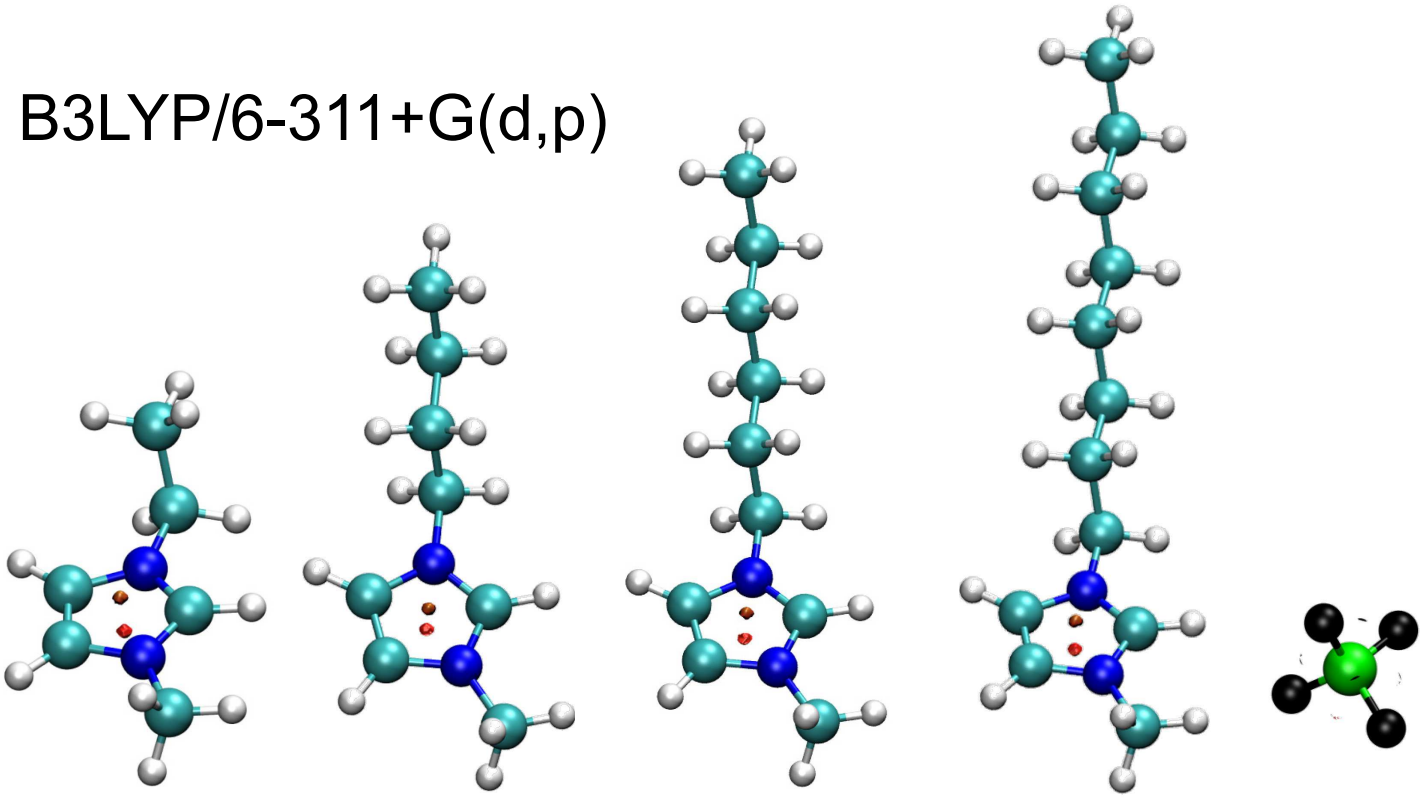

$[g_-]^+$ $[g_-t_2]^+$ $[g_-t_4]^+$ $[g_-t_6]^+$

$[C_2mim]^+$ $[C_4mim]^+$ $[C_6mim]^+$ $[C_8mim]^+$ $[BF_4]^-$

M06-2X/6-311+G(d,p)

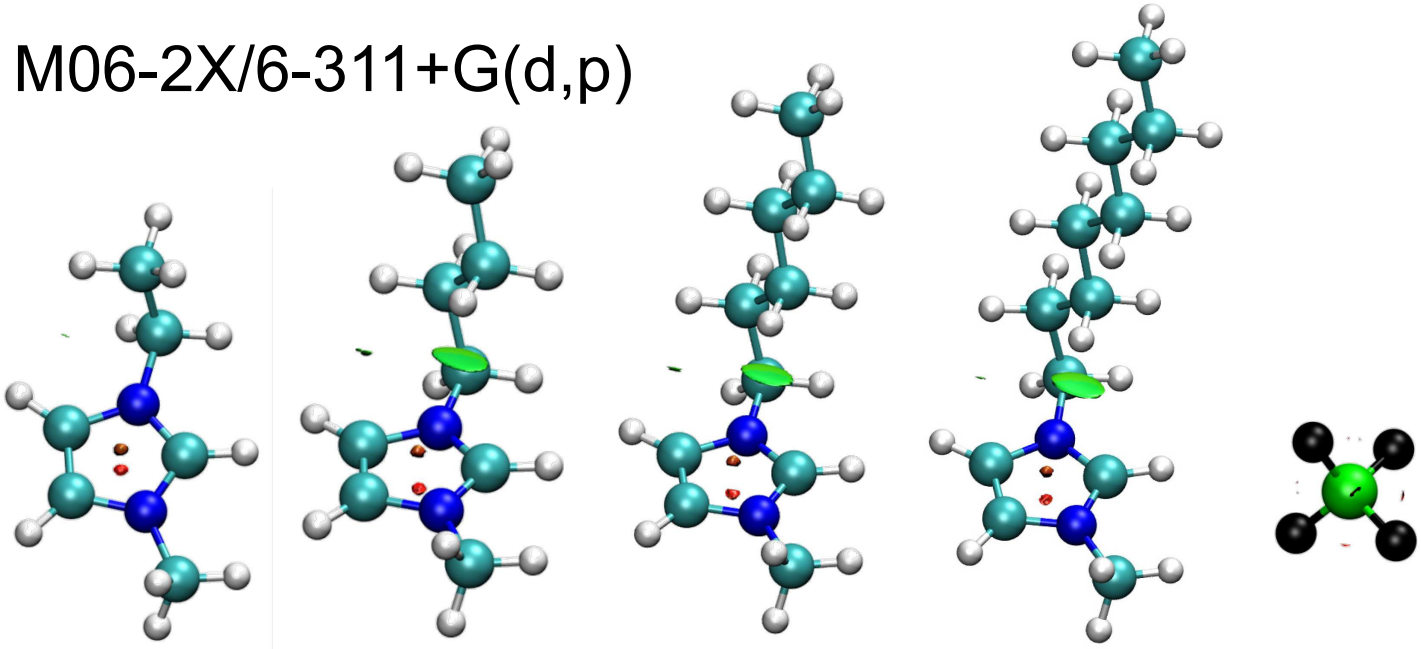

$[g_-]^+$ $[g_-g_+t]^+$ $[g_-g_+t_3]^+$ $[g_-g_+t_5]^+$

Figure 5.

B3LYP/6-311+G(d,p)

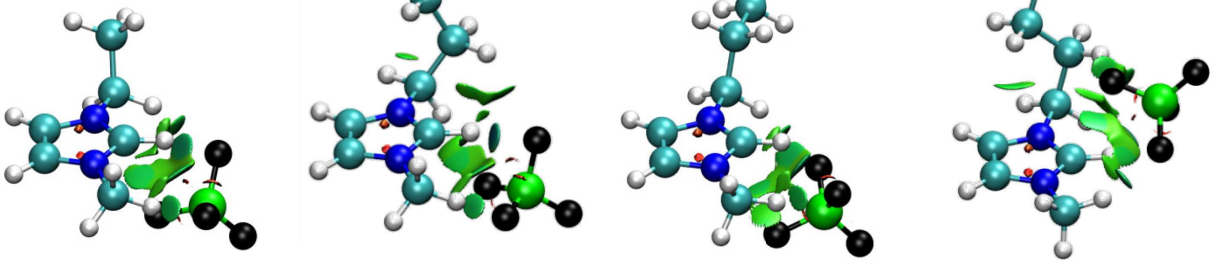

($\mathbf{g_+F}$;g_-) ($\mathbf{g_+F}$;$g_{-2}t$) ($\mathbf{cF}$;g_-t_4) ($\mathbf{cF}$;$g_{-2}t_5$)

(C_2mim:BF_4) (C_4mim:BF_4) (C_6mim:BF_4) (C_8mim:BF_4)

M06-2X /6-311+G(d,p)

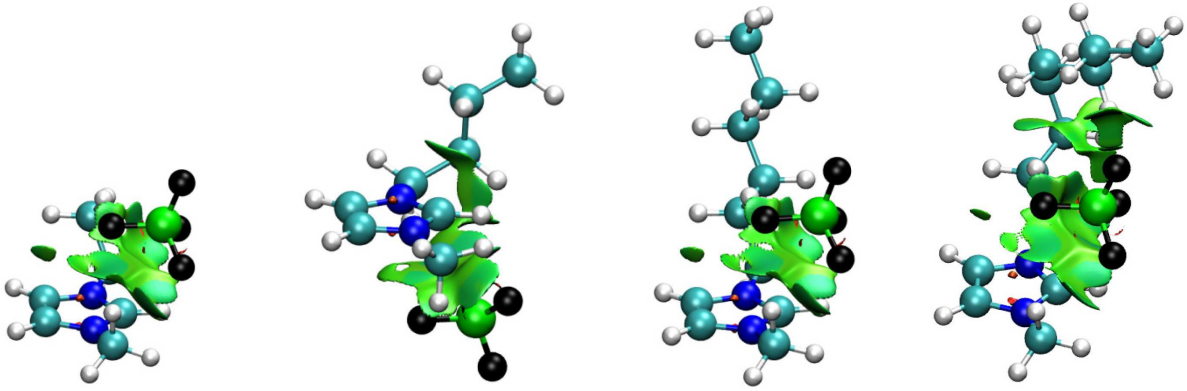

($\mathbf{g_-F}$;g_-) ($\mathbf{g_+F}$;cg_-t) ($\mathbf{g_-F}$;g_-t_4) ($\mathbf{g_-F}$;$g_-t_2g_{+2}t_2$)

Figure 6.

B3LYP/6-311+G(d,p)

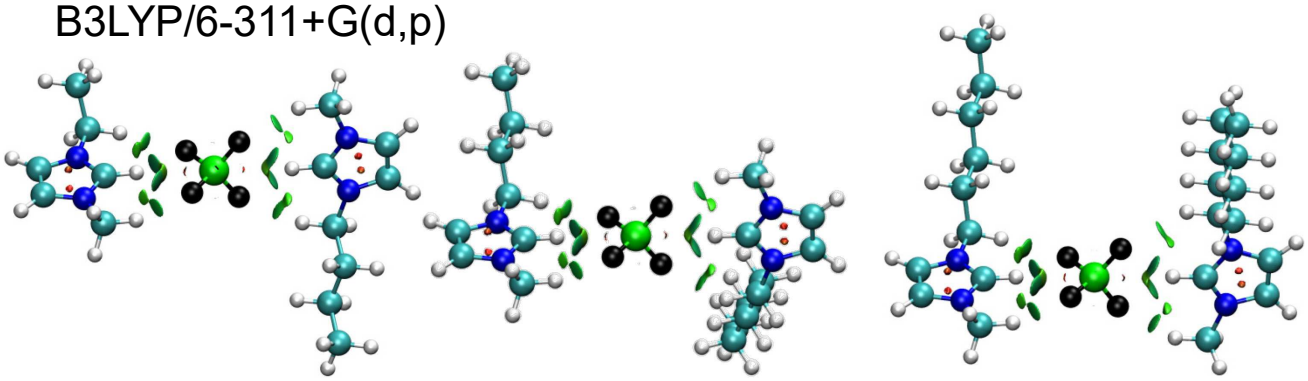

$[g_-;\mathbf{g_-cFcF};g_-t_2]^+$ $[g_-t_2;\mathbf{g_-cFcF};g_+t_4]^+$ $[g_-t_4;\mathbf{g_+cFcF};g_+t_6]^+$

$[C_2mim:BF_4:C_4mim]^+$ $[C_4mim:BF_4:C_6mim]^+$ $[C_6mim:BF_4:C_8mim]^+$

$[g_-;\mathbf{g_+g_-FcF};g_{+2}t]^+$ $[g_+g_{-2};\mathbf{tcF_mcF};g_-g_+t_3]^+$ $[g_+g_-t_2g_-;\ \mathbf{g_-cFcF}\ ;g_-g_{+2}t_2g_+t]^+$

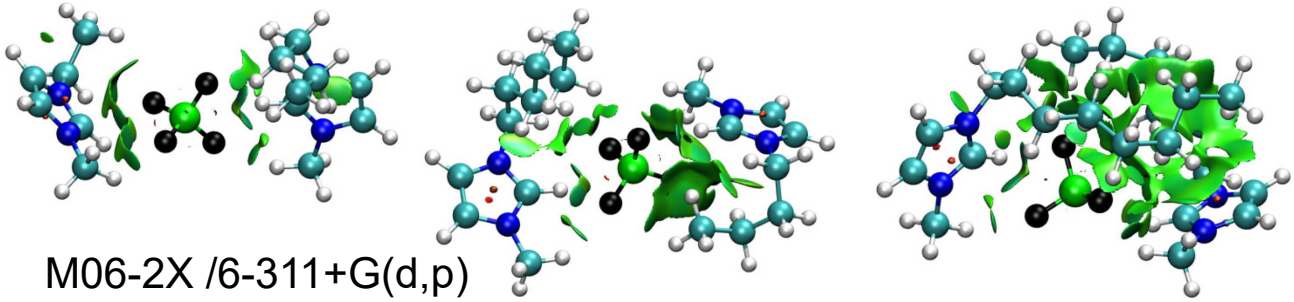

M06-2X /6-311+G(d,p)

Figure 7.

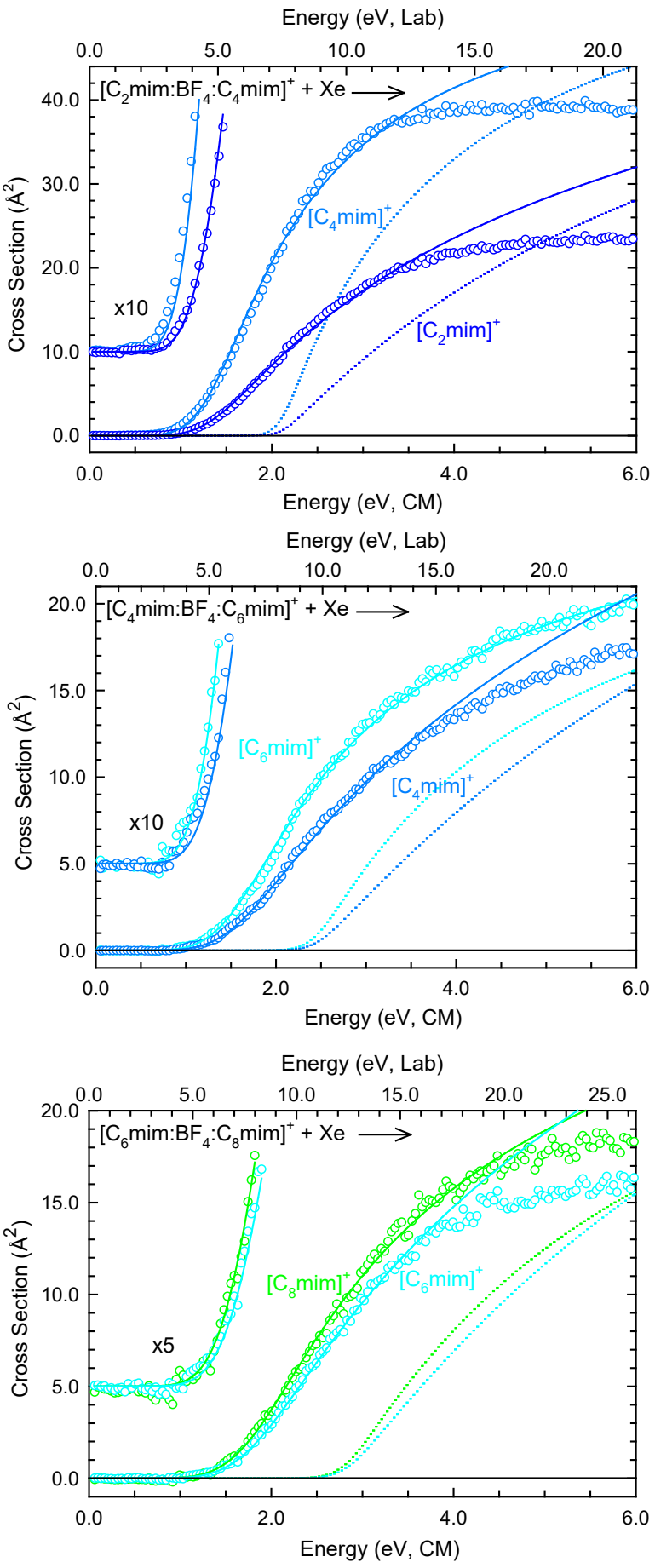
Energy (eV, Lab)
[C2mim:BF4:C4mim]+ + Xe
[C4mim]+
[C2mim]+
x10
Cross Section (Å2)
Energy (eV, CM)
[C4mim:BF4:C6mim]+ + Xe
[C6mim]+
[C4mim]+
x10
[C6mim:BF4:C8mim]+ + Xe
[C8mim]+
[C6mim]+
x5

Figure 8.

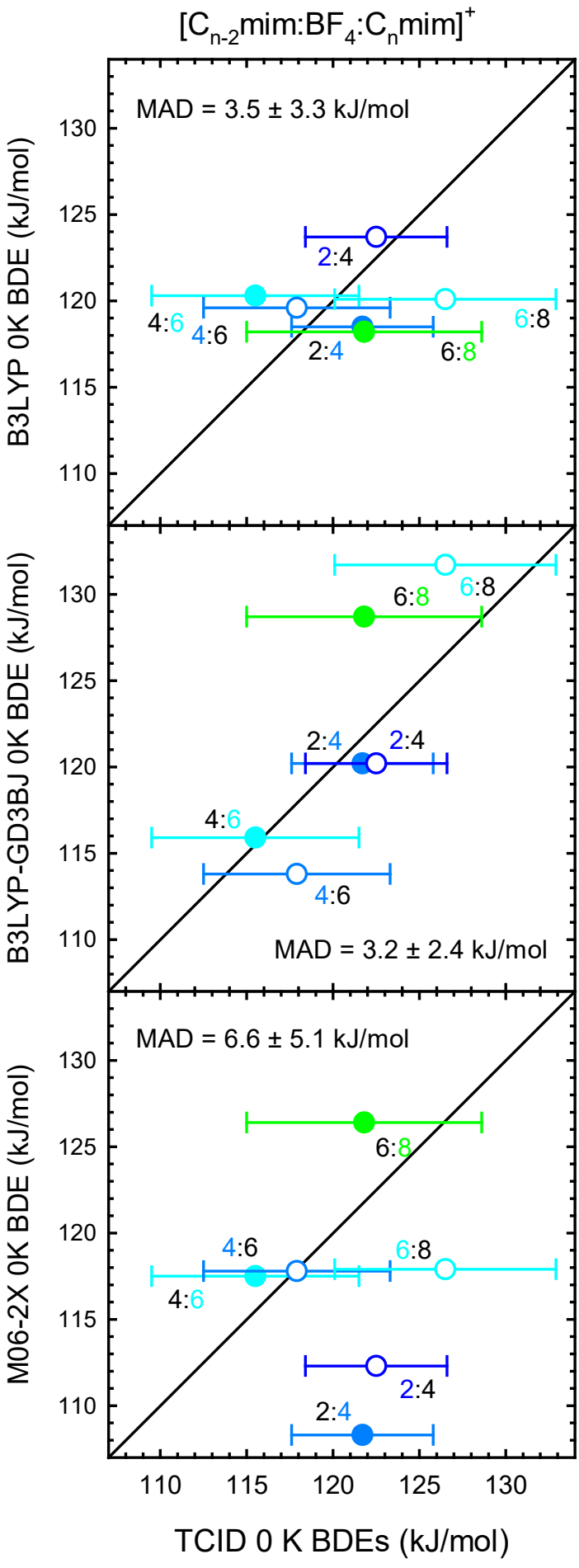
[C$_{n-2}$mim:BF$_4$:C$_n$mim]$^+$
MAD = 3.5 ± 3.3 kJ/mol
2:4
4:6
4:6
6:8
2:4
6:8
B3LYP 0K BDE (kJ/mol)
6:8
6:8
2:4
2:4
4:6
4:6
MAD = 3.2 ± 2.4 kJ/mol
B3LYP-GD3BJ 0K BDE (kJ/mol)
MAD = 6.6 ± 5.1 kJ/mol
6:8
4:6
6:8
4:6
2:4
2:4
M06-2X 0K BDE (kJ/mol)
110
115
120
125
130
TCID 0 K BDEs (kJ/mol)

Figure 9.

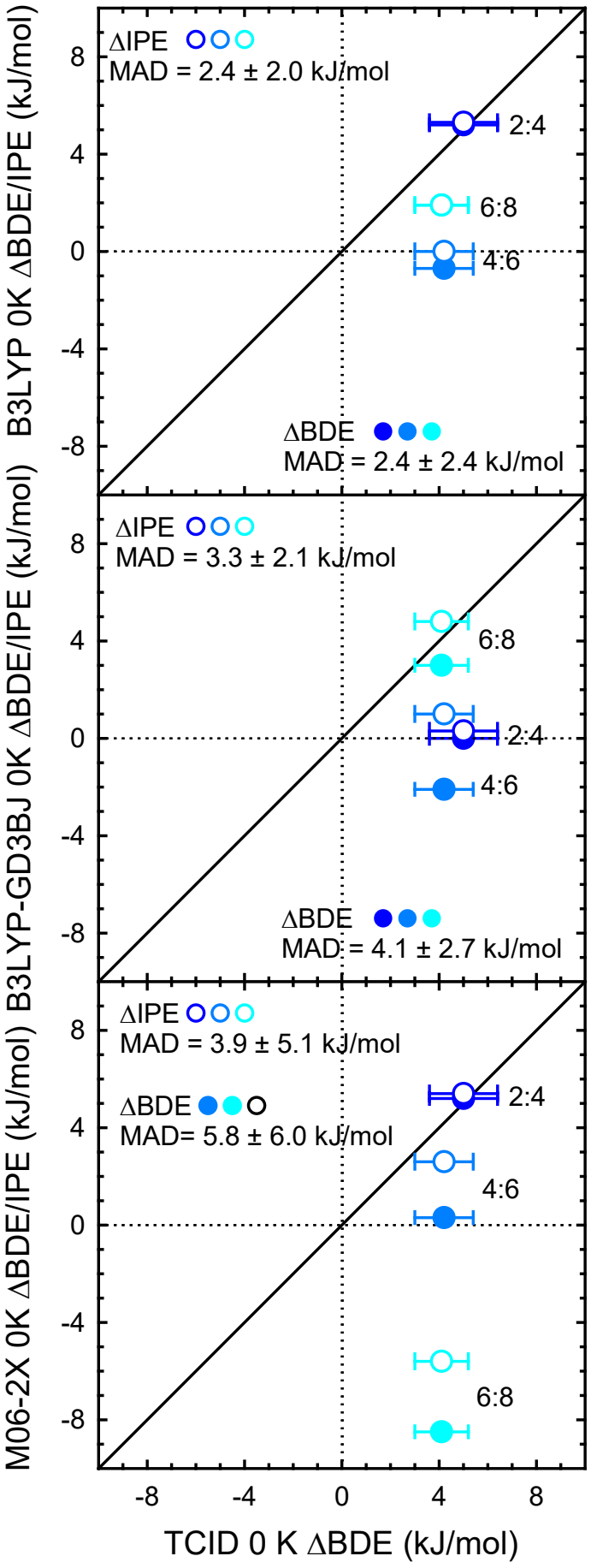
ΔIPE
MAD = 2.4 ± 2.0 kJ/mol
2:4
6:8
4:6
ΔBDE
MAD = 2.4 ± 2.4 kJ/mol
ΔIPE
MAD = 3.3 ± 2.1 kJ/mol
6:8
2:4
4:6
ΔBDE
MAD = 4.1 ± 2.7 kJ/mol
ΔIPE
MAD = 3.9 ± 5.1 kJ/mol
ΔBDE
MAD= 5.8 ± 6.0 kJ/mol
2:4
4:6
6:8
M06-2X 0K ΔBDE/IPE (kJ/mol) B3LYP-GD3BJ 0K ΔBDE/IPE (kJ/mol) B3LYP 0K ΔBDE/IPE (kJ/mol)
TCID 0 K ΔBDE (kJ/mol)
8
4
0
-4
-8

Figure 10.

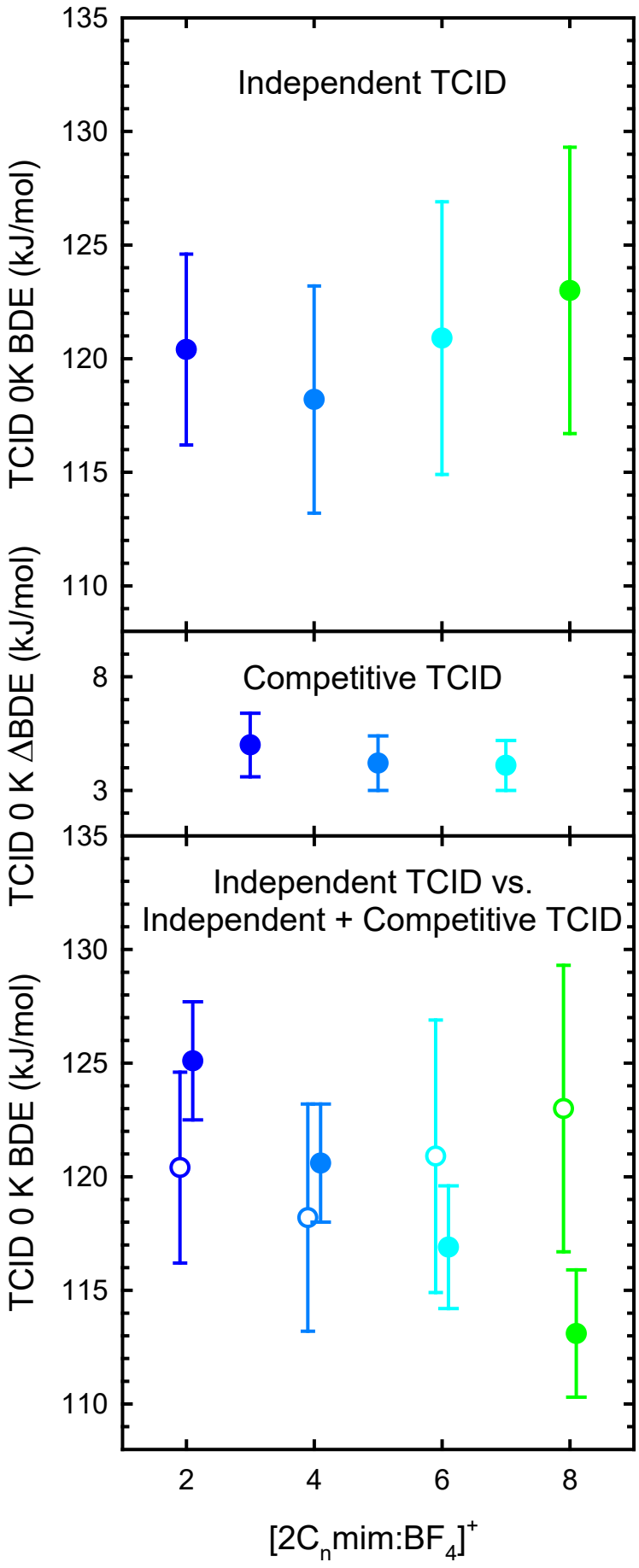
Independent TCID
Competitive TCID
Independent TCID vs.
Independent + Competitive TCID
TCID 0K BDE (kJ/mol)
TCID 0 K ΔBDE (kJ/mol)
TCID 0 K BDE (kJ/mol)
135
130
125
120
115
110
8
3
2
4
6
8
[2C$_n$mim:BF$_4$]$^+$

Figure 11.

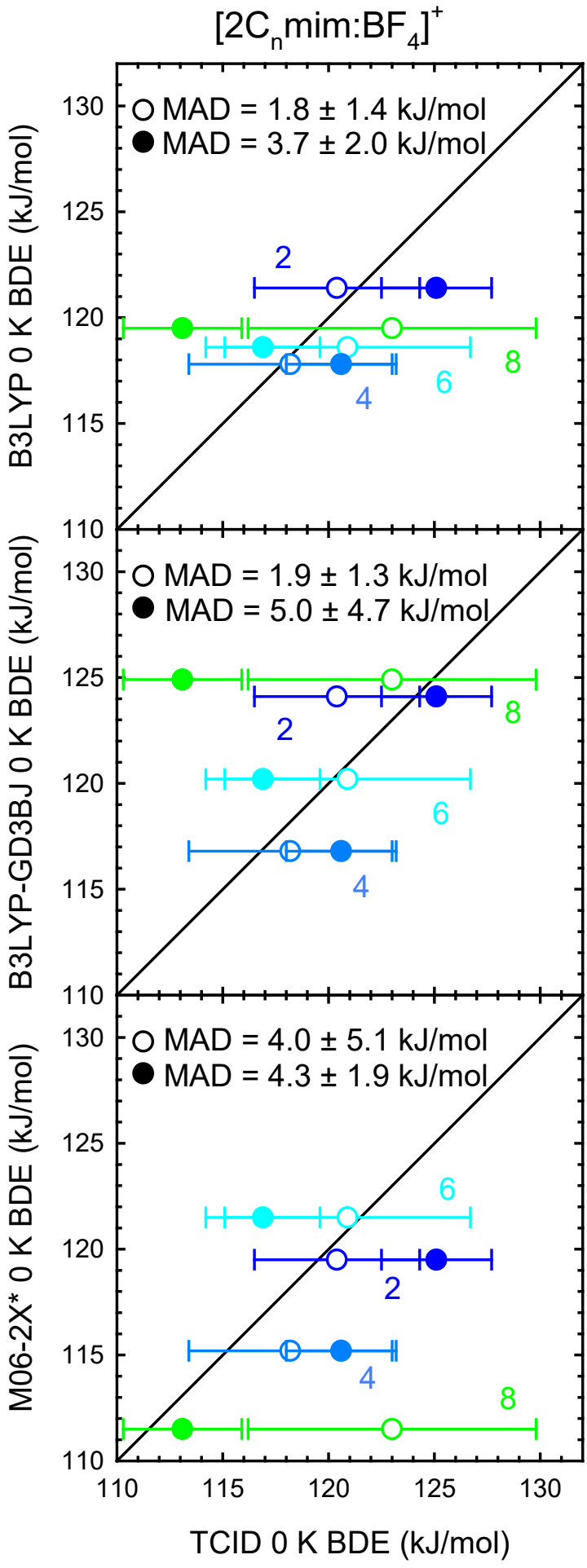
[2C$_n$mim:BF$_4$]$^+$
B3LYP 0 K BDE (kJ/mol)
B3LYP-GD3BJ 0 K BDE (kJ/mol)
M06-2X* 0 K BDE (kJ/mol)
TCID 0 K BDE (kJ/mol)
MAD = 1.8 ± 1.4 kJ/mol
MAD = 3.7 ± 2.0 kJ/mol
MAD = 1.9 ± 1.3 kJ/mol
MAD = 5.0 ± 4.7 kJ/mol
MAD = 4.0 ± 5.1 kJ/mol
MAD = 4.3 ± 1.9 kJ/mol
2
4
6
8
110
115
120
125
130

TOC.

@ 200%

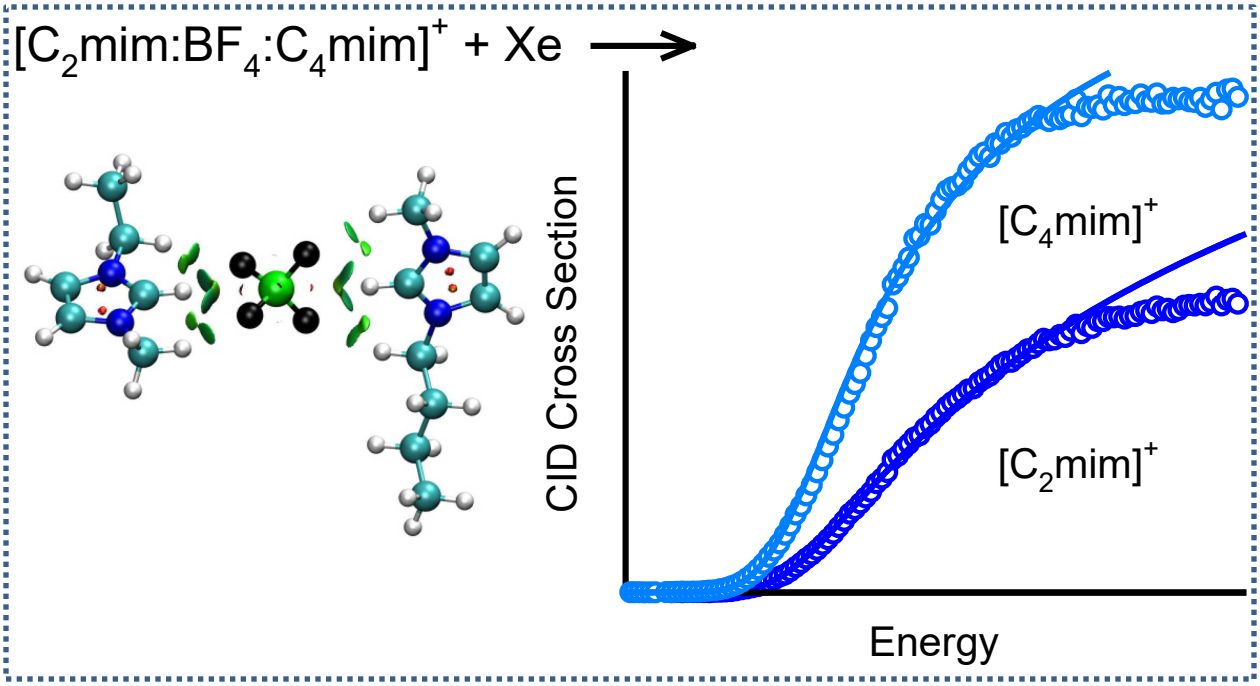
[C2mim:BF4:C4mim]+ + Xe
CID Cross Section
[C4mim]+
[C2mim]+
Energy

@ 100%

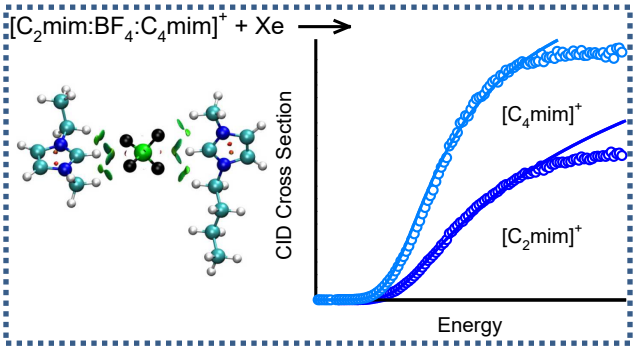
[C2mim:BF4:C4mim]+ + Xe
CID Cross Section
[C4mim]+
[C2mim]+
Energy

Supporting Information for…

Absolute Trends and Accurate and Precise Gas-Phase Binding Energies of 1-Alkyl-3-Methylimidazolium Tetrafluoroborate Ionic Liquid Clusters

H. A. Roy and M. T. Rodgers*
Department of Chemistry, Wayne State University, Detroit, MI, 48202, USA

Table S1. CID Fragments of the $[C_{n-2}mim{:}BF_4{:}C_nmim]^+$ Cluster Ions.[a]

precursor ion	m/z (Da/*e*)	symbol	1° fragment ion	2° fragment ions	neutral loss(es)
$[C_2mim{:}BF_4{:}C_4mim]^+$	337				
	139	●	$[C_4mim]^+$		$(C_2mim{:}BF_4)$
	111	●	$[C_2mim]^+$		$(C_4mim{:}BF_4)$
	83	□		$[C_4H_7N_2]^+$	C_4H_8
	57	△		$[C_4H_9]^+$	$C_4H_6N_2$
$[C_4mim{:}BF_4{:}C_6mim]^+$	393				
	167	●	$[C_6mim]^+$		$(C_4mim{:}BF_4)$
	139	●	$[C_4mim]^+$		$(C_6mim{:}BF_4)$
	83	□		$[C_4H_7N_2]^+$	$C_5H_8N_2$
	57	△		$[C_4H_9]^+$	$C_6H_{10}N_2$
	43	○		$[C_3H_7]^+$	$C_7H_{12}N_2$
$[C_6mim{:}BF_4{:}C_8mim]^+$	449				
	195	●	$[C_8mim]^+$		$(C_6mim{:}BF_4)$
	167	●	$[C_6mim]^+$		$(C_8mim{:}BF_4)$
	83	□		$[C_4H_7N_2]^+$	C_8H_{16}

[a]The elemental compositions of the $[C_nmim]^+$ cations are $[C_2mim]^+ = [C_6H_{11}N_2]^+$, $[C_4mim]^+ = [C_8H_{15}N_2]^+$, $[C_6mim]^+ = [C_{10}H_{19}N_2]^+$, and $[C_8mim]^+ = [C_{12}H_{23}N_2]^+$.

Table S2. Geometric Parameters of the B3LYP, B3LYP-GD3BJ, and M06-2X Ground Conformers of the $[C_nmim]^+$ Cations[a]

cation	theory	a1	a2	a3	a4	a5	a6	a7
$[C_2mim]^+$	B3LYP	-104.6						
	B3LYP-GD3BJ	-104.6						
	M06-2X	-108.0						
$[C_4mim]^+$	B3LYP	-100.1	-179.7	-179.6				
	B3LYP-GD3BJ	-103.5	61.9	177.3				
	M06-2X	-106.2	59.1	175.5				
$[C_6mim]^+$	B3LYP	-102.1	180.0	180.0	180.0	180.0		
	B3LYP-GD3BJ	-104.5	60.9	176.4	179.5	179.7		
	M06-2X	-106.4	58.9	174.0	179.2	179.4		
$[C_8mim]^+$	B3LYP	-103.0	179.3	179.8	179.5	180.0	179.7	180.0
	B3LYP-GD3BJ	-103.4	60.5	176.1	179.5	179.6	180.0	179.9
	M06-2X	-104.9	59.2	174.7	180.0	179.8	179.6	180.0

[a]The torsion angles are given in (°) and describe the 1-alkyl dihedral angles: a1 = ∠C2N1C1′C2′, a2 = ∠N1C1′C2′C3′, a3 = ∠C1′C2′C3′C4′, a4 = ∠C2′C3′C4′C5′, a5 = C3′C4′C5′C6′, a6 = C4′C5′C6′C7′, and a7 = ∠C5′C6′C7′C8′ as shown in **Figure S1**. The optimized structures were determined using the density functional indicated with a 6-311+G(d,p) basis set and are shown in **Figure 4** and **Figures S3-S6**.

Table S3. Geometric Parameters of B3LYP, B3LYP-GD3BJ, and M06-2X Optimized Geometries of the $[BF_4]^-$ Anion[a]

theory	B-F (Å)	∠FBF (°)
B3LYP	1.417	109.5
B3LYP-GD3BJ	1.417	109.5
M06-2X	1.410	109.5

[a]The optimized structures were determined using the density functional indicated with a 6-311+G(d,p) basis set.

Table S4. Geometric Parameters of the B3LYP, B3LYP-GD3BJ, and M06-2X Ground Conformers of the ($C_n$mim:BF_4) Ion Pairs[a]

ion pair	theory	∠C2N3C1″H	a1[b]	∠C2HB	**b**[c]	**b1**[d]
(C_2mim:BF_4)	B3LYP	-22.9	-102.5	117.6	2.4	51.1
	GD3BJ	-0.7	-38.3	106.3	-6.0	53.0
	M06-2X	-27.6	-115.1	93.4	-2.1	-61.7
(C_4mim:BF_4)	B3LYP	-26.0	-60.4	124.7	1.9	45.7
	GD3BJ	20.4	-103.5	111.6	-0.3	-53.9
	M06-2X	26.6	-35.6	91.8	-4.7	60.8
(C_6mim:BF_4)	B3LYP	-5.8	-87.1	118.4	-4.0	44.7
	GD3BJ	19.0	-103.2	112.2	-0.7	-52.9
	M06-2X	-25.1	-112.3	94.4	-2.0	-61.9
(C_8mim:BF_4)	B3LYP	-19.2	78.5	124.6	-5.7	42.9
	GD3BJ	-24.3	108.8	122.6	-1.8	46.4
	M06-2X	-22.3	-110.7	94.2	-1.6	-62.3

ion pair	theory	C1′H-F	C2H-F	C1″H□F	C2-F	C2-B
(C_2mim:BF_4)	B3LYP	2.294	2.072, 2.288	2.228	2.835	3.114
	GD3BJ	2.489	2.424, 2.051	2.365	2.851	3.052
	M06-2X	2.408	2.317, 2.294	2.617	2.709	2.937
(C_4mim:BF_4)	B3LYP	2.323	1.906, 2.428	2.241	2.950	3.166
	GD3BJ	2.442	2.222, 2.199	2.206	2.768	3.067
	M06-2X	2.365	2.392, 2.255	2.576	2.723	2.933
(C_6mim:BF_4)	B3LYP	2.261	2.296, 2.056	2.321	2.843	3.118
	GD3BJ	2.455	2.217, 2.199	2.204	2.758	3.066
	M06-2X	2.409	2.314, 2.284	2.589	2.717	2.943
(C_8mim:BF_4)	B3LYP	3.271	2.017, 2.435	2.094	2.882	3.211
	GD3BJ	2.906	1.889, 2.553	2.162	2.863	3.165
	M06-2X	2.371	2.299, 2.318	2.566	2.758	2.956

[a]Bond and dihedral angles are given in (°); bond distances are given in Angstroms. The optimized structures were determined using the density functional indicated with a 6-311+G(d,p) basis set and are shown in **Figure 6** and **Figures S7-S10**. See **Figure S1** for dihedral definitions. [b]First 1-alkyl dihedral angle a1 ≡ ∠C2N1C1′C2′. [c]Binding site dihedral angle defined as **b** ≡ ∠(C2,©,©+CP,B), where © denotes the centroid of the imidazolium ring. [d]Binding orientation dihedral angle defined as **b1** ≡ ∠C1″N3C2B.

Table S5. Geometric Parameters of the B3LYP, B3LYP-GD3BJ, and M06-2X Ground Conformers of the $[C_{n-2}mim:BF_4:C_nmim]^+$ Clusters[a]

system	Theory	∠C2N3C1″H	a1[b]	∠C2HB	**b**[c]	**b1**[d]	**b2**[e]
$[C_2mim:BF_4:C_4mim]^+$	B3LYP	-1.2	-106.4	176.1	-1.5	3.0	-100.1
		0.6	-103.9	176.7	-1.2	0.9	
	B3LYP-GD3BJ	1.8	-103.1	176.4	0.0	-3.7	-95.0
		-1.7	96.5	176.6	1.3	2.8	
	M06-2X	15.8	-110.0	119.1	1.1	-52.5	103.8
		-6.8	79.5	164.6	-0.2	14.4	
$[C_4mim:BF_4:C_6mim]^+$	B3LYP	-0.1	-105.1	176.9	-1.4	1.2	-89.6
		-1.3	102.6	177.1	-1.5	0.0	
	B3LYP-GD3BJ	-6.8	89.0	165.0	2.9	14.7	-89.8
		6.9	-90.8	161.3	2.3	-18.3	
	M06-2X	17.3	101.4	115.7	-24.5	34.1	149.2
		12.1	-102.2	146.8	-0.2	-29.8	
$[C_6mim:BF_4:C_8mim]^+$	B3LYP	0.6	-101.8	176.2	-1.7	1.2	88.8
		2.7	107.9	174.6	-2.0	-3.5	
	B3LYP-GD3BJ	-1.8	-67.7	153.6	14.1	3.1	79.8
		-20.1	83.7	132.6	1.9	43.1	
	M06-2X	-16.5	103.0	139.9	-2.0	32.7	-80.4
		12.3	-122.8	143.0	-0.7	-31.4	

system	Theory	C1′H-F	C2H-F	C1″H-F	C2-B
$[C_2mim:BF_4:C_4mim]^+$	B3LYP	2.483	2.070, 2.121	2.349	3.662
		2.529	2.071, 2.133	2.339	3.669
	B3LYP-GD3BJ	2.422	2.061, 2.058	2.369	3.616
		2.409	2.093, 2.036	2.445	3.618
	M06-2X	2.433	2.219, 2.260	2.312	3.382
		2.736	2.058, 2.038	2.317	3.578
$[C_4mim:BF_4:C_6mim]^+$	B3LYP	2.512	2.072, 2.126	2.341	3.666
		2.532	2.070, 2.133	2.346	3.668
	B3LYP-GD3BJ	2.462	2.126, 2.027	2.525	3.608
		2.509	2.154, 2.010	2.482	3.601
	M06-2X	4.140	2.039, -	2.465	3.422
		2.485	2.072, 2.138	2.335	3.541
$[C_6mim:BF_4:C_8mim]^+$	B3LYP	2.551	2.064, 2.137	2.328	3.667
		2.533	2.064, 2.143	2.314	3.669
	B3LYP-GD3BJ	2.291	2.382, 1.962	3.283	3.651
		2.772	2.076, 2.261	2.379	3.443
	M06-2X	2.618	1.977, 2.245	2.318	3.484
		2.550	2.024, 2.158	2.217	3.484

[a]Bond and dihedral angles are given in (°). The optimized structures were determined using the density functional indicated with a 6-311+G(d,p) basis set and are shown in **Figure 5** and **Figures S3-5**. See **Figure S1** for dihedral definitions. [b]First 1-alkyl dihedral angle a1 ≡ ∠C2N1C1′C2′. [c]Binding site dihedral angle defined as **b** ≡ ∠(C2,©,©+CP,B), where © denotes the centroid of the imidazolium ring. [d]Binding orientation dihedral angle defined as **b1** ≡ ∠C1″N3C2B. [e]Relative cation binding orientation dihedral angle defined as **b2** ≡ ∠C1′N1N1C1′.

Table S6. Vibrational Frequencies and Average Vibrational Energies of the $[C_{n-2}mim:BF_4:C_nmim]^+$ Clusters, the $[C_nmim]^+$ Cations, and ($C_nmim:BF_4$) Ion Pairs [a]

system	E_{int}, eV[b]	vibrational frequencies (cm^{-1})
$[C_2mim:BF_4:C_4mim]^+$	0.74 (0.05)	10, 12(2), 20, 29, 32, 37, 45, 46, 58, 73, 76, 77, 80, 85, 113, 116, 121, 129, 141, 199, 210, 233, 239, 248, 282, 298, 318, 329, 361, 378, 406, 429, 439, 496, 497, 517, 596, 628, 635(2), 663, 667, 699, 736, 744(2), 749, 749, 806, 810, 867, 868, 907, 912, 918, 951, 964, 1013(2), 1016, 1031, 1038, 1048, 1049, 1056, 1058, 1102, 1108, 1109, 1121, 1122, 1130, 1141, 1155, 1157, 1158, 1177(2), 1239, 1274, 1295, 1302, 1313, 1321, 1338, 1345, 1348, 1386, 1389, 1400, 1414, 1416, 1422, 1426, 1446, 1448, 1464, 1465, 1491, 1494(2), 1495, 1498(2), 1502, 1505, 1512, 1513(2), 1516, 1592(2), 1604(2), 3014, 3022, 3028, 3040, 3043, 3062, 3063(2), 3071, 3074, 3090, 3100, 3108, 3119, 3127, 3137, 3139, 3140, 3165(2), 3246, 3251, 3275(2), 3293(2)
$[C_4mim:BF_4:C_6mim]^+$	0.89 (0.06)	4, 7, 9, 15, 19, 27, 35, 38, 42, 45, 53, 57, 69, 70, 76, 79, 81, 85, 113, 119, 127, 128, 132, 135, 146, 200, 214, 239(2), 245, 248, 281, 286, 295, 318, 329, 361, 405, 409, 438, 440, 452, 496(2), 517, 628, 629, 635, 636, 667, 669, 736(2), 740, 743, 744, 748, 749, 753, 804, 805, 866, 867, 899, 900, 908, 911, 918, 949, 1003, 1008, 1012, 1014, 1016, 1030, 1038(2), 1046, 1048, 1052, 1056, 1058, 1065, 1108(2), 1121, 1122, 1129, 1136, 1154, 1156, 1157, 1158, 1177(2), 1221, 1239, 1264, 1274, 1293, 1301, 1302, 1321, 1323, 1327, 1336, 1337, 1340, 1347, 1348, 1381, 1385, 1398, 1399, 1404, 1416, 1418(2), 1422, 1446(2), 1464(2), 1488, 1490(2), 1494(2), 1498, 1499, 1501, 1502(2), 1505, 1510, 1513(2), 1515, 1517, 1592(2), 1603, 1604, 2999, 3005, 3013(2), 3019, 3021, 3022, 3023, 3028, 3034, 3039, 3049, 3061, 3062, 3063, 3064, 3070, 3072, 3084, 3090, 3092, 3100, 3127, 3128, 3139(2), 3165, 3166, 3247, 3251, 3274, 3275, 3292, 3293
$[C_6mim:BF_4:C_8mim]^+$	1.04 (0.07)	5, 8, 11, 16, 18, 27, 30, 35(2), 41, 43, 48, 50, 58, 61, 70, 77, 79, 80, 91, 96, 109, 121, 122, 126, 129, 136, 145(2), 158, 176, 194, 215, 240, 242, 245, 247, 286(2), 296, 313, 329, 361, 373, 410, 418, 439, 448, 452, 494, 496(2), 517, 628, 629, 636(2), 670(2), 734, 736, 739, 740(2), 744, 748, 749, 752, 759, 804(2), 866, 867, 875, 899(2), 900, 912, 913, 957, 994, 1004, 1006, 1010, 1014, 1015, 1030, 1034, 1038, 1039, 1041, 1047, 1049, 1053, 1056, 1061, 1065, 1069, 1073, 1108(2), 1121, 1122, 1136, 1138, 1156, 1157, 1158, 1160, 1177(2), 1213, 1221, 1245, 1254, 1266, 1274, 1287, 1294, 1302, 1307, 1324, 1326, 1328, 1329, 1338, 1339, 1342, 1342(2), 1348(2), 1379, 1381, 1395, 1398, 1401, 1403, 1404, 1416(3), 1417, 1445, 1446, 1464(2), 1486, 1487, 1488, 1489, 1491, 1493(2), 1499(3), 1500, 1501(2), 1506, 1510, 1512, 1513(2), 1516, 1518, 1592(2), 1603(2), 2995, 2997, 2999, 3002, 3005, 3008, 3012(2), 3013(2), 3019, 3021, 3022(2), 3024, 3031, 3034(2), 3050, 3053, 3062, 3063(2), 3064, 3070, 3071, 3082, 3084, 3089, 3093, 3126, 3127, 3139(2), 3166(2), 3246, 3250, 3275(2), 3293(2)
$[C_2mim]^+$	0.19 (0.02)	46, 69, 135, 209, 233, 292, 378, 425, 592, 633, 660, 698, 753, 803, 834, 881, 962, 1036, 1043, 1099, 1102, 1124, 1136, 1150, 1175, 1270, 1311, 1343, 1385, 1411, 1428, 1437, 1461, 1484, 1491, 1494, 1509, 1510, 1595, 1604, 3046, 3070, 3079, 3110, 3122, 3134, 3150, 3165, 3274, 3278, 3292
$[C_4mim]^+$	0.27 (0.02)	28, 65, 69, 83, 112, 199, 237, 247, 273, 318, 407, 434, 626, 632, 664, 733, 741, 752, 801, 834, 879, 916, 946, 1010, 1037, 1042, 1054, 1100, 1125, 1128, 1147, 1150, 1175, 1234, 1295, 1299, 1318, 1336, 1345, 1381, 1395, 1412, 1424, 1436, 1460, 1484, 1489, 1492, 1502(2), 1510, 1515, 1594, 1603, 3015, 3025, 3032, 3041, 3065, 3069, 3072, 3094, 3108, 3121, 3149, 3165, 3274, 3279, 3292

Table S6. Vibrational Frequencies and Average Vibrational Energies of the $[C_{n-2}mim:BF_4:C_nmim]^+$ Clusters, the $[C_nmim]^+$ Cations, and ($C_nmim:BF_4$) Ion Pairs [a]

system	E_{int}, eV[b]	vibrational frequencies (cm^{-1})
$[C_6mim]^+$	0.34 (0.03)	28, 49, 52, 63, 76, 124, 131, 147, 214, 238, 245, 278, 294, 408, 437, 449, 626, 631, 666, 736, 737, 750, 754, 802, 833, 881, 897, 901, 1001, 1007, 1035, 1037, 1041, 1046, 1062, 1099, 1125, 1135, 1149, 1154, 1174, 1219, 1262, 1272, 1303, 1320, 1326, 1336, 1340, 1344, 1378, 1394, 1401, 1412, 1420, 1436, 1460, 1484, 1488, 1489, 1493, 1500, 1502, 1510(2), 1510, 1517, 1595, 1603, 3001, 3006, 3015, 3022, 3024, 3026, 3035, 3051, 3067, 3068, 3072, 3086, 3098, 3122, 3148, 3164, 3274, 3277, 3291
$[C_8mim]^+$	0.42 (0.03)	20, 38, 40, 53, 70, 93, 96, 107, 149, 156, 175, 193, 242(2), 279, 311, 374, 416, 448, 492, 626, 631, 666, 734, 736, 738, 752, 757, 801, 833, 872, 880, 900, 955, 994, 1004, 1032, 1036, 1038, 1044, 1059, 1064, 1072, 1100, 1125, 1138, 1148, 1155, 1172, 1211, 1245, 1251, 1286, 1294, 1306, 1322, 1329, 1338, 1340, 1342, 1345, 1378, 1392, 1402, 1403, 1412, 1419, 1435, 1461, 1484, 1486, 1487, 1491, 1492, 1497, 1501, 1505, 1511, 1512, 1517, 1594, 1603, 2996, 2999, 3004, 3009, 3014(2), 3022(2), 3025, 3032, 3044, 3055, 3068(2), 3071, 3083, 3091, 3120, 3148, 3164, 3275, 3277, 3292
($C_2mim:BF_4$)	0.36 (0.03)	8, 35, 43, 66, 75, 86, 109, 124, 179, 213, 237, 302, 342, 346, 383, 430, 497, 500, 507, 597, 636, 671, 705, 735, 736, 805, 854, 930, 951, 965, 996, 1040, 1050, 1103, 1111, 1120, 1140, 1157, 1161, 1181, 1271, 1313, 1353, 1392, 1412, 1424, 1456, 1464, 1494, 1497, 1505, 1509, 1516, 1596, 1603, 3036, 3056, 3077, 3099, 3112, 3135, 3137, 3158, 3257, 3276, 3295
($C_4mim:BF_4$)	0.44 (0.03)	28, 40, 42, 56, 65, 82, 89, 94, 117, 130, 148, 213, 244, 249, 284, 326, 343, 346, 408, 446, 498, 500, 508, 630, 642, 674, 735, 736, 738, 747, 807, 856, 913, 935, 953, 957, 989, 1013, 1039, 1047, 1060, 1109, 1120, 1129, 1156, 1157, 1162, 1178, 1241, 1297, 1305, 1322, 1343, 1353, 1380, 1404, 1413, 1419, 1450, 1463, 1492, 1494, 1501, 1503, 1504, 1509, 1515, 1595, 1604, 3004, 3011, 3023, 3046, 3056(2), 3084, 3090, 3096, 3131, 3137, 3157, 3266, 3276, 3295
($C_6mim:BF_4$)	0.52 (0.04)	19, 25, 36, 44, 53, 63, 71, 79, 92, 111, 127, 133, 147, 155, 226, 244, 245, 287, 300, 343, 345, 410, 442, 459, 498, 499, 507, 630, 642, 674, 736(3), 740, 754, 806, 855, 898, 900, 925, 958, 989, 1004, 1009, 1036, 1039, 1046, 1053, 1066, 1109, 1120, 1135, 1155, 1158, 1164, 1175, 1223, 1265, 1275, 1301, 1325, 1329, 1337, 1343, 1353, 1379, 1399, 1404, 1415, 1416, 1450, 1463, 1487, 1489, 1495, 1500(2), 1504, 1508, 1509, 1516, 1594, 1603, 2994, 2996, 3006, 3012, 3019, 3026, 3037, 3053, 3056(2), 3080, 3085, 3089, 3132, 3136, 3157, 3267, 3277, 3296
($C_8mim:BF_4$)	0.59 (0.04)	1, 23, 28, 41, 43, 48, 55, 75, 81, 92, 106, 117, 130, 143, 158, 177, 193, 225, 245, 256, 293, 324, 343, 347, 393, 419, 470, 497, 501, 507, 511, 598, 636, 668, 704, 735, 737, 739, 745, 778, 836, 856, 875, 899, 923, 930, 969, 978, 989, 1007, 1027, 1040, 1042, 1049, 1057, 1066, 1082, 1110, 1121, 1137, 1154, 1159, 1162, 1179, 1216, 1233, 1258, 1278, 1303, 1311, 1319, 1331, 1339, 1346, 1352, 1364, 1387, 1396, 1402, 1403, 1414, 1415, 1451, 1464, 1485, 1486, 1489, 1492, 1495, 1499, 1500, 1506, 1507, 1508, 1514, 1591, 1604, 2981, 2991, 2996, 3003, 3006, 3015, 3019, 3023, 3024, 3038, 3045, 3053, 3061, 3063, 3080, 3083, 3103, 3119, 3136, 3155, 3227, 3278, 3296

[a] Determined at the B3LYP/6-311+G(d,p) level of theory and with frequencies scaled by 0.9887. Degeneracies are listed in parentheses. [b] Uncertainties are listed in parentheses.

Table S7. Rotational Constants (in cm^{-1}) of $[C_{n-2}mim:BF_4:C_nmim]^+$ Clusters and the Corresponding PSL Transition States

system	ionic product	energized molecule		transition state		
		1-D[a]	2-D[b]	1-D[c]	2-D[c]	2-D[d]
$[C_4mim:BF_4:C_6mim]^+$	$[C_2mim]^+$	0.0112	0.00280	0.178, 0.0208	0.0393, 0.0115	0.0012
	$[C_4mim]^+$	0.0112	0.00280	0.132, 0.0324	0.0167, 0.0162	0.0012
$[C_4mim:BF_4:C_6mim]^+$	$[C_4mim]^+$	0.00529	0.00209	0.132, 0.0198	0.0167, 0.00558	0.0008
	$[C_6mim]^+$	0.00529	0.00209	0.110, 0.0208	0.00831, 0.0115	0.0009
$[C_6mim:BF_4:C_8mim]^+$	$[C_6mim]^+$	0.00311	0.00142	0.110, 0.0143	0.00831, 0.00488	0.0007
	$[C_8mim]^+$	0.00311	0.00142	0.096, 0.0198	0.00460, 0.00558	0.0007

[a]Active external. [b]Inactive external. [c]Rotational constants of the transition state treated as free internal rotors. [d]Two-dimensional rotational constants of the transition state at threshold, treated variationally and statistically.

Table S8. Fitting Parameters of eq 5, Threshold Dissociation Energies at 0 K, and Entropies of Activation at 1000 K of $[C_{n-2}mim:BF_4:C_nmim]^+$ Clusters Based on Independent Fitting of the Two Primary Dissociation Pathways[a]

system	Ionic Product	σ^b	n	$E_0{}^c$ (eV)	E_0(PSL)[b] (eV)	kinetic shift (eV)	$\Delta S^{\ddagger}$(PSL)[b] (J mol^{-1} K^{-1})
$[C_2mim:BF_4:C_4mim]^+$	$[C_2mim]^+$	33.2 (0.9)	1.1 (0.1)	2.12 (0.06)	1.27 (0.04)	0.85	25 (4)
	$[C_4mim]^+$	67.5 (1.6)	1.0 (0.1)	2.05 (0.06)	1.26 (0.04)	0.79	31 (4)
$[C_4mim:BF_4:C_6mim]^+$	$[C_4mim]^+$	18.4 (0.3)	1.2 (0.1)	2.30 (0.09)	1.22 (0.06)	1.08	26 (4)
	$[C_6mim]^+$	25.8 (0.6)	1.1 (0.1)	2.35 (0.08)	1.20 (0.06)	1.15	17 (4)
$[C_6mim:BF_4:C_8mim]^+$	$[C_6mim]^+$	21.8 (1.0)	1.2 (0.1)	2.71 (0.09)	1.31 (0.07)	1.40	44 (4)
	$[C_8mim]^+$	24.0 (2.8)	1.2 (0.1)	2.67 (0.11)	1.26 (0.07)	1.41	38 (4)

[a]Present results, uncertainties are listed in parentheses. [b]Average values for loose PSL TS. [c]No RRKM analysis.

FIGURE CAPTIONS

Figure S1. Nomenclature employed in this work to describe the stable conformations predicted for the $[C_nmim]^+$ cations, ($C_nmim:BF_4$) ion pairs, and $[2C_nmim:BF_4]^+$ clusters.

Figure S2. Electrostatic potential maps of the B3LYP/6-311+G(d,p) ground conformers of the $[C_{n-2}mim:BF_4:C_nmim]^+$ clusters. The ESP maps are shown at an isosurface of 0.01 a.u. of the total B3LYP/6-311+G(2d,2p) SCF electron density. The Mülliken charges on the hydrogen atoms of the cations and fluorine atoms of the anion are labeled. The most electropositive regions are color-coded in blue and occur at the hydrogen atoms of the 3-methylimidazolium moiety, with the C2 hydrogen atom displaying the greatest Mülliken charge. The most electronegative regions are color-coded in red, and occur at the fluorine atoms of the anion. Regions of intermediate ESP are shown in green and yellow and become more prevalent as the size of the 1-alkyl substituent increases.

Figure S3. B3LYP/6-311+G(d,p) optimized geometries of the ground and select stable conformers of the $[C_2mim:BF_4:C_4mim]^+$ cluster. Conformer designations along with the B3LYP/6-311+G(2d,2p), B3LYP-GD3BJ/6-311+G(2d,2p) and M06-2X/6-311+G(2d,2p) relative Gibbs energies at 298 K (in kJ/mol) are also listed. Values indicated with an asterisk required use of an ultrafine integration grid during optimization and frequency analysis for proper convergence.

Figure S4. B3LYP/6-311+G(d,p) optimized geometries of the ground and select stable conformers of the $[C_4mim:BF_4:C_6mim]^+$ cluster. Conformer designations along with the B3LYP/6-311+G(2d,2p), B3LYP-GD3BJ/6-311+G(2d,2p) and M06-2X/6-311+G(2d,2p) relative Gibbs energies at 298 K (in kJ/mol) are also listed. Values indicated with an asterisk required use of an ultrafine integration grid during optimization and frequency analysis for proper convergence. Conformers not determined upon M06-2X re-optimization of the B3LYP optimized structures (due to significant structural rearrangement) are indicated with a dash.

Figure S5. B3LYP/6-311+G(d,p) optimized geometries of the ground and select stable conformers of the $[C_2mim:BF_4:C_4mim]^+$ cluster. Conformer designations along with the B3LYP/6-311+G(2d,2p), B3LYP-GD3BJ/6-311+G(2d,2p) and M06-2X/6-311+G(2d,2p) relative Gibbs energies at 298 K (in kJ/mol) are also listed. Values indicated with an asterisk required use of an ultrafine integration grid during optimization and frequency analysis for proper convergence. Conformers not determined upon M06-2X re-optimization of the B3LYP optimized structures (due to significant structural rearrangement) are indicated with a dash.

Figure S1.

$[C_n mim]^+$ Nomenclature

$[a1a2\ldots an\text{-}1]^+$

$[C_2mim]^+ = [a1]^+$

$[C_4mim]^+ = [a1a2a3]^+$

$[C_6mim]^+ = [a1a2a3a4a5]^+$

$[C_8mim]^+ = [a1a2a3a4a5a6a7]^+$

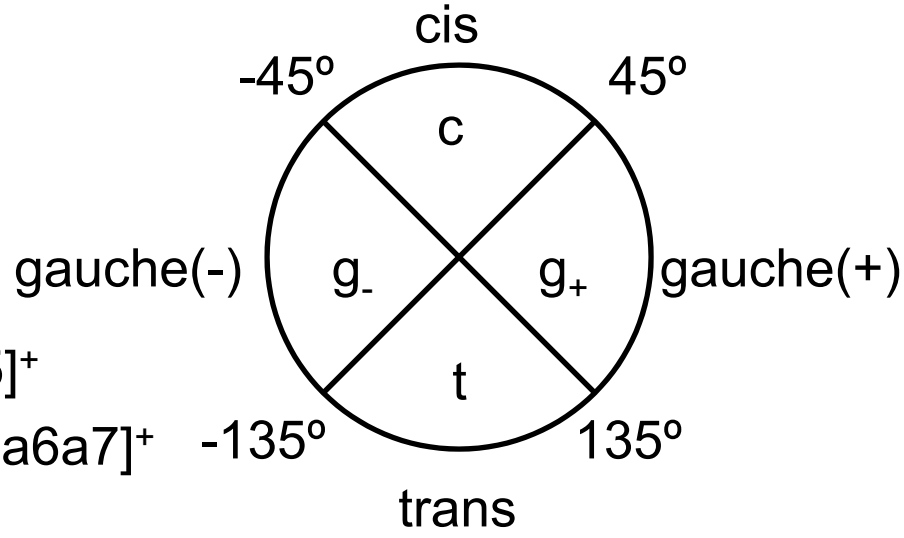

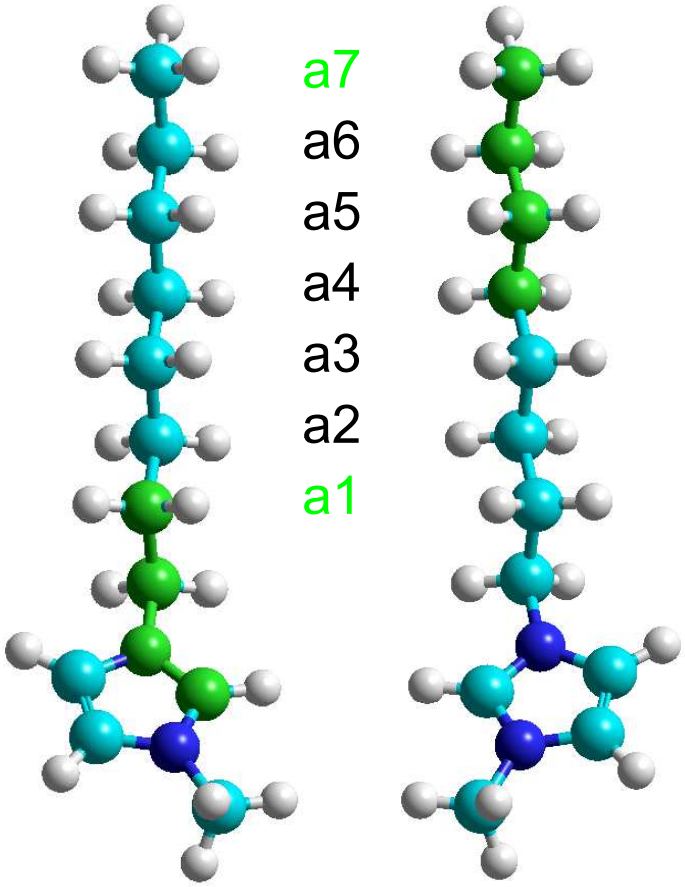

$[g_-ttttt]^+$ $[g_-t_6]^+$

$[g_+ttttt]^+$ $[g_+t_6]^+$

$[C_8mim]^+$

Dihedral Angle Classification

1-Alkyl Dihedral Angles

a1 = ∠C2N1C1′C2′
a2 = ∠N1C1′C2′C3′
a3 = ∠C1′C2′C3′C4′
a4 = ∠C2′C3′C4′C5′
a5 = ∠C3′C4′C5′C6′
a6 = ∠C4′C5′C6′C7′
a7 = ∠C5′C6′C7′C8′

Figure S1.

Binding Site (BS) Nomenclature

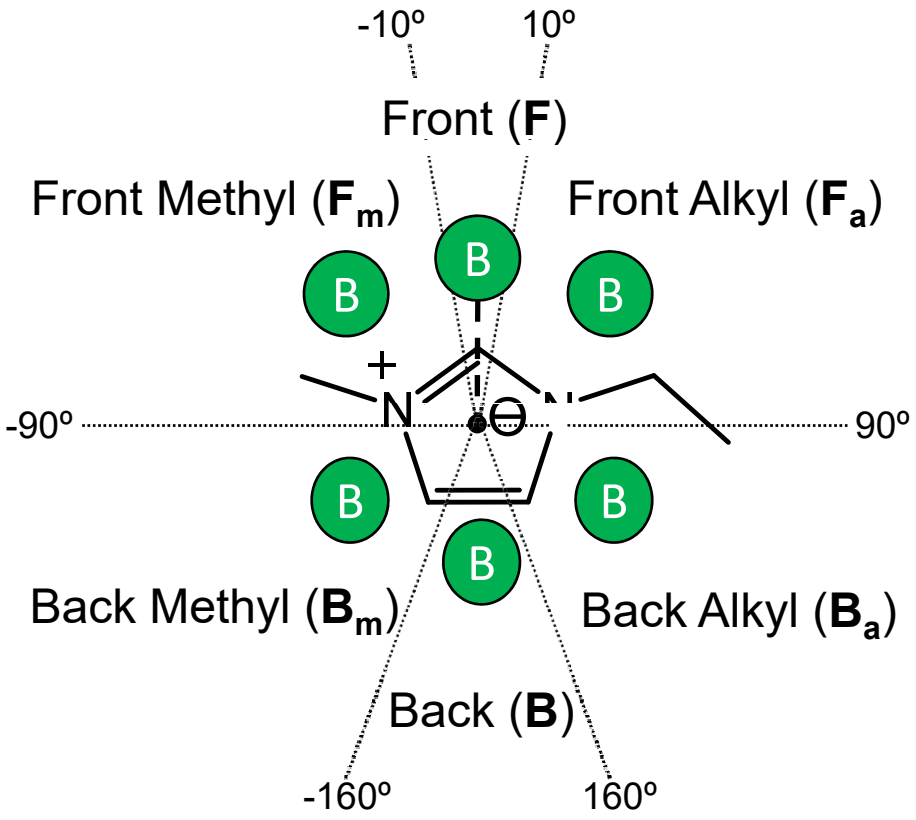

The **binding site** (**BS**) designation is readily described by the dihedral angle **b** = ∠(C2,©,©+CP,B), where © denotes the centroid of the imidazolium ring (N1C2N3C4C5) and CP denotes the cross product of the vectors that describe the C2-N1 and C2-N3 bonds, i.e., CP = $(\overrightarrow{C2\text{-}N1})x(\overrightarrow{C2\text{-}N3})$. The range of angles that define BS designations are shown in the figure above and the bar below.

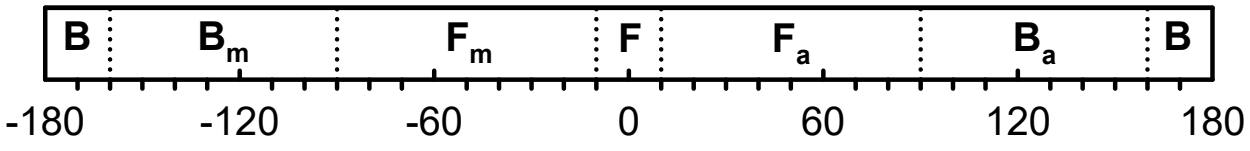

b (Binding Site Dihedral Angle, deg)

Figure S1.

Binding Site (BS) Nomenclature

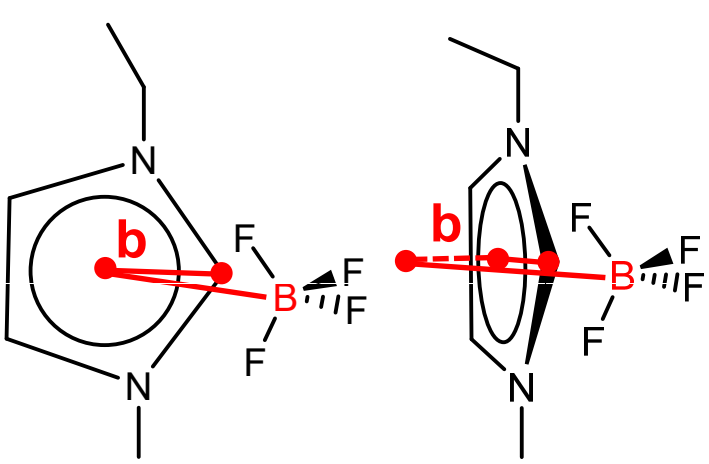

Front Binding (**F**)

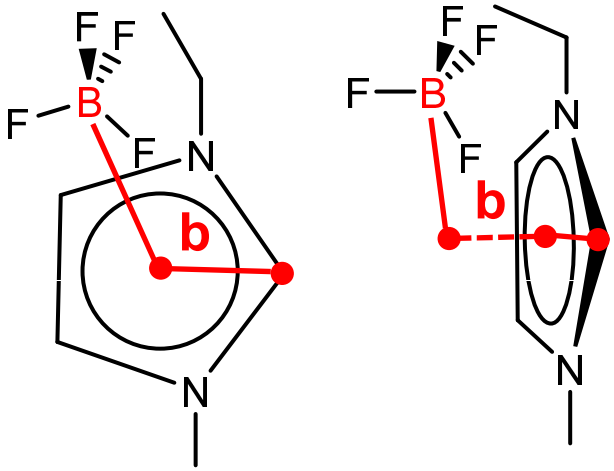

Back Alkyl Binding ($\mathbf{B_a}$)

The **binding site** (**BS**) designation is readily described by the dihedral angle **b** = ∠(C2,©,©+CP,B), where © denotes the centroid of the imidazolium ring (N1C2N3C4C5) and CP denotes the cross product of the vectors that describe the C2-N1 and C2-N3 bonds, i.e., CP = $(\overrightarrow{C2\text{-}N1})x(\overrightarrow{C2\text{-}N3})$. The range of angles that define BS designations are shown in the figure above and the bar below.

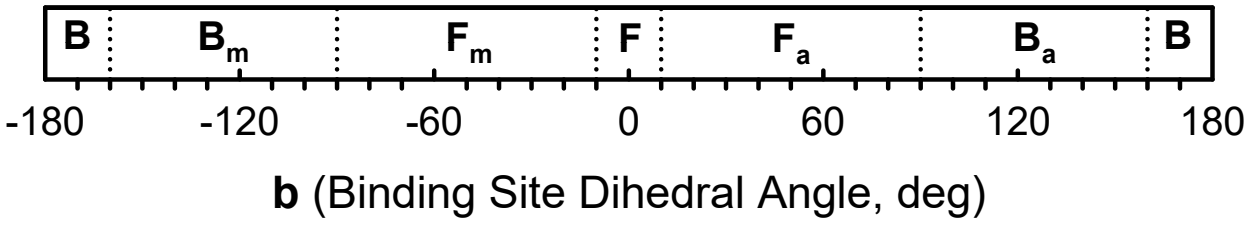

Figure S1.

($C_n$mim:BF_4) Nomenclature

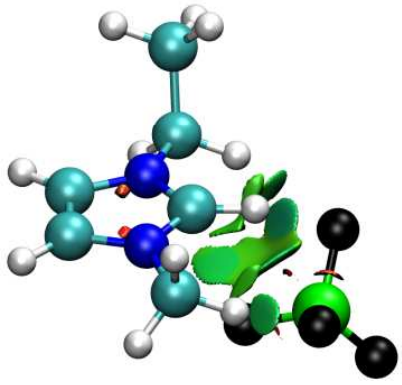

(C_2mim:BF_4)

(**g_+F**;g_-)

(**Binding Site**;Alkyl$_n$)

(**b1BS**;a1…an)

b1 = ∠C1″N3C2B

[C_{n-2}mim:BF_4:$C_n$mim]$^+$ Nomenclature

[Alkyl$_{n-2}$;**BindingSites**;Alkyl$_n$]$^+$

[a1…an-2;**b2b1BS(n-2)b1BS(n)**; a1…an]$^+$

b2 = ∠C1′N1(n-2)N1C1′(n)

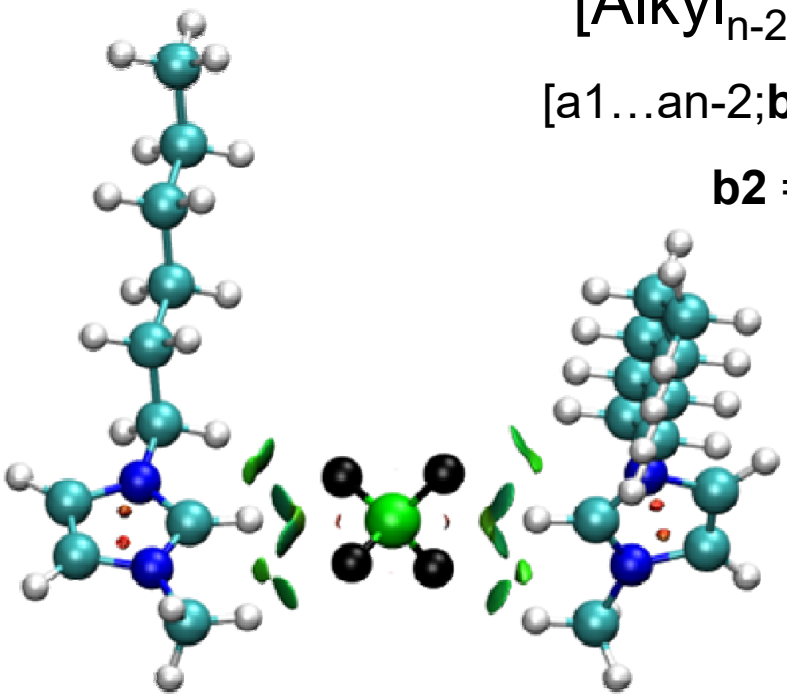

[C_6mim:BF_4:C_8mim]$^+$

[g_-t_4;**g_+cFcF**;g_+t_6]$^+$

Figure S2.

B3LYP/6-311+G(d,p)

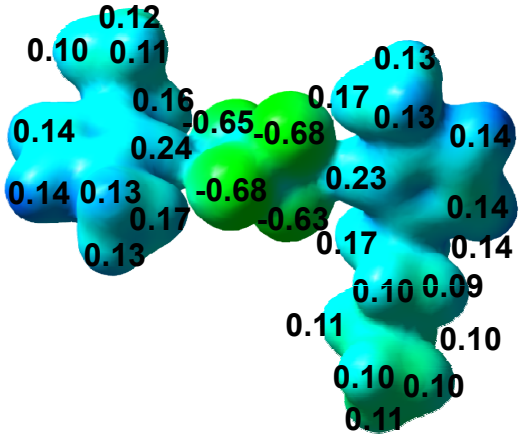

$[g_-;\mathbf{g_-cFcF};g_-t_2]^+$

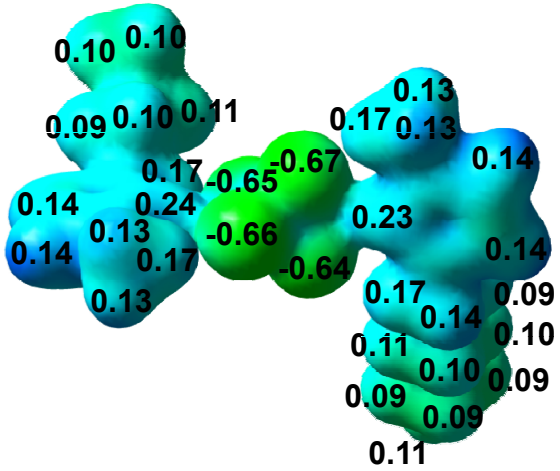

$[g_-t_2;\mathbf{g_-cFcF};g_+t_4]^+$

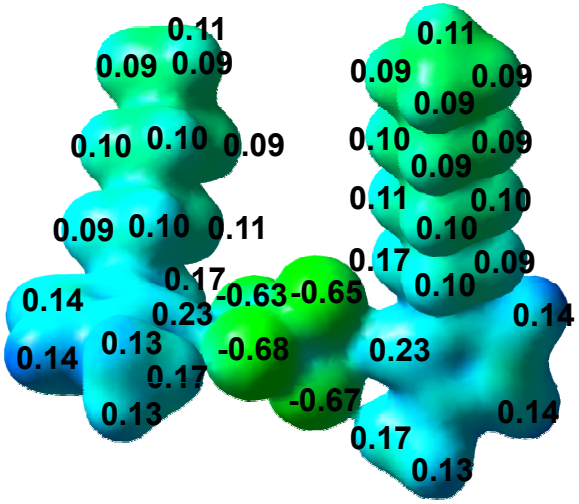

$[g_-t_4;\mathbf{g_+cFcF};g_+t_6]^+$

$[C_2mim:BF_4:C_4mim]^+$

$[C_4mim:BF_4:C_6mim]^+$

$[C_6mim:BF_4:C_8mim]^+$

$[g_-;\mathbf{g_+g_-FcF};g_{+2}t]^+$

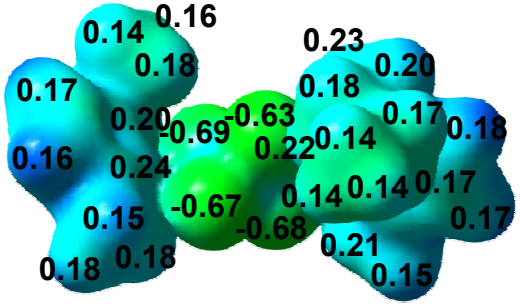

$[g_+g_{-2};\mathbf{tcF_mcF};g_-g_+t_3]^+$

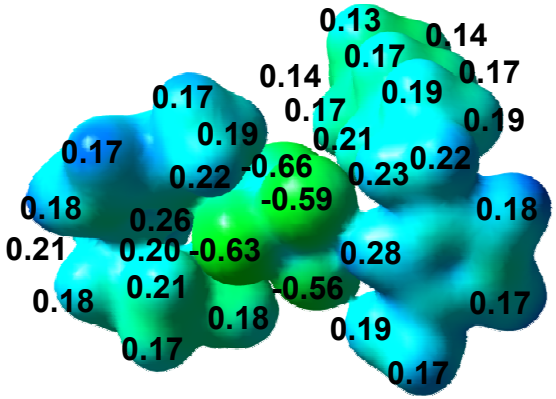

$[g_+g_-t_2g_-;\mathbf{g_-cFcF};g_-g_{+2}t_2g_+t\ ]^+$

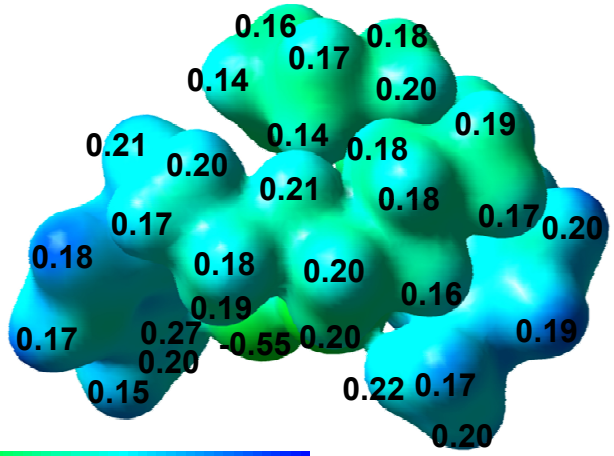

M06-2X/6-311+G(d,p)

Figure S3.

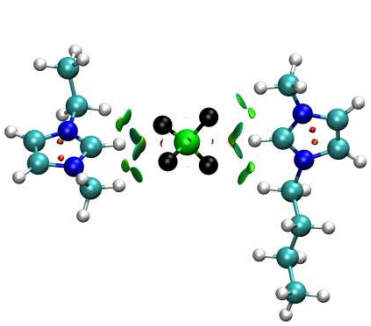

$[g_-;\mathbf{g_-cFcF};g_-t_2]^+$
0.0, 5.0, - kJ/mol

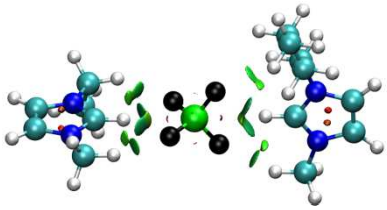

$[g_+;\mathbf{g_+cFcF};g_+t_2]^+$
0.0, 2.8, - kJ/mol

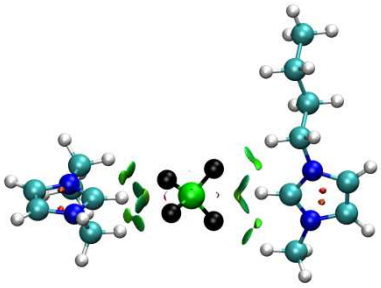

$[g_+;\mathbf{g_+cFcF};g_-t_2]^+$
0.1, 0.4, - kJ/mol

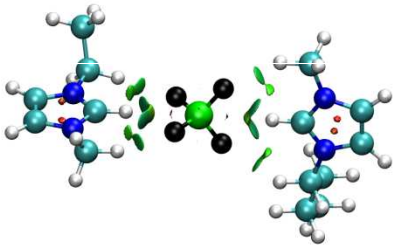

$[g_-;\mathbf{g_-cFcF};g_+t_2]^+$
0.1, 0.0, - kJ/mol

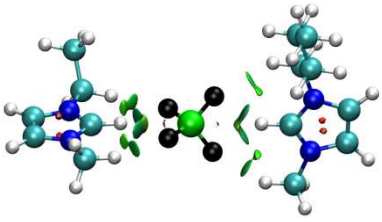

$[g_-;\mathbf{g_+cFcF};g_+t_2]^+$
0.6, 1.3, - kJ/mol

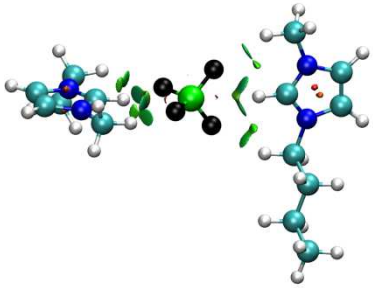

$[g_+;\mathbf{g_-cFcF};g_-t_2]^+$
0.6, 1.3, - kJ/mol

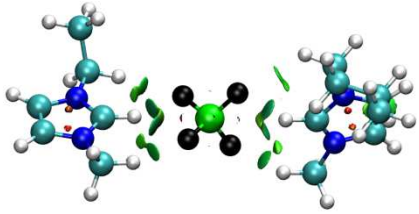

$[g_-;\mathbf{g_+cFcF};g_{+2}t]^+$
1.3, 5.4, - kJ/mol

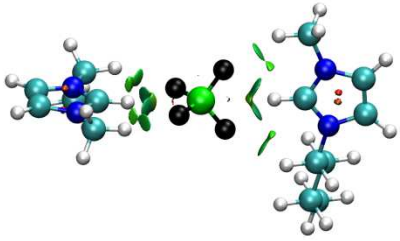

$[g_+;\mathbf{g_-cFcF};g_+t_2]^+$
1.3, 7.4, - kJ/mol

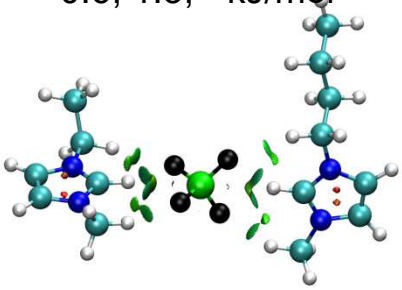

$[g_-;\mathbf{g_+cFcF};g_-t_2]^+$
1.3, 3.3, - kJ/mol

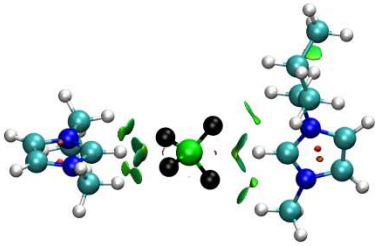

$[g_+;\mathbf{g_+cFcF;}g_+tg_-]^+$
1.9, 5.6, - kJ/mol

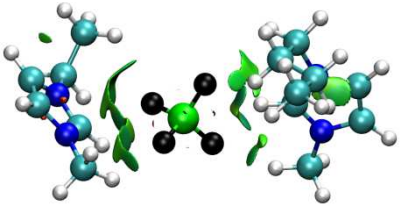

$[g_-;\mathbf{g_+g_-FcF};g_{+2}t]^+$
-, -, 0.0* kJ/mol

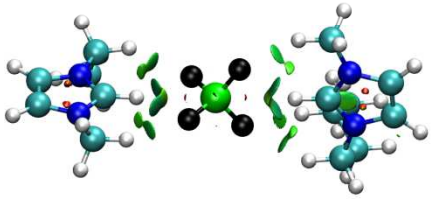

$[g_+;\mathbf{g_-cFcF};g_+g_-t]^+$
3.8, 3.5, 0.0 kJ/mol

$[C_2mim:BF_4:C_4mim]^+$

Figure S4.

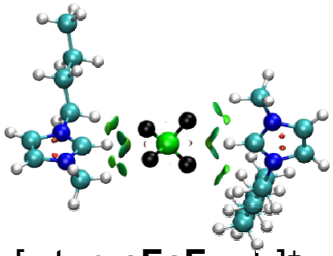

$[g_-t_2;\mathbf{g_-cFcF};g_+t_4]^+$
0.0, 5.1, - kJ/mol

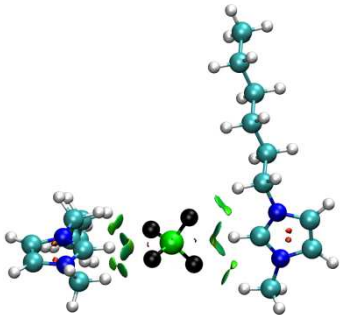

$[g_+t_2;\mathbf{g_+cFcF};g_-t_4]^+$
0.1, 5.0, - kJ/mol

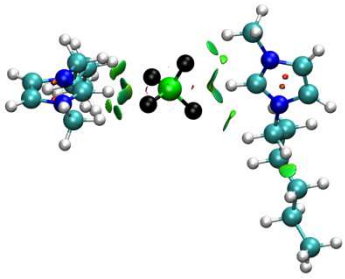

$[g_+t_2;\mathbf{g_-cFcF};g_+tg_-t_2]^+$
1.2, 5.5, 2.5 kJ/mol

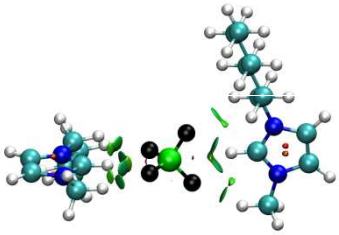

$[g_+t_2;\mathbf{g_+cFcF};g_+t_4]^+$
3.3, 5.8, - kJ/mol

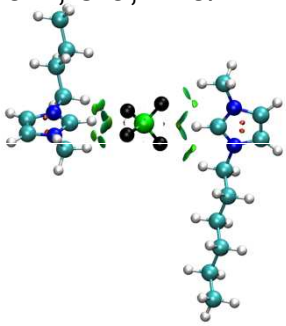

$[g_-t_2;\mathbf{g_-cFcF};g_-t_4]^+$
3.3, 5.8, - kJ/mol

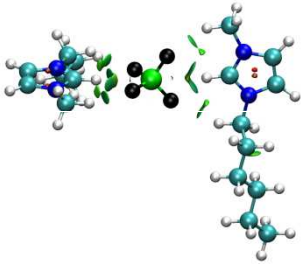

$[g_+t_2;\mathbf{g_-cFcF};g_-tg_+t_2]^+$
5.2, 6.0, - kJ/mol

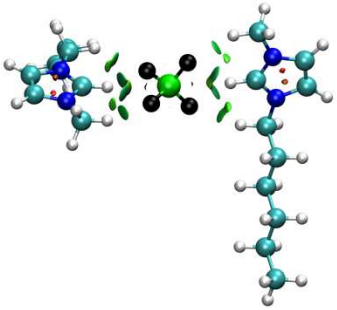

$[g_+t_2;\mathbf{g_-cFcF};g_-t_4]^+$
6.1, 0.0, 1.2 kJ/mol

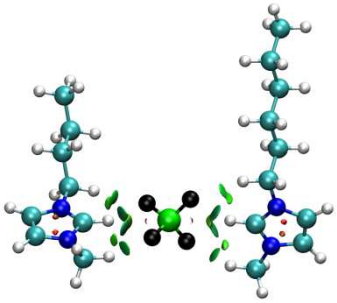

$[g_-t_2;\mathbf{g_+cFcF};g_-t_4]^+$
6.1, -, - kJ/mol

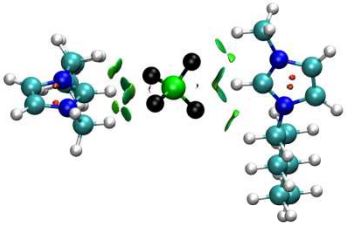

$[g_+t_2;\mathbf{g_-cFcF};g_+t_4]^+$
6.1, -, - kJ/mol

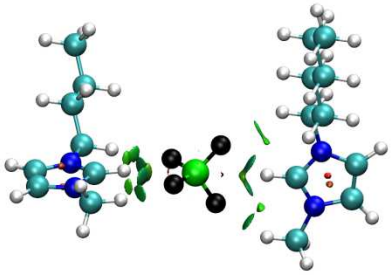

$[g_-t_2;\mathbf{g_+cFcF};g_+t_4]^+$
6.1, 5.4, - kJ/mol

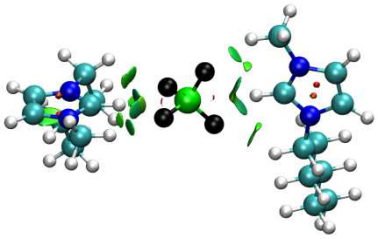

$[g_{+2}t;\mathbf{g_-cFcF};g_+t_4]^+$
7.0, -, - kJ/mol

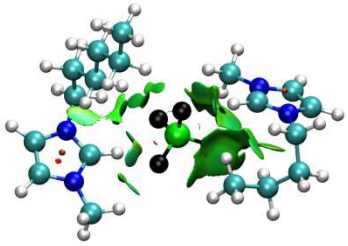

$[g_+g_{-2};\mathbf{tcF_mcF};g_-g_+t_3]$
-, -, 0.0 kJ/mol

$[C_4mim{:}BF_4{:}C_6mim]^+$

Figure S5.

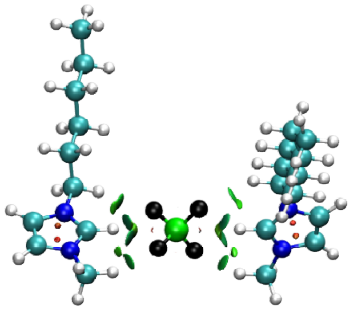

$[g_{-}t_4;\mathbf{g_{+}cFcF};g_{+}t_6]^{+}$
0.0, -, - kJ/mol

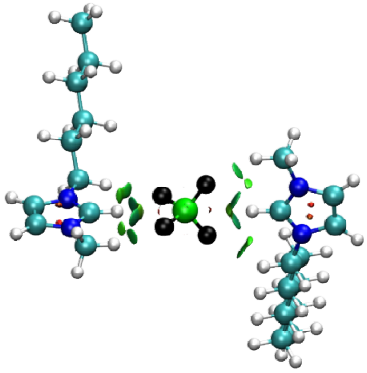

$[g_{-}t_4;\mathbf{g_{-}cFcF};g_{+}t_6]^{+}$
1.2, 2.4, - kJ/mol

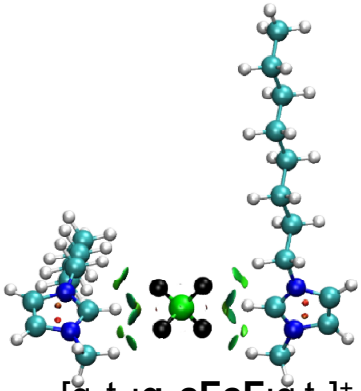

$[g_{+}t_4;\mathbf{g_{+}cFcF};g_{-}t_6]^{+}$
1.3, 2.5, - kJ/mol

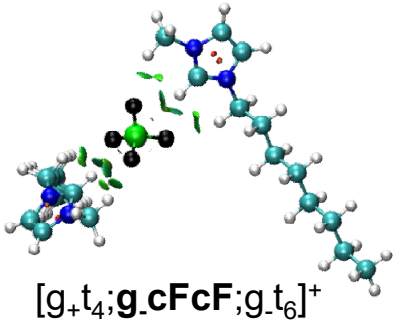

$[g_{+}t_4;\mathbf{g_{-}cFcF};g_{-}t_6]^{+}$
2.2, 3.1, - kJ/mol

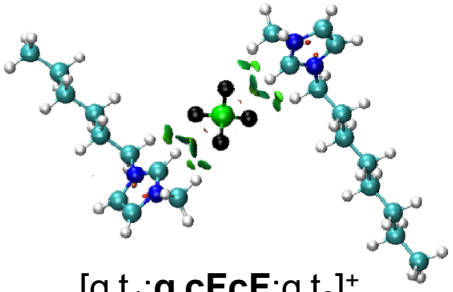

$[g_{-}t_4;\mathbf{g_{-}cFcF};g_{-}t_6]^{+}$
2.4, 7.2, - kJ/mol

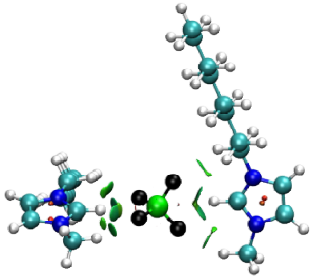

$[g_{+}t_4;\mathbf{g_{+}cFcF};g_{+}t_6]^{+}$
2.5, 7.2, - kJ/mol

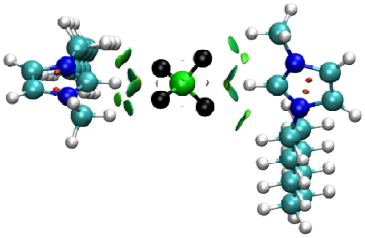

$[g_{+}t_4;\mathbf{g_{-}cFcF};g_{+}t_6]^{+}$
3.0, 1.1, 5.1 kJ/mol

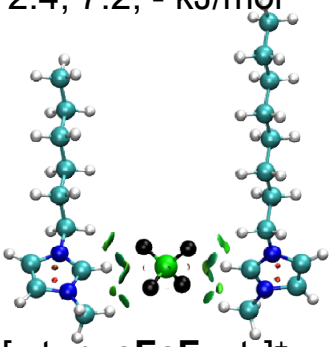

$[g_{-}t_4;\mathbf{g_{+}cFcF};g_{-}t_6]^{+}$
3.0, 0.1, - kJ/mol

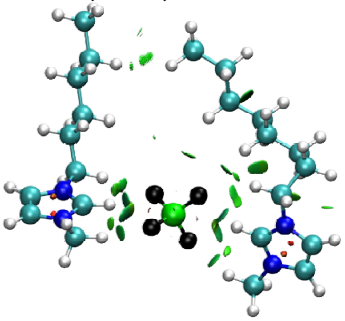

$[g_{-}t_4;\mathbf{g_{+}cFcF};g_{-}g_{+2}t_2g_{+}t]^{+}$
10.1, 4.9, 4.9 kJ/mol

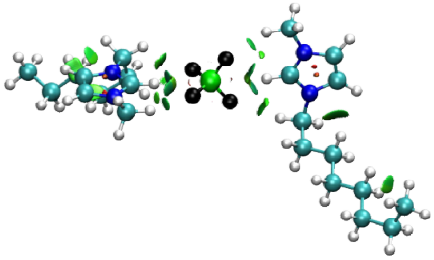

$[g_{+3}t_2;\mathbf{g_{-}cFcF};g_{-2}t_4g_{+}]^{+}$
12.0, 10.7, 2.8* kJ/mol

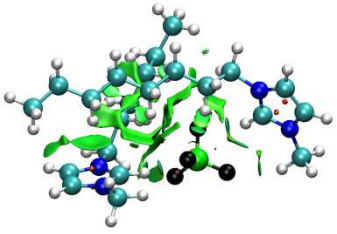

$[g_{-}t_4;\mathbf{g_{+}cF_acF};g_{+}t_6]^{+}$
-, 0.0, - kJ/mol

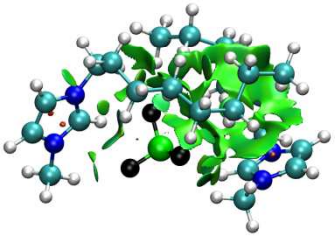

$[g_{+}g_{-}t_2g_{-};\mathbf{g_{-}cFcF};g_{-}g_{+2}t_2g_{+}t]^{+}$
17.7, 1.2, 0.0 kJ/mol

$[C_6mim{:}BF_4{:}C_8mim]^{+}$